

68-11,842

SHULER, William Beeuwkes, 1939-  
MEASUREMENTS OF PIONIC AND MUONIC  $K_{\alpha}$   
X-RAY ENERGIES IN LOW Z ATOMS.

The College of William and Mary in Virginia,  
Ph.D., 1968  
Physics, nuclear

University Microfilms, Inc., Ann Arbor, Michigan

MEASUREMENTS OF PIONIC AND MUONIC  $K_{\alpha}$  X-RAY ENERGIES IN LOW Z ATOMS

---

A Thesis

Presented to

The Faculty of the Department of Physics  
The College of William and Mary in Virginia

---

In Partial Fulfillment

Of the Requirements for the Degree of  
Doctor of Philosophy

---

by

William Beeuwkes Shuler

March 1968

APPROVAL SHEET

This thesis is submitted in partial fulfillment of  
the requirements for the degree of  
Doctor of Philosophy

W. B. Shuler

Author

Approved, March 1968

Morton Eckhause

Morton Eckhause

Rolf G. Winter

Rolf G. Winter

Robert T. Siegel

Robert T. Siegel

Raymond W. Southworth

Raymond W. Southworth

Robert E. Welsh

Robert E. Welsh

David A. Jenkins

David A. Jenkins

MEASUREMENTS OF PIONIC AND MUONIC  $K_{\alpha}$  X-RAY ENERGIES IN LOW Z ATOMS

## TABLE OF CONTENTS

|   | Page |
|---|------|
| I. ABSTRACT . . . . .   | 1    |
| II. INTRODUCTION . . . . .                                      | 2    |
| III. EXPERIMENTAL METHOD . . . . .                              | 24   |
| A. General Technique  |      |
| B. Beam Characteristics   |      |
| C. Counters and Counter Geometry                                |      |
| D. Timing and Logic Circuitry                                   |      |
| E. $\gamma$ -Ray Spectrometers                                  |      |
| F. Stabilization  |      |
| G. Targets  |      |
| H. Calibration  |      |
| I. System Linearity   |      |
| IV. ANALYSIS OF DATA . . . . .                                  | 46   |
| A. General Technique  |      |
| B. Analysis of Calibration Lines                                |      |
| C. Analysis of X-Ray Lines                                      |      |
| V. RESULTS AND THEORETICAL CONSIDERATIONS . . . . .             | 60   |
| A. Computation of Pionic and Muonic $K_{\alpha}$ X-Ray Energies |      |
| B. Vacuum Polarization Corrections                              |      |
| C. Coulomb Corrections  |      |
| D. Nuclear Force Shift  |      |
| VI. TABLES . . . . .  | 73   |
| VII. ACKNOWLEDGMENTS . . . . .                                  | 84   |
| VIII. LIST OF REFERENCES . . . . .                              | 86   |
| IX. FIGURES . . . . .   | 90   |

## I. ABSTRACT

Pionic and muonic  $K_{\alpha}$  X-ray energies have been measured for elements in the range  $Z = 3$  to  $Z = 6$  using high resolution Si(Li) and Ge(Li)  $\gamma$ -ray spectrometers. Level corrections due to vacuum polarization and the finite extent of the nuclear charge distribution have been calculated. The nuclear force shifts due to the strong pion-nucleus interaction have been measured for the  $1s$  levels of pionic atoms and are found to be in fair agreement with the shifts calculated according to the theory of the Ericsons. The X-ray energy and nuclear force shift measurements reported here represent a substantial improvement in precision over previous measurements. The measured pionic and muonic  $K_{\alpha}$  X-ray energies and the pionic  $1s$  level nuclear force shifts (keV) are:

| ELEMENT         | $E(\pi K_{\alpha})$ | $E(\mu K_{\alpha})$ | $E_{nuc}$       |
|-----------------|---------------------|---------------------|-----------------|
| Li <sup>6</sup> | 24.18 $\pm$ 0.06    | 18.66 $\pm$ 0.07    | 0.35 $\pm$ 0.06 |
| Li <sup>7</sup> | 24.06 $\pm$ 0.06    | 18.71 $\pm$ 0.06    | 0.57 $\pm$ 0.06 |
| Be <sup>9</sup> | 42.32 $\pm$ 0.05    | 33.39 $\pm$ 0.05    | 1.63 $\pm$ 0.08 |
| B <sup>10</sup> | 65.79 $\pm$ 0.11    | 52.18 $\pm$ 0.10    | 2.96 $\pm$ 0.12 |
| B <sup>11</sup> | 65.00 $\pm$ 0.11    | 52.23 $\pm$ 0.09    | 3.85 $\pm$ 0.12 |
| C <sup>12</sup> | 93.19 $\pm$ 0.12    | 75.23 $\pm$ 0.08    | 5.96 $\pm$ 0.12 |

Nuclear radii determined from the muonic X-ray data were found to be in agreement with those determined from electron scattering experiments.

## II. INTRODUCTION

A mesic atom is formed when a negatively charged meson is captured in an outer Bohr orbit of a normal electronic atom. From this orbit, the meson cascades by radiative and Auger transitions to the innermost atomic shells where it is either absorbed by the nucleus or undergoes radioactive decay. Observation of the X-rays emitted during the cascade process provides information on meson properties, nuclear parameters, and meson-nucleus interaction forces.

The existence of such atoms was postulated as the result of an experiment performed by Conversi et al.,<sup>1</sup> in 1947. However, the first conclusive observations of mesic X-rays were not made until 1952 when Camac et al.,<sup>2</sup> used a scintillation counter to detect X-rays from negative pions stopped in carbon. A number of experiments followed in which observations of pionic and muonic X-rays were made using the critical absorber technique, scintillation detectors and proportional counters. A comprehensive summary of these experiments and early theoretical developments is given in a survey article by West<sup>3</sup> on mesic atoms.

With the advent of high-resolution Ge(Li) and Si(Li) detectors, new interest has been generated in the field of mesic X-rays, and many of the earlier experiments are being repeated and augmented with increased precision. Specifically, Jenkins, et al.,<sup>4,5,6</sup> at Berkeley and Backenstoss, et al.,<sup>7,8,9</sup> at CERN have been engaged in measuring energies and widths of pionic and muonic X-ray lines with solid state  $\gamma$ -ray spectrometers. The increased precision and scope of these

experiments allow a more detailed investigation of the effects which contribute to shifts and broadening of the energy levels of mesic atoms.

The purpose of the present investigation is twofold. First is the accurate determination of the energies of the pionic and muonic  $K_{\alpha}$  X-rays observed when pions and muons are stopped in targets of  $\text{Li}^6$ ,  $\text{Li}^7$ ,  $\text{Be}^9$ ,  $\text{B}^{10}$ ,  $\text{B}^{11}$ , and  $\text{C}^{12}$ . Second is the determination, based on these measurements, of the  $1s$  level shift due to the strong pion-nucleus interaction in mesic atoms formed in the same elements. This shift is generally referred to as the nuclear force shift. The determination of the experimental nuclear force shift is based on a comparison of the measured and theoretically predicted pionic  $K_{\alpha}$  X-ray transition energies. The theoretically predicted energies include corrections for effects other than the nuclear force shift which perturb the mesic energy levels. These effects are primarily of electromagnetic origin, and therefore, the corresponding level corrections can be calculated to a high degree of accuracy. The difference between the theoretical  $K_{\alpha}$  X-ray energies thus calculated and the corresponding measured energies is attributed to the nuclear force effect.

The remainder of this section is a description of the features of the energy levels of mesic atoms and of the phenomena that produce shifts in the levels of light pionic and muonic atoms. Estimates of the magnitudes of the shifts are given; however, detailed calculations of the most important shifts are deferred until section V. Finally, several theoretical investigations of the nuclear force shift are discussed.

The features of the energy levels of mesic atoms are most easily understood by comparing them to similar features occurring in more familiar electronic atoms. The gross structure of mesic energy levels is accounted for by the Bohr equations for level energies and orbital radii. Since the energy of an atomic bound state is proportional to the system's reduced mass, the levels of mesic atoms are lowered relative to those of similar electronic atoms by the meson-electron mass ratio ( $m_{\pi}/m_e = 273$ ,  $m_{\mu}/m_e = 207$ ). Hence the meson is more tightly bound, and the energies of mesic X-rays are increased compared to similar electronic X-ray energies by the same factor. Similarly, since the radius of a Bohr orbit is inversely proportional to the system's reduced mass, the radii of mesic orbits are smaller than those of similar electronic orbits by the electron-meson mass ratio. There are several interesting consequences of the smaller orbit size for mesons:

1. The principal quantum number,  $n$ , for a mesic orbit having a radius equal to that of the K electron orbit in the same atom is 17 for pions and 14 for muons. Hence in the treatment of the lower levels of the pionic and muonic atoms, the effect of the electron cloud can be neglected and the mesic energy levels are hydrogen-like to a very good approximation. Thus, neglecting other effects, only the Coulomb potential of the nucleus need be used with the Klein-Gordon and Dirac equations to calculate energies of the lower levels of pionic and muonic atoms.
2. Since the mesic orbital radii are smaller, the wave function overlap with the nuclear volume is increased for mesic s states.

This is also true for states of higher  $l$ ; however, for these states the wave functions are small within the nuclear volume and the effect is greatly reduced. The large  $s$  state wave function overlap means that mesons in  $s$  states spend a substantial fraction of their lifetimes within the nuclear volume. During this time the total nuclear charge is not effective, and the electromagnetic meson-nucleus interaction is decreased, causing the meson to be less tightly bound and the  $s$  levels to be shifted upward. This effect is generally referred to as the Coulomb effect or the finite nuclear size effect. It has been estimated by Cooper and Henley<sup>10</sup> and a generalized expression for the shift is given by West<sup>3</sup>:

$$\frac{E_{\text{Coul}}}{E_Z} = \frac{4}{5} \frac{1}{n^3} \left( \frac{ZR}{r_B} \right)^2$$

where

$$E_Z = -\frac{1}{2} \mu (Z\alpha c)^2$$

and

$$r_B = \frac{\hbar^2}{\mu e^2}$$

Here  $\mu$  is the system's reduced mass, and  $R$  is the nuclear radius for the equivalent uniform charge distribution. This equation is applicable only for  $s$  states with  $Z < 10$ , where the shift is about 1 percent. Since the Coulomb shift for  $s$  states is proportional to  $\mu^3$ , the shift for pionic  $1s$  states should be about twice that for muonic  $1s$  states. A corresponding expression for the shift in the  $2p$  level has been

derived by Flügge<sup>11</sup> and is given by West<sup>3</sup>:

$$\frac{E_{\text{Coul}}}{E_Z} = \left[ 0.0018 \left( \frac{Z_R}{r_B} \right)^4 - 0.0010 \left( \frac{Z_R}{r_B} \right)^5 + \dots \right]$$

The energy shift for p states is approximately 0.0001 percent for pionic carbon and can be neglected. Detailed calculations of 1s level shifts according to Pustovalov<sup>12</sup> in light pionic and muonic atoms are described in section V.

3. The energy levels of normal atoms are further shifted because of radiative effects. This shift is composed of two parts: that due to the interaction of the electron with vacuum fluctuations of the electromagnetic field, generally known as the radiative reaction or electron self energy modification, and that due to polarization of the vacuum by the field of the nucleus, known as vacuum polarization. These two effects give rise to the well known Lamb-shift in hydrogen, a shift of the  $2s_{1/2}$  level (doublet) upward relative to the  $2p_{1/2}$  level by approximately 1057 MHz. The radiative reaction accounts for most of this upward shift; however, there is a small negative shift of about 27 MHz due to vacuum polarization effects. The correction due to radiative reaction is in the first approximation inversely proportional to the square of the mass of the orbiting particle<sup>13</sup> and is thus negligible for pionic and muonic atoms. The correction due to vacuum polarization is independent of mass<sup>13</sup>. Vacuum polarization may be interpreted within the framework of Dirac hole theory. According to this picture, a

positive-energy negatively charged particle electrostatically repels electrons in the negative-energy electron sea which comprises the vacuum. Thus the vacuum is polarized in the vicinity of the particle and the physically measured charge of the particle,  $e$ , is comprised of contributions from the charge density of the "bare" particle,  $\rho_0(r)$ , and the induced vacuum polarization charge  $\rho_P(r)$ :

$$e = \int d^3r [\rho_0(\vec{r}) + \rho_P(\vec{r})].$$

The bare charge is just:

$$e_0 = \int d^3r \rho_0(\vec{r}),$$

with  $|e_0| > |e|$  since the induced vacuum polarization charge and the bare charge are of opposite sign. Thus when two charged particles are brought very close together, the bare charge becomes more important, and the strength of the electromagnetic interaction is increased. For mesic atoms this effect is enhanced because of the small orbital radii, and the levels are correspondingly shifted downward. The shift is largest for s states because of the large wave function overlap with the nucleus. Corrections to the 1s and 2p levels for pionic carbon are about 0.5 percent and 0.2 percent, respectively, with smaller corrections (because of the larger orbit size) for the same levels of muonic carbon. Calculations of the level shifts due to vacuum polarization for the 1s and 2p levels of light pionic and muonic atoms have been made according

to the method of Mickelwait and Corben<sup>13,14</sup> and are described in detail in section V.

Excluding the nuclear force shift for pionic atoms, the Coulomb effect and vacuum polarization give rise to the largest level shifts in light pionic and muonic atoms. Other secondary effects that give rise to smaller, in fact negligible, level shifts include:

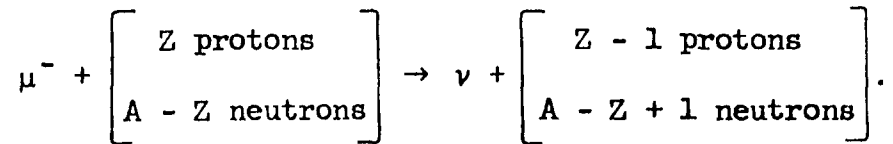
1. the effect of the electron cloud. This effect has been previously mentioned in the description of the general features of the energy levels of mesic atoms. The presence of an electron cloud causes a reduction in the binding energy of the mesic energy levels; i.e., shifts them upward since the negatively charged cloud tends to reduce the attractive effect of the nuclear charge. The shift is small, especially for low-lying mesic levels. Stearns and Stearns<sup>15</sup> have estimated the correction due to the presence of the electron cloud to the 4f-3d transition in muonic phosphorus to be approximately 0.003 percent.
2. polarization of the nuclear charge. The decreased orbital radii for mesic atoms results in polarization of the nuclear charge by the meson when it is near the nucleus. This results in a shift downward of the mesic energy levels since the nuclear charge becomes concentrated near the meson. This effect has been estimated to give an increase in the transition energies of less than 0.01 percent for light atoms<sup>10</sup>.
3. discreteness of the nuclear charge distribution. Cooper and Henley<sup>10</sup> have estimated the effect of the discreteness of the

nuclear charge distribution on the low-lying levels of mesic atoms. This effect causes a shift in the  $1s$  level of muonic lead of only 0.1 percent and is negligible for light elements because of the larger average distance of the meson from the nucleus.

4. fine and hyperfine structure. For muonic atoms there is the usual fine structure splitting between levels with  $j = l \pm \frac{1}{2}$  due to the coupling of the muon's spin with its orbital angular momentum vector. A simple perturbation estimate shows the splitting to be proportional to  $\mu Z^4/n^3$ . It is thus enhanced relative to that observed in similar electronic atoms by the meson-electron mass ratio. This splitting is of the order of 10 eV (0.01 percent) for the  $2p_{1/2}$  and  $2p_{3/2}$  levels of muonic  $C^{12}$  and is reduced slightly by the Coulomb effect, especially in heavy mesic atoms. The levels of pionic atoms do not exhibit fine structure of this type since the pion spin is zero. Hyperfine structure results from the coupling of the magnetic moment of the nucleus with the magnetic field associated with the motion of the meson. Each level is split according to the possible states of total angular momentum,  $F$ , compounded from the total meson angular momentum,  $J$ , and the spin,  $I$ , of the nucleus. This splitting is reduced relative to the fine structure splitting by approximately the meson-nucleon mass ratio<sup>16</sup>. For pionic atoms there is a small relativistic splitting of states of different  $l$  for a given  $n$ ; the  $s$  states being most tightly bound. This splitting is predicted by the Klein-Gordon equation

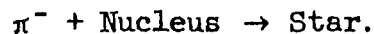
and is approximately the same magnitude as muonic fine structure

5. quadrupole splitting. The levels of both pionic and muonic atoms are split because of effects caused by the quadrupole moment of the nucleus. The splitting depends on the orientation of the total angular momentum vector of the meson relative to the nuclear angular momentum vector and is due to the deviation from spherical symmetry of the nuclear charge distribution. The magnitude of the splitting for muonic atoms is generally much smaller than the fine structure splitting<sup>10</sup>. The splitting varies as the cube of the system's reduced mass so that for pionic atoms the splitting is only about two times greater than that for muonic atoms. However, for intermediate and heavy nuclei, where large quadrupole moments occur, the splitting may be of the same magnitude as that due to spin-orbit coupling<sup>10</sup>.
6. Coulomb excitation of nuclear levels. Level splitting may occur because of possible Coulomb excitation of nuclear rotational levels by the bound meson<sup>17</sup>. This effect is expected to occur in heavy elements and the splitting is of the same order as that due to fine structure<sup>3</sup>.
7. nonelectric interaction of the muon. This weak interaction gives rise to nuclear capture of the muon primarily from the 1s state where the wave function overlap is greatest. The capture process is:



The interaction strength is approximately the same as that for the electron-nucleon beta decay process<sup>18,19</sup>. Hill and Ford<sup>20</sup> have estimated that this interaction shifts the levels of muonic lead by less than 1 eV. Since the probability of nuclear capture from the 1s state varies as  $Z_{\text{eff}}^4$ ,<sup>21</sup> where  $Z_{\text{eff}}$  is the effective nuclear charge seen by the muon in its 1s state, this effect is negligible for low Z muonic atoms.

The seven secondary effects listed above have been neglected in the present analysis. Of the three major effects, the nuclear force shift, vacuum polarization, and Coulomb effect, the first is by far the largest. The nuclear force shift exists only for pionic atoms and is due to the strong pion-nucleon interaction. The strong interaction gives rise to both shifts and broadening of the levels of pionic atoms and results in the fast nuclear capture of the pion from the low-lying levels, leading to the process<sup>22</sup>:



The nuclear capture rate from a given low level competes with the radiative rate from the same level. Messiah and Marshak<sup>23</sup> estimate that for  $Z \geq 3$  nuclear capture is expected to predominate over the radiative rate for the 2p state. Therefore, pionic  $K_{\alpha}$  radiation is expected only from the very light elements. Blackenstoss et al.,<sup>8</sup> have observed pionic  $K_{\alpha}$  radiation from Na<sup>23</sup>; however, they were unable to detect such radiation in Mg and Al.

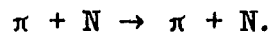
In the pion capture process there is a liberation of approximately 139 MeV (pion rest mass) as kinetic energy. The concentration of all this kinetic energy on one nucleon means it will move with a momentum of over 500 MeV/c. Since the pion momentum is negligible, the nucleon must have an initial momentum of 500 MeV/c by conservation of momentum. However, the Fermi momentum is only of the order of 250 MeV/c, so that such high momentum components are unlikely and capture by one nucleon is improbable. However for two or more participating nucleons, relative momentum components of the necessary magnitude are possible, and nuclear capture is expected to be due mainly to a reaction of the form



and it is such reactions which result in level broadening in pionic atoms. Broadening for the  $K_{\alpha}$  transition lines observed in this investigation is discussed elsewhere<sup>24</sup>. Absorption also results in a real level shift due to the elastic process:



About 12 percent of the level shift observed in light pionic atoms is attributed to absorptive processes of this type.<sup>25</sup> The major part of the level shift (approximately 73 percent) is due to elastic pion-single nucleon scattering of the form:



This process is usually treated in the first approximation using the free pion-nucleon scattering amplitudes with modifications due to nuclear effects. The 1s level shift due to absorption enhances the

1s level shift calculated from the pion-single nucleon interaction.

Line broadening and level shifts have been the subjects of several theoretical investigations. All theories assert that the major part of the 1s shift is due to the elastic s-wave interaction between the pion and nucleons. Deser et al.,<sup>26</sup> have derived an expression for the shift by comparing the results of a perturbation calculation using the Schrodinger equation (including the Coulomb and pion-nucleon interaction potentials) to the matrix element describing forward scattering of positive energy pions by protons. The energy shift is thus related to the pion-nucleon s-wave scattering length  $\alpha_1$  and  $\alpha_3$  corresponding to isotopic spin states 1/2 and 3/2. Their expression for the energy shift of the 1s level is

$$\frac{\Delta E}{E_Z} = \frac{4Z}{r_B} \left[ \frac{2Z}{3} \alpha_1 + \frac{3N + Z}{3} \alpha_3 \right],$$

where  $E_Z$  is the mesic 1s state Bohr energy and  $r_B$  is the mesic 1s Bohr radius. In this treatment it is assumed that the contributions of individual nucleons are independently additive<sup>3</sup> with each neutron contributing a shift proportional to  $\alpha_3$  and each proton contributing a shift proportional to  $(2\alpha_1 + \alpha_3)/3$ .

Brueckner<sup>22</sup> has calculated an expression for the 1s energy level shift taking into account two-nucleon absorption. The expression consists of a term associated with the scattering of pions by single nucleons which is similar to that obtained by Deser et al.,<sup>26</sup> and an additional term depending on the pion absorption rate and associated

with the two nucleon absorption. The absorption rate has been estimated<sup>27</sup> on the basis of the cross section for pion absorption in deuterium ( $\pi^- + D \rightarrow 2n$ ). This additional shift due to two-nucleon absorption is about 0.7 times that predicted without absorption and is to be added to the shift as given by Deser et al.. Later estimates<sup>28</sup> showed this additional shift to be only 0.25 times that predicted by Deser et al.. Additional calculations,<sup>29</sup> including the elastic p wave interaction, give a shift of the same magnitude but opposite that predicted from absorptive effects.

One of the most recent and detailed theoretical investigations of the nuclear force shift is that of Ericson and Ericson<sup>30,31,32</sup>. They include a nonlocal potential for pions in finite nuclei using the amplitudes for pion-nucleon scattering and for pion production in nucleon-nucleon collisions. The pion-nucleus interaction is analyzed, in the first approximation, by assuming that the scattering amplitudes for pions incident on bound nucleons are the same as those for pions incident on free nucleons except for kinematical factors. In the initial development the scattering amplitude for the  $i^{\text{th}}$  nucleon is assumed to be:

$$f_1(\vec{r}) = [b_0 + c_0 \vec{k}' \cdot \vec{k}] \delta(\vec{r} - \vec{r}_1)$$

where  $\vec{k}$  and  $\vec{k}'$  are the momenta of the incident and of the scattered pion, while  $b_0$  and  $c_0$  are given by

$$b_0 = \frac{1}{3}(\alpha_1 + 2\alpha_3)$$

$$c_0 = \frac{1}{2}(4\alpha_{33} + 2\alpha_{31} + 2\alpha_{13} + \alpha_{11}).$$

The  $\alpha_{2t,2j}$  ( $t$  = total isospin,  $j$  = total spin of the  $\pi N$  system) are the  $p$  wave ( $\pi N$ ) scattering volumes. The amplitude  $f_1(\vec{r})$  is for single nucleon-pion elastic scattering and does not include absorptive processes. The multiple scattering equations are developed by expressing the total pion-nucleus wave function for both elastic and inelastic scattering as the sum of the incident wave and the scattered wave emerging from every one of the scatterers  $i$  in the nucleus. The scattered wave is unknown and is determined by an iterative process giving rise to a systematic expansion of the scattering equations into higher order correlation functions between scatterers. The nucleons are assumed massive, and the nuclear excitation energies are assumed to be negligible. These equations are applicable to both inelastic and elastic processes; however, the computations are simplified considerably by treating only elastic scattering using  $f_1(\vec{r})$  as given above. If the expansion is truncated at the earliest possible stage, no correlations are included, and the resulting pion-nucleus interaction potential is ( $\hbar = c = m_\pi = 1$ )

$$V_1(\vec{r}) = -2\pi \left[ b_0 \rho(\vec{r}) - \vec{\nabla} \cdot c_0 \rho(\vec{r}) \vec{\nabla} \right],$$

where  $\rho(\vec{r})$  is the nuclear density distribution function. The gradient operators result from replacing  $\vec{k}$  and  $\vec{k}'$  by their corresponding momentum operators in  $f_1(\vec{r})$ . The most notable feature of this potential is the explicit dependence on the nonlocal  $p$  wave interaction (gradient term). This potential is obtained by interrupting the expansion of the scattering equations at the earliest possible stage. If very short pair correlations are admitted, and the expansion carried out one more step, the following potential is obtained ( $\hbar = m_\pi = c = 1$ ):

$$V_2(\vec{r}) = -2\pi \left[ b_{0\rho}(\vec{r}) - \vec{\nabla} \cdot \frac{c_{0\rho}(\vec{r}) \vec{\nabla}}{1 + \frac{4\pi}{3} c_{0\rho}(\vec{r})} \right].$$

$V_2$  differs from  $V_1$  by the explicit nonlinear dependence on the density of scatterers. This nonlinear density dependence is referred to by the Ericsons as the Lorentz-Lorenz effect due to the similarity of this result and that obtained for dipole scattering of electromagnetic waves through a dense medium of polarizable atoms. The potential  $V_2$  is expected to be a better approximation than  $V_1$  since in the derivation of  $V_1$  the effects of self excitation of a particular scatterer were not excluded. These effects could apparently give rise to considerable errors<sup>30</sup>, particularly when the scattering amplitude  $f_1$  has important contributions with  $l \neq 0$ .

The potentials  $V_1$  and  $V_2$  are obtained from the scattering amplitudes for free ( $\pi N$ ) elastic scattering with the assumptions that nuclear excitation energies are negligible and that the nucleons are massive. No spin or isospin effects are included, nor is the contribution to the real potential from absorptive effects considered. The Ericsons correct for these assumptions by considering their effect on the free scattering amplitudes appearing in  $V_1$  and  $V_2$ . The corrections would appear as additional terms in the interaction potential; however, for the sake of convenience they are treated as giving rise to effective values of the scattering amplitudes.

Specifically, corrections considered are:

1. different kinds of scatterers. This correction results in the replacement of

$$b_0^{\rho}(\vec{r}) \rightarrow \sum_{\lambda} b_{0\lambda} \rho_{\lambda}(\vec{r})$$

and

$$c_0^{\rho}(\vec{r}) \rightarrow \sum_{\lambda} c_{0\lambda} \rho_{\lambda}(\vec{r}),$$

where the different kinds of scatterers are denoted by the index  $\lambda$  (e.g.,  $\lambda = 1$  signifies a proton,  $\lambda = 2$  a neutron) and the average density of particles of index  $\lambda$  is  $\rho_{\lambda}(\vec{r})$ .

2. nonnegligible nuclear excitation energies. The small pion mass reduces the corrections from intermediate excitation energies relative to those expected from nucleon-nuclear scattering to negligible amounts<sup>30</sup>.
3. effects of binding and Fermi motion. Since the nucleons are only approximately massive there is a kinematical correction to the scattering amplitude for pions on free nucleons. The free scattering amplitude,  $f_1(\vec{r})$ , is multiplied by the Fermi factor

$$\frac{k_{\text{bound}}}{k_{\text{free}}} = \left[ \frac{(M^2 + m_{\pi}^2 + 2ME)}{M^2} \right]^{1/2}$$

where  $E$  is the total energy (including rest energy) of the pion. If the kinetic energy of the pion is assumed to be zero, i.e.,  $E = m_{\pi}$ , the Fermi factor becomes  $1 + m_{\pi}/M$ . This correction is about 14 percent.

According to the Ericsons' treatment, the Fermi motion gives rise to an induced s-wave interaction of the form ( $\kappa = c = 1$ ):

$$V_{\text{FM}} = - \frac{4\pi}{2m_\pi} \left( \frac{m_\pi}{M} \right)^2 \langle p_N^2 \rangle \frac{c_0 \rho(\vec{r})}{1 + \frac{4\pi}{3} c_0 \rho(\vec{r})}$$

with a contribution from the Lorentz-Lorenz effect appearing explicitly. Here  $\langle p_N^2 \rangle$  is the mean square momentum of a nucleon and is given by  $\langle p_N^2 \rangle \simeq \frac{3}{5} p_F^2$  where  $p_F = 250 \text{ MeV}/c$  is the Fermi momentum. The correction due to Fermi motion is of the order of  $m_\pi/M^2 \simeq \frac{1}{50}$ .

4. spin and isospin effects. These effects are included by replacing

$$b_0 \rho(\vec{r}) \rightarrow b_0 \rho(\vec{r}) + b_1 \vec{t} \cdot \vec{\tau}(\vec{r})$$

$$c_0 \rho(\vec{r}) \rightarrow c_0 \rho(\vec{r}) + c_1 \vec{t} \cdot \vec{\tau}(\vec{r}) - id_0 \vec{\sigma}(\vec{r}) \wedge$$

in the expression for  $V_2$ . Here  $\frac{1}{2} \vec{\sigma}(\vec{r})$  and  $\frac{1}{2} \vec{\tau}(\vec{r})$  are the spin and isospin densities, respectively, of the scattering system.

Also

$$b_1 = \frac{1}{3}(\alpha_3 - \alpha_1),$$

$$c_1 = \frac{1}{3}(2\alpha_{33} + \alpha_{31} - 2\alpha_{13} - \alpha_{11}),$$

and

$$d_0 = \frac{1}{3}(2\alpha_{31} - 2\alpha_{33} + \alpha_{11} - \alpha_{13}).$$

These replacements result from the inclusion of spin and isospin effects in the scattering amplitude  $f_1(\vec{r})$ . The spin and isospin densities are defined by the Ericsons to be

$$\vec{\sigma}(\vec{r}) = \frac{2}{A} \frac{\vec{J}(\vec{S} \cdot \vec{J})}{J(J+1)} \rho(\vec{r}),$$

and

$$\vec{\tau}(\vec{r}) = \frac{2}{A} \vec{T} \rho(\vec{r})$$

where the spin and isospin density distributions have been assumed equal to the nuclear density distribution. Here  $\vec{S}$  is the total spin,  $\vec{J}$  the total angular momentum, and  $\vec{T}$  the total isospin of the scattering system. The isospin term introduces an energy shift depending on the neutron excess due to the potential ( $\bar{n} = c = m_\pi = 1$ ):

$$-2\pi \left[ b_1^2 \frac{\vec{t} \cdot \vec{T}}{A} \right] \rho(\vec{r}).$$

The spin density term gives rise to a "strong hyperfine" splitting for the levels of  $\pi$  mesic atoms for  $l \neq 0$  of the form

$$-2\pi d_0 \frac{\vec{J} \cdot \vec{l}}{A} \frac{2(\vec{S} \cdot \vec{J})}{J(J+1)} \frac{1}{r} \frac{d}{dr} \left[ \frac{\rho(\vec{r})}{1 + \frac{4\pi}{3} c_0 \rho(\vec{r})} \right].$$

This splitting has been estimated for  $\text{Li}^6$ , using a uniform density distribution, to be less than 0.1 eV and is therefore negligible.

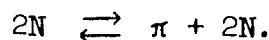
5. finite correlation length. The potential  $V_2(\vec{r})$  is derived assuming a very short-range pair correlation function. The neutron pair and the proton pair correlation lengths are assumed to be equal and the neutron-proton pair correlation length to be zero, resulting in an additional potential due to the finite correlation length of the form

$$-\pi^2 \left( 1 + \frac{M_\pi}{M} \right) \frac{9}{2p_F^2} (b_0^2 + b_1^2) \rho^2(\vec{r}).$$

This correction is of the order of 10 percent.

6. level shifts due to two-nucleon absorption. The Ericsons generalize a treatment of two-nucleon absorption in  $\text{He}^4$

developed by Eckstein<sup>33</sup>. Eckstein estimates the pion capture rate from a two-nucleon absorption model with a phenomenological interaction operator. The amplitudes appearing in the interaction operator are evaluated by a comparison with pion production cross sections. The Ericsons extend this treatment using a generalized phenomenological two-nucleon scattering amplitude. The structure of the resulting potential is similar to that obtained for pion-single nucleon elastic scattering with  $f_1(\vec{r})$  replaced by the two-nucleon amplitude and a two-nucleon density  $\rho^2(\vec{r})$  replacing  $\rho(\vec{r})$ . The two-nucleon amplitude involves complex constants related to the pion s and p wave interaction amplitudes with the two nucleons. The real part of the potential describing absorption gives rise to a real contribution to the level shifts and the imaginary part describes the level broadening. The imaginary parts of the complex scattering amplitudes are determined from processes of the form



The real parts of the scattering amplitudes may arise from reactions in which the pion is absorbed and re-emitted; however, they are experimentally unknown. The Ericsons assume that the magnitudes of the real parts of the amplitudes can be inferred from the magnitudes of the corresponding imaginary parts. Thus the real part of the two-nucleon amplitude is taken to be repulsive in both its s wave and p wave contribution with magnitude equal to that of the imaginary part. The contribution

to the level shifts from two-nucleon absorption appears as a correction to the pion-single nucleon scattering amplitudes in  $V_1$  and  $V_2$ .

The discussion of the corrections to the single nucleon scattering amplitudes arising from the above effects will be simplified by first determining the relevant contributions of  $V_2$  to the  $1s$  level shift, which is the one of interest here. A simple perturbation calculation using  $V_2$  and hydrogen-like wave functions gives an energy shift of the form:

$$\Delta E_{n,l} = -2\pi \left[ b_0 \int_{\text{all space}} \rho(\vec{r}) |\psi_{n,l}|^2 d\tau - c_0 \int_{\text{all space}} \frac{\rho(\vec{r})}{1 + \frac{4\pi}{3} c_0 \rho(\vec{r})} |\nabla \psi_{n,l}|^2 d\tau \right],$$

where the main contributions to the integrals are over the region of the nuclear volume. For the  $1s$  state, the nonlocal (gradient) term is negligible since the  $1s$  wave function is nearly constant within the nuclear volume. In this approximate calculation, the nonlocal term contributes a downward shift of roughly 30 eV for the  $1s$  level of  $C^{12}$ . The local interaction term dominates for the  $1s$  shift since the  $1s$  wave function is large in the region of the nuclear volume. For the  $1s$  level of  $C^{12}$ , this term gives rise to a shift of about 6 keV upward. However, for the  $2p$  state, the wave function is zero at the origin while its gradient is large in the nuclear region. Thus, the nonlocal term dominates for  $l \neq 0$  and the local interaction is negligible. For presently-known values of the single nucleon scattering amplitudes, the strong interaction raises  $l = 0$  states corresponding to a repulsive potential, while for states with  $l \neq 0$  the levels are lowered, indicating an attractive nonlocal potential. For pionic  $C^{12}$ , the  $2p$  shift has been estimated to

be of the order of 1 eV and is thus negligible compared to the 6 keV 1s shift. It is concluded, then, that the total experimental nuclear force shift as determined from the observed  $K_{\alpha}$  X-ray energies can be attributed entirely to shifts in the 1s level arising from the local interaction term in  $V_2$ . Thus for the 1s level shift  $V_2$  becomes

$$V_2(\vec{r}) = -2\pi b_0 \rho(\vec{r})$$

and we need correct only  $b_0$  for nuclear effects.

If the Fermi factor and isotopic spin interaction are included explicitly in the potential,  $V_2$  becomes

$$V(\vec{r}) = -2\pi \left(1 + \frac{m_{\pi}}{M}\right) \left[ b_0 + b_1 \frac{2\vec{t} \cdot \vec{T}}{A} \right] \rho(\vec{r}).$$

As previously mentioned, it is convenient to account for the remaining corrections by including them as corrections to  $b_0$  rather than introducing additional terms into  $V$ . The main corrections included by the Ericsons are:

1. corrections due to the Fermi motion, including the Lorentz-Lorenz modification. This changes the value of  $b_0$  as determined from free ( $\pi N$ ) scattering by an amount +0.004 ( $\hbar = c = m_{\pi} = 1$ ).
2. corrections due to finite range correlation effects change  $b_0$  by an amount -0.014.
3. corrections due to the real part of the absorption amplitude change  $b_0$  by an amount -0.006 with a large uncertainty of about 20 to 30 percent.

The scattering lengths for free ( $\pi N$ ) scattering have been calculated from experimental ( $\pi N$ ) cross section data by Samaranyake and

Woolcock<sup>34</sup>:

$$b_0 = -0.012 \pm 0.004$$

$$b_1 = -0.097 \pm 0.007.$$

With  $b_0$  corrected as described and similar corrections applied to  $b_1$ , the "effective" values become:

$$b_{0 \text{ eff}} = -0.028 \pm 0.006$$

$$b_{1 \text{ eff}} = -0.10 \pm 0.01.$$

The potential for the nuclear force shift for the 1s state is thus

$$V(\vec{r}) = -2\pi \left(1 + \frac{m_\pi}{M}\right) \left[ b_{0 \text{ eff}} + b_{1 \text{ eff}} \left( \frac{N - Z}{A} \right) \right] \rho(\vec{r})$$

where  $\vec{t} \cdot \vec{T}$  has been replaced by  $(N - Z)/2$ . This potential is used in section V to compute theoretical values for the 1s state nuclear force shifts, which will then be compared with the experimentally determined 1s shifts.

### III. EXPERIMENTAL METHOD

#### A. General Technique

An average of five "pion runs" per target element were taken in which a beam consisting primarily of pions was stopped and the resulting mesic X-rays observed with solid state Ge(Li) and Si(Li) spectrometers. One "muon run" per target element was taken with a beam consisting primarily of muons in order to facilitate the analysis for subtraction of muonic X-ray lines occurring in the pionic X-ray spectra. A Si(Li) spectrometer was used to detect X-radiation from the three lighter targets  $\text{Li}^6$ ,  $\text{Li}^7$ , and  $\text{Be}^9$ , and a Ge(Li) spectrometer, including digital gain stabilization, was used with the three heavier targets  $\text{B}^{10}$ ,  $\text{B}^{11}$ , and  $\text{C}^{12}$ . Each of the X-ray runs was about six hours in duration. Energy calibration runs were taken before and after each of the X-ray runs with calibration sources suspended in the beam and logic requirements similar to those used for X-ray runs.

The major portion of the data was obtained during a four week March-April 1967 run using the 450 MeV synchrocyclotron at the Carnegie-Mellon University. Additional carbon data were taken during a one-week June 1967 run at the 600 MeV synchrocyclotron of the Space Radiation Effects Laboratory (SREL). The counter array, the timing logic, and the stabilization and calibration techniques were the same for both runs. Beam characteristics differed somewhat and are described separately.

## B. Beam Characteristics

A van der Mier type meson channel<sup>35</sup> was used to extract the pion and muon beams from the 450 MeV Carnegie-Mellon machine. The pion beam consisted of about 80 percent pions and 20 percent muons, while the muon beam was 90 percent muons and about 10 percent pions. Both the pion and muon beams were collimated with lead bricks and were about 4 inches in diameter. A range curve taken with CH<sub>2</sub> absorber is shown in Fig. 1. Beam stretching was accomplished with a stochastic cee<sup>36</sup>, resulting in a duty factor of almost unity. An electronic beam gate was used to inhibit the appropriate discriminators in the logic circuitry when the small prompt beam spike was present. The rate of coincidences in counters 1 and 2 (12's) was about  $200 \times 10^3/\text{sec}$  for both the pion and muon beams. The counter array is shown in Fig. 3. The pion stopping rate was  $15 \times 10^3/\text{sec}$  while that for muons was  $3 \times 10^3/\text{sec}$ , both measured for a 6" x 6" x 1/2" carbon target.

The pion and muon beams were extracted from the SREL machine using one quadrupole doublet and a bending magnet. Beam stretching was accomplished using an internal mechanical vibrating target which provided a macroscopic duty factor of about three. The prompt beam was gated out as previously described. The pion beam was 90 percent pure with most of the contamination due to muons, while the muon beam was 90 percent muons and about 10 percent pions. A lead collimator was used to limit the beam diameter to about 5 inches. Rates of  $500 \times 10^3$  12's/sec were obtained with the SREL machine with pion and muon stopping rates of  $90 \times 10^3/\text{sec}$  and  $20 \times 10^3/\text{sec}$ , respectively, as measured with a 6" x 6" x 1" carbon target. A range curve is shown in Fig. 2.

### C. Counters and Counter Geometry

The counter geometry is shown in Fig. 3. Counters 1 and 2 were  $6'' \times 6'' \times 1/4''$  and served as a beam-defining telescope; 3 was  $4'' \times 4'' \times 1/16''$  and was the target-defining counter; 4 was  $12'' \times 12'' \times 1/8''$  and served as an anti-coincidence counter. All counters were constructed from Pilot B plastic scintillant and Lucite light pipes which were mated to Amperex 56 AVP photomultiplier tubes. The scintillants of 3 and 4 were wrapped with aluminized mylar and covered with a thin light-tight wrapping in order to reduce background occurring when a particle stopped in counter 3 or its downstream wrappings or in the upstream wrappings of counter 4. The anti-coincidence efficiency of counter 4 was measured to be 97 percent.

The Čerenkov radiator was water and was viewed from one side by two RCA 8575 photomultiplier tubes whose amplified outputs fed a coincidence circuit operated in the "or" mode (see Fig. 4). The Čerenkov counter was about 50 percent efficient in discriminating against electrons.

$\text{CH}_2$  absorber was used with about two inches of it placed in front of the Čerenkov counter in order to insure that pions and muons would not trigger the counter, while the remainder of the absorber was placed behind the Čerenkov counter. The signal to noise ratio of the observed X-ray spectra and the system resolution were dependent upon the location of the solid state detectors. In order to achieve a maximum signal to noise ratio, the detectors were placed out of the beam path about seven inches from the target center. Minor adjustments in detector position were made for each target. Lead bricks were also used to shield

the detector from the beam. The detector position and shielding served to minimize overload pulses due to high energy particles stopping in the detector. Other precautions such as pole zero cancellation<sup>37</sup> and an overload inhibit discriminator were used for the same purpose and are described in parts E and D of this section.

#### D. Timing and Logic Circuitry

The discussion of the timing circuitry is presented in two parts: a description of the method used to obtain timing pulses from the  $\gamma$ -ray spectrometers, and a description of the beam logic circuitry, including a discussion of the  $^{123}\text{40C} - \gamma$  (fast-slow) timing procedure. A block diagram of the timing circuitry is shown in Fig. 4.

In order to obtain a timing pulse with a fixed time relation to the output signal of the  $\gamma$ -ray spectrometer, both leading edge and crossover timing methods were tested. The TC 130 preamplifier auxiliary output and the first stage output of the TC 200 amplifier were examined as possible sources for timing pulses. The rise time of the preamplifier output pulse was approximately 100 nsec while the fall time was 44  $\mu$ sec. Pulse amplitudes were in the 10 to 50 mV range corresponding to  $\gamma$ -ray energies in the 15 keV to 100 keV region. The TC 200 first-stage output signal characteristics were identical to those of the TC 130 output except that the signal was amplified by a factor of two.

For a given pulse amplitude there were rise time variations due to the location of the  $\gamma$ -ray interaction in the crystal. Events occurring in the middle of the crystal produced fast rising pulses, while those occurring near one of the electrodes produced a pulse whose rise time

was approximately twice as long. In order to minimize rise time variation effects in leading edge timing, it is desirable to trigger the timing discriminator as close to the noise as possible. Leading edge timing tests were made using a low level discriminator triggering in the noise, and an upper level discriminator triggering above the noise. A valid timing pulse was generated when the upper and lower level discriminator outputs (appropriately delayed) were in coincidence. The timing pulse retained the characteristics of the lower level discriminator output pulse.

The zero crossover method was tested using the TC 200 first stage output to drive a Canberra 1410 RC amplifier operated in the double delay line mode. The Canberra amplifier was followed by an ORTEC timing single channel analyzer operated in the differential model which provided a fast timing output in coincidence with the zero crossing point. The baseline and window width of the single channel analyzer were set by using  $\gamma$ -ray sources to bracket the desired energy range. Optimum timing characteristics were achieved with long integration times in the Canberra amplifier.

Timing spectra were recorded in the laboratory using a time to amplitude converter (TAC) and a  $\text{Na}^{22}$  source deposited on plastic scintillant viewed by a phototube to provide a "fast-slow" coincidence for testing purposes. The "fast" (start) signal was provided by the positron ( $\text{Na}^{22}$  beta decays into  $\text{Ne}^{22}$ ) detected by the scintillation counter. The "slow" (stop) signal was provided by Compton-scattered  $\gamma$ -rays detected by the  $\gamma$ -ray spectrometer when the  $\text{Ne}^{22}$  nuclei de-excited. The TAC output was sorted and stored in a 1600-channel spectrum analyzer. The timing spectra consisted of a peak due to positron-de-excitation

$\gamma$ -ray coincidences superimposed on a flat background due to random coincidences. The width of the base of this peak was taken as a measure of the timing resolution. Tests of this nature indicated that, with the available equipment, the crossover method was superior to the leading edge method for both the Ge(Li) and the Si(Li) spectrometers. Timing resolutions of 60 nsec and 30 nsec, respectively, were obtained using the crossover method for the Si(Li) and Ge(Li) spectrometers. Since the energies of the X-rays of interest were relatively small (15 keV to 100 keV), the timing signals from the preamplifier or TC 200 first stage were very close to the high frequency noise band caused by the inherent electronic noise. The ability to amplify and integrate the signal with the Canberra amplifier greatly improved the signal-to-noise ratio and made timing on the low energy pulses more practicable. Attempts to improve the signal-to-noise ratio by integration for leading edge timing purposes led to degradation of pulse rise time and made leading edge techniques less effective. Crossover techniques require timing pulses with constant rise times for optimum performance. Although the output pulse rise time for these detectors was not constant, the rise time variations were slight<sup>38</sup>, since the depletion layers of the detectors used were only about 3 mm to 5 mm.

The beam logic circuitry is included in Fig. 4. Chronetics 100 MHz logic modules were used for all of the fast timing circuitry shown in Fig. 4, except discriminators 8 and 9 and the TAC, which were supplied by EG&G. A Canberra 1410 variable RC amplifier used as a delay line amplifier to provide a bipolar timing pulse was followed by two ORTEC 420 timing single channel analyzers. The timing analyzer was a

TMC 400 channel analyzer while the energy analyzer was a SCIPP 1600 channel analyzer. The delay gate generator was a Canberra Logic Shaper and Delay. The solid dots in Fig. 4 represent inhibit signals.

The inputs to discriminators 1 through 4 were the corresponding outputs of counters 1 through 4, while discriminators 5 and 6 had as their inputs the amplified outputs of the two phototubes ( $\check{C}_1$  and  $\check{C}_2$ ) viewing the Čerenkov counter.

Coincidence units 2 and 3 were operated in the "or" mode as "fan ins" to the DC no input of coincidence unit 1. An output from coincidence unit 1 signified a  $\pi$  stop ( $123\overline{4C}$ ) and served as both a start pulse for the TAC and the "fast" timing input to coincidence unit 4. An output from single channel analyzer 1 indicated that a  $\gamma$ -ray or charged particle had interacted in the detector. This pulse served as a stop pulse for the TAC and a "slow" timing input to coincidence unit 4. The resolving time of coincidence unit 4 was determined by the output widths selected for discriminators 10 and 11. The TAC was operated with a 3  $\mu$ sec resolving time and provided an output only when a stop pulse occurred within 120 percent of the resolving time chosen. Whenever a TAC output was generated, it was accompanied by a time related "valid stop output" which was used as a routing pulse for the timing analyzer. The routing was such that whenever a valid stop output and an output from coincidence unit 4 were simultaneously present at the router, the amplified output of the TAC was routed to the second 200 channels of the 400 channel timing analyzer. When only the valid stop output was present at the router, the amplified TAC output was routed to the first 200 channels. When the fast timing signal ( $123\overline{4C}$ )

and the time related  $\gamma$ -ray (slow timing signal) detected by the spectrometer were out of time at coincidence unit 4, the resulting spectrum displayed in the first 200 channels of the timing analyzer included a peak corresponding to time correlated  $123\overline{4C}$  -  $\gamma$  events and a flat background corresponding to noncorrelated events. However, in this flat background there existed a trough where no counts were present. The width of this trough was determined by the coincidence resolving time of coincidence unit 4. The number of channels separating the trough and the peak was determined by the amount of delay inserted between discriminators 8 and 10. The trough in the first 200 channels was due to random coincidences between the valid stop output and the output of coincidence unit 4 at the router. These coincidences caused the TAC output representing random start and stop pulses arriving simultaneously at coincidence unit 4 to be routed to the second 200 channels and appear there as a square bump with a width equal to that of the trough. Adjustment of the delay between discriminators 8 and 10 caused the trough to move so that it fell over the timing peak which was then routed to the second 200 channels. Fig. 5 shows such a timing spectrum taken under running conditions. The  $123\overline{4C}$  pulses and the time related  $\gamma$ -ray pulse were then in time at coincidence unit 4. The output of coincidence unit 4 then served as a gating pulse which permitted the energy analyzer to process the  $\gamma$ -ray detected in the spectrometer. The width of the trough corresponded to the fast-slow coincidence resolving time. The width of the base of the timing peak resulted from the walk and jitter inherent in the double-delay-line amplifier and the single-channel analyzer used to produce a timing pulse for the  $\gamma$ -ray spectrometers.

For the Ge(Li) spectrometer this width was approximately 60 nsec while for the Si(Li) detector it was 120 nsec as measured under running conditions. Generally, in order to achieve the best signal-to-noise ratio for the X-ray spectra, the trough width would have been adjusted to bracket exactly the base of the timing peak so that no background due to random coincidences would have been included. However, tests were made to determine the signal-to-noise ratio as a function of fast-slow coincidence resolving times, and it was found that the signal-to-noise ratio was not adversely affected for resolving times as large as 320 nsec. This large resolving time was chosen to insure against loss of valid events and misinterpretation of X-ray yields at low energies due to excessively tight timing. The timing logic allowed quick and convenient timing of the fast-slow signals, with continual monitoring of the timing curve on the 400 channel analyzer. It also circumvented the difficulties of long delay times characteristic of delay curves taken for crossover timing. Typical delays were of the order of 1.5  $\mu$ sec and were due mainly to the time interval between an input pulse to the delay line amplifier and the zero crossing of its output. These delays were longer for longer integration time settings on the delay-line amplifier. Visual monitoring of the timing curve provided a convenient method of checking for the existence of  $\gamma$ -rays from exponentially decaying excited nuclear states. If a peak due to a nuclear  $\gamma$ -ray was present in the X-ray spectra, a slight exponential tail was observable on the otherwise Gaussian-shaped timing peak.

The method<sup>39</sup> used to calibrate the TAC is illustrated in Fig. 6. A radioactive source ( $\text{Na}^{22}$ ) produced events which randomly gated the

coincidence unit, allowing pulses of a fixed frequency,  $f$ , from the time mark generator to pass as stop pulses into the TAC. A spectrum of evenly spaced peaks of equal amplitudes was then obtained, with a spacing of  $1/f$  between successive center channels. In the diagram,  $f = 50$  MHz, corresponding to a separation of 20 nsec.

As previously mentioned, precautions were taken to guard against base line shifts in the  $\gamma$ -ray spectrometer due to overload pulses in the detector. These pulses resulted in saturated outputs from both the TC 200 amplifier used in the spectrometer system and the double-delay-line amplifier use for timing purposes. In order to reject such events, single-channel analyzer 2 was used in the integral mode and set to trigger at a level just below the saturation level of the delay line amplifier, whose gain was adjusted so that its output and that of the TC 200 were the same voltage for a given energy. The output of the single channel analyzer 2 was used to gate off discriminators 8 and 9 for approximately 10  $\mu$ sec to allow for base line restoration in the TC 200. With discriminators 8 and 9 gated off, no analyzer gates were generated for this 10  $\mu$ sec period. As previously mentioned, the position of the detector relative to the beam was adjusted so that the overload pulses occurred only infrequently and the overload rejection was relatively efficient.

#### E. $\gamma$ -Ray Spectrometers

Two  $\gamma$ -ray spectrometers were used for X-ray detection: a Si(Li) spectrometer with the  $\text{Li}^6$ ,  $\text{Li}^7$ , and  $\text{Be}^9$  targets and a Ge(Li) spectrometer with the  $\text{B}^{10}$ ,  $\text{B}^{11}$ , and  $\text{C}^{12}$  targets.

The Si(Li) spectrometer consisted of a TMC Si(Li) planar detector 80 mm<sup>2</sup> × 3 mm deep selected for low noise, a modified TC 130 preamplifier with a cooled first stage DC coupled to the detector, a TC 200 RC shaping amplifier with pole-zero cancellation network, and a Victoreen SCIPP 1600 channel analyzer. Pole-zero cancellation was incorporated in the TC 200 amplifier by installing resistors across the first differentiating capacitors so that this RC combination was equal to the decay time (44 μsec) of the preamplifier output pulse. The TC 130 input stage was modified as shown in Fig. 7a. All components shown in Fig. 7a were installed in the same cryostat and were cooled using a copper cold finger in the "dipstick" configuration immersed in a liquid nitrogen reservoir. The input device was a 2N3823 field effect transistor (FET) selected for low noise and cooled to optimum operating temperature using a ceramic rod connected to the copper cold finger as a heat leak. The gauge of the FET ground wire and a thin teflon wrapping on the FET case provided additional means of temperature control. The detector was mounted in an aluminum disk supported by two aluminum rods electrically insulated from the cold finger by small ceramic insulators. In this configuration, the detector was cooled to about 77° K. The detector was operated at -300 volts bias. The gamma ray entry window was a 0.010 inch thick beryllium disk. The thin window and low system noise allowed detection of gamma rays whose energies were as low as 3 keV; however, detector efficiency dropped above 60 keV. The Si(Li) spectrometer was thus well suited for use in detecting the pionic and muonic X-ray radiation from the lithium and beryllium targets.

The TC 200 shaping amplifier was used in the single differentiating mode with differentiation and integration times of 6.4 μsec and 3.2 μsec,

respectively. These time constants resulted in optimum system resolution. System gain was adjusted so that the energy per channel was 77 eV/ch, giving rise to typical unbroadened  $\gamma$ -ray peak widths (FWHM) of about 7.5 channels. System resolution for the Si(Li) spectrometer in a laboratory environment was 0.54 keV FWHM at 26.36 keV as illustrated by the  $\text{Am}^{241}$  spectrum in Fig. 8. This is to be compared to a FWHM of 0.58 keV at the same energy measured under running conditions with an  $\text{AM}^{241}$  source suspended in the beam. Such an  $\text{AM}^{241}$  spectrum is shown in Fig. 9. A detailed description of the Si(Li) spectrometer is given in Ref. 40.

The Ge(Li) spectrometer<sup>41</sup> was similar to the Si(Li) spectrometer, the main differences being the detector itself, the cooling arrangement, and the inclusion of a digital gain stabilizer. The Ge(Li) detector was an encapsulated RCA Ltd. planar device  $3.5 \text{ cm}^2 \times 5 \text{ mm}$  deep mated with a modified TC 130 preamplifier similar to that already described and was operated at 700 volts bias. The preamplifier first stage-detector arrangement is shown in Fig. 7b. Since the Ge(Li) detector was more efficient (due to its size and the higher intrinsic efficiency of germanium) than the Si(Li) detector, count rate problems were more serious. In order to minimize charge pile-up problems in the preamplifier first stage, the Ge(Li) detector was mounted in a positive high voltage configuration so that the FET was positively biased between zero and one volt above ground. High counting rates tended to make the FET bias more positive so that the FET operated with a decreased source-to-gate impedance and excess charge was quickly drained to ground, restoring optimum FET bias. The opposite was true for a

negative bias configuration since the source-to-gate impedance increases with increasing negative bias and the excess charge continues to accumulate, thereby changing the bias from its optimum value and causing charge pile-up. The Ge(Li) detector encapsulation, a 0.020 inch thick soft steel case, the 0.020 inch aluminum  $\gamma$ -ray entry window and the detector dead layer prohibited detection of  $\gamma$ -rays whose energy was much below 30 keV. However, detector efficiency was highest at about 60 keV so that the Ge(Li) spectrometer was used for the detection of pionic and muonic X-rays from the boron and carbon targets. The Ge(Li) spectrometer system resolution was 1.02 keV at 122 keV under laboratory conditions as shown in the Co<sup>57</sup> spectrum of Fig. 10. Under running conditions, the system resolution was 1.10 keV at 100.1 keV as measured with a Ta<sup>182</sup> source suspended in the beam (Fig. 11). The cooling arrangement for the Ge(Li) detector and TC 130 preamplifier front end consisted of an inverted dewar feeding liquid nitrogen through a hollow right angle cold finger to a cooling block. The detector and associated electronics (Fig. 7b) were mounted in an aluminum plate connected to the cooling block by a sapphire rod 1/2 inch in diameter. The FET temperature was controlled by wrapping several layers of teflon tape around its outer casing before mounting it in the aluminum plate. This arrangement allowed the rapid cooling necessary for the Ge(Li) detector. However, there was some degradation of resolution due to bubbling of the liquid nitrogen being fed into the cold finger. This was attributed to peculiarities of the detector encapsulation since no degradation of resolution occurred when a bare Si(Li) detector was mounted in the same cooling configuration. With

the system cooled to liquid nitrogen temperature and the nitrogen removed, system resolution for the Ge(Li) spectrometer was 0.8 keV at 122 keV; however, such performance was possible for only short time periods (about 10 minutes) and thus was not realizable for the long-time X-ray runs. For the Ge(Li) spectrometer single differentiation with integration and differentiation time constants equal to 1.6  $\mu$ sec provided optimum system resolution. Pole-zero cancellation was used in the TC 200 shaping amplifier. For the Ge(Li) spectrometer gain settings,  $\gamma$ -ray unbroadened peak widths of about 6 channels FWHM were observed. For both the Si(Li) and the Ge(Li) spectrometers, the entire range of useable data was recorded from channels 250 to 860 which was the most linear portion of the analyzer. Since separate TC 130's and TC 200's were used with the Si(Li) and Ge(Li) spectrometers, the spectrometers could be interchanged easily with no changes in the control settings.

#### F. Stabilization

The Ge(Li) spectrometer included a Canberra 1495 digital gain stabilizer used for stabilization during both X-ray and calibration runs for the  $B^{10}$ ,  $B^{11}$ , and  $C^{12}$  targets. A 10  $\mu$ C  $Am^{241}$  source taped to the targets provided the stabilization peak at 59.57 keV. The fast-slow timing resolution was 320 nsec, allowing stabilization during X-ray runs on the 59.57 keV  $\gamma$ -rays which were detected in accidental coincidence with a  $\overline{1234C}$ . For calibration runs, the  $\overline{1234C} - \gamma$  coincidence requirement was reduced to only a  $\gamma$ -ray requirement and therefore the calibration and stabilization  $\gamma$ -rays "self gated" the analyzer without

a  $^{123}\text{I}$  signature. The accumulation rate was thus increased for calibration runs (approximately 30 counts per second). The  $\text{Am}^{241}$  source strength was such that the accumulation rate for the stabilization line was equal to or greater than that for the X-ray or calibration lines. Total accumulation rates in the X-ray runs were about 3 counts per second.

The stabilization peak was bracketed by two windows 4 channels wide on either side of the peak. The peak center fell in channel 412 while the windows were set to bracket channels 406 to 410 and 414 to 418 inclusive. An integral scaler recorded counts falling in both windows, summing events until a total of 32 events were recorded, and a differential scaler simultaneously recorded the difference between the number of events recorded in the upper and lower windows. For an integral setting of 32, statistical considerations indicate that the difference in the number of events recorded in the upper and lower windows should not be more than about 10. When the integral scaler recorded a sum of 32 events, the differential scaler was tested. If the differential scaler had at this time registered 10 or fewer events, no gain adjustments were made. However, if the accumulation of events totaled more than 10, a servo-pot in the gain stabilizer changed the system gain by the amount necessary to keep the 59.57 keV peak centered in channel 412. A chart recorder was used to monitor gain changes initiated by the stabilizer.

The 59.57 keV  $\gamma$ -ray line was chosen for stabilization purposes because its energy was such that it accumulated in a channel region free from contamination during the X-ray runs. Thus the peak center was not

subject to changes due to background contamination. The  $\text{Am}^{241}$  source was also convenient because none of the  $\gamma$ -rays generated by this source interfered with the muonic and pionic X-rays detected from the boron and carbon targets. Since only one stabilizer was used, and since stabilization was at a relatively low channel, the drifts caused by slope intercept variation were more pronounced. These drifts, however, were small for the peaks of interest since both calibration peaks and X-ray peaks all fell within 200 channels of the stabilization peak. Errors due to drifts are discussed in section IV.

During calibration runs, the  $\text{Am}^{241}$  59.57 keV stabilization peak was slightly contaminated by the  $K_{\alpha 1}$  and  $K_{\alpha 2}$  electronic X-rays of  $\text{W}^{182}$  formed from the  $\text{Ta}^{182}$  calibration source (see Fig. 11). This contamination contributed about 16 percent of the total integrated counts in the 59.57 keV peak and gave rise to a very small systematic gain increase for calibration runs. Corrections for this effect and corresponding error enhancement are discussed in section IV.

Stabilization was not used with the Si(Li) spectrometer since no sources were available that could provide a stabilization peak without also generating  $\gamma$ -rays which would interfere with the X-ray measurements for the three lighter target elements. Gain and intercept drifts were observed for spectra recorded with the Si(Li) spectrometer and are also discussed in section IV.

#### G. Targets

1.  $\text{Li}^6$ : separated by the Oak Ridge Isotope Division and consisting of 95.63 percent  $\text{Li}^6$  and 4.37 percent  $\text{Li}^7$  totaling 99.9 percent

lithium supplied in sheet form, covered with a light grease and wrapped in polyvinyl film. Target dimensions were 5" x 5" x 1".

2.  $\text{Li}^7$ : supplied by United Mineral and Chemical Corporation in foil form and consisting of the natural abundances of 92.58 percent  $\text{Li}^7$  and 7.42 percent  $\text{Li}^6$ , covered with a light grease. Target dimensions were 6" x 6" x 1".

3.  $\text{Be}^9$ : supplied in sheet form consisting of 98.0 percent total beryllium of which 100 percent was  $\text{Be}^9$ . Sheets were sandwiched to give a target of dimensions 5" x 5" x 5/8".

4.  $\text{B}^{10}$ : separated at Oak Ridge Isotope Division, consisting of 93.16 percent boron of which 92.67 percent was  $\text{B}^{10}$  and 7.33 percent was  $\text{B}^{11}$  and supplied in powdered form. Target dimensions were 6" x 6" x 3/8".

5.  $\text{B}^{11}$ : supplied by United Mineral and Chemical Corporation in powdered form and consisting of 99.8 percent boron of which 80.22 percent was  $\text{B}^{11}$  and 19.78 percent  $\text{B}^{10}$  (natural abundances). Target dimensions were 7" x 7" x 3/4".

6.  $\text{C}^{12}$ : consisting of 99.89 percent carbon of which 98.89 percent was  $\text{C}^{12}$  and 1.11 percent  $\text{C}^{13}$ . Target dimensions were 6" x 6" x 1/2" for the CMU and 6" x 6" x 1" for the SREL runs.

All of the targets except the  $\text{Be}^9$  and  $\text{C}^{12}$  targets were mounted in thin air-tight plastic holders.

#### H. Calibration

The 26.36 keV and the 59.57 keV nuclear  $\gamma$ -rays from  $\text{Np}^{237}$ , formed from  $\text{Am}^{241}$  by alpha decay, served as calibration standards for the

Si(Li) spectrometer used to detect the pionic and muonic  $K_{\alpha}$  X-rays produced in the  $\text{Li}^6$ ,  $\text{Li}^7$ , and  $\text{Be}^9$  targets. The X-ray lines produced in these targets ranged in energy from 18 to 43 keV and were, in most cases, bracketed by the calibration peaks. The calibration energies have been precisely measured by Day<sup>42</sup>, using a bent crystal spectrometer, to be  $26.363 \pm 0.014$  keV and  $59.568 \pm 0.017$  keV. As described in part A of this section, calibration runs were taken immediately before and after each X-ray run. The  $\text{Am}^{241}$  calibration runs were each about 10 minutes long, with the source-to-detector distance adjusted to give a minimum of 1000 counts in the center channels of each of the 26.36 and 59.57 keV peaks. The calibration source strength was approximately 10  $\mu\text{C}$ . During the 10-minute accumulation time, the background due to contamination from the beam was negligible, and the calibration peaks were clean and well separated, as shown in Fig. 9.

A 1  $\mu\text{C}$   $\text{Ta}^{182}$  source provided calibration standards for the Ge(Li) spectrometer used in the detection of pionic and muonic X-rays produced in the  $\text{B}^{10}$ ,  $\text{B}^{11}$ , and  $\text{C}^{12}$  targets.  $\text{Ta}^{182}$  beta decays into  $\text{W}^{182}$  which de-excites, emitting  $\gamma$ -rays whose energies range from 60 keV to 1.5 MeV. Since the energies of the mesic X-rays from the boron and carbon targets ranged from 52 to 94 keV, only three of the less energetic  $\text{W}^{182}$   $\gamma$ -rays were used for calibration purposes. The energies of these  $\gamma$ -rays have been measured<sup>43</sup> to be  $67.751 \pm 0.001$ ,  $84.693 \pm 0.001$  and  $100.107 \pm 0.001$  keV. The 59.57 keV  $\text{Np}^{237}$   $\gamma$ -ray used for stabilization was also analyzed for calibration purposes. In addition, a  $\text{Hg}^{203}$  source was used to provide a 279 keV  $\gamma$ -ray for calibration at the high end of the analyzer scale; however, this  $\gamma$ -ray line was not used in the data analysis. Since the

59.57 keV line was contaminated by electronic X-rays from  $W^{182}$  and the 84.69 keV line of  $W^{182}$  was contaminated by the  $K_{\beta 1}$  and  $K_{\beta 2}$  electronic X-rays of  $Tl^{203}$  formed from  $Hg^{203}$  by  $\beta$ -decay, only the 67.75 and 100.12 keV  $W^{182}$   $\gamma$ -rays were used for calibration purposes in the final analysis. However, the two contaminated lines were analyzed and used in conjunction with the 67.59 and 100.12 keV lines as a self-consistency check on the calibration analysis (see section IV) and for system linearity measurements. The procedure for calibrating the Ge(Li) spectrometers with  $Ta^{182}$ ,  $Am^{241}$ , and  $Hg^{203}$  sources was identical to that used for the Si(Li) detector, with the exception of the accumulation time. The period for accumulation was 1/2-hour, this being determined by the requirement that there be approximately 500 counts in the center channel of the weakest useable peak, the 84.69 keV line. A typical calibration spectrum for the Ge(Li) spectrometer is shown in Fig. 11.

### I. System Linearity

System linearity was measured in the laboratory using a precision — 60 Hz pulser designed by J. A. Biggerstaff of Oak Ridge National Laboratory. The specifications on pulser output were linearity and reproducibility to a few parts in  $10^5$ . The pulser output was a fast rising (approximately 50 nsec) pulse with a 100  $\mu$ sec decay time and was similar in shape to the pulses generated by the detectors. Pulse amplitude was variable from 0 to 5 volts by means of a three-stage decapot. Both the Si(Li) and Ge(Li) spectrometers were tested by using the precision pulser to deposit charge on a 0.5 pF test capacitor connected to

the gate lead of the cooled FET in the preamplifier first stage. The test capacitor was installed within the cooling cryostat in order to insure temperature stability. Gain settings used during the run were reproduced, and a Tennelec temperature-stable attenuator was inserted between the precision pulser and the test pulse input in order to reduce the test pulse amplitude and still allow use of the full range of the decapot. In this manner the decapot could be varied over 70 percent of its range to produce pulser peaks whose centers were separated by as little as five channels and distributed over the entire channel range occupied by the X-ray peaks observed during the run. Linearity corrections for both systems were made following the method of Heath *et al.*,<sup>44,45</sup> and Black<sup>46</sup>.

For the Si(Li) spectrometer, the channel range of interest was 300 to 900. Several separate linearity runs were taken in which the pulser amplitude was varied so that the peaks were recorded at intervals of 17 channels over this entire channel range. The pulser peaks were typically 6 channels wide with a total of about 1000 counts in the center channel. The pulser peaks were least-squares fitted to a Gaussian function, the centers being determined to within 0.05 channels. Two pulser peaks, one falling in channel 446, approximately the center channel of the 26.36 keV calibration peak, and the other falling in channel 882, approximately the center of the 59.57 keV calibration peak, were chosen as "anchor points" on a plot of pulser amplitude setting versus center channel. These anchor points are represented by the circles in Fig. 12, while the remaining pulser peak centers fall along the curved line representing the actual system response. The

deviation of the actual response from a linear one has been greatly exaggerated in this figure for the purposes of illustration. The slope and intercept of the straight line defined by these anchor points were computed and the deviations of the remaining peak centers from this straight line were plotted as in Fig. 13 as channel correction versus channel number. These points were fitted to a second-order polynomial so as to give the channel correction as a function of channel number for any channel. In this manner, the calibration and X-ray peak centers were corrected for system nonlinearities, thereby linearizing the system response. The choice of anchor points was quite arbitrary. However, since the anchor points were chosen to be within a few channels of the calibration line centers, the energy per channel remained approximately constant and channel corrections could be estimated in terms of energy corrections. Thus from Fig. 13, the maximum correction due to system nonlinearities for the Si(Li) spectrometer was about 27 eV with typical corrections of approximately 10 eV.

Linearity tests for the Ge(Li) spectrometer were identical to those described for the Si(Li) system; however, the channel range of interest was the smaller interval 280 to 740. For the Ge(Li) spectrometer tests, pulser peaks were recorded about every 10 channels. Four linearity runs were taken for the Ge(Li) spectrometer, and each run was analyzed and compared with the others to determine reproducibility. A typical correction curve for the Ge(Li) spectrometer is shown in Fig. 14. Over most of the range of interest the system was found to be linear, with significant deviations (about 40 eV) occurring in the lower channel region, where the  $B^{10}$  and  $B^{11}$  muonic  $K_{\alpha}$  X-rays were recorded. Anchor

points chosen in this analysis were near the center channels of the 59.57 and 100.12 keV calibration peaks. Unfortunately, during these linearity tests, the TC 200 amplifier used with the Ge(Li) detector failed, and the TC 200 amplifier from the Si(Li) spectrometer was substituted to complete the tests.

To check the results of these tests, the four calibration lines used with the Ge(Li) spectrometer during the X-ray run were analyzed to give an estimate of the system nonlinearity. All of the calibration runs were analyzed in a manner similar to the analysis of the pulser peaks, and the results indicated that the system was linear to within 0.25 channels from channel 412 to 624. This large uncertainty was due to background subtraction in the calibration peak analysis.

Since system linearity was measured after the run and not under running conditions, the response of both the Ge(Li) and Si(Li) systems was assumed to be known to within only 0.25 channels. This large uncertainty is a considerable overestimate since the correction curves shown in Figs. 13 and 14 indicate that the system response was actually known to within 0.05 channels.

## IV. ANALYSIS OF DATA

### A. General Technique

A least-squares fitting program, incorporating a background-subtraction subroutine and allowing fits to functions defined by as many as twelve parameters, was used with an IBM 360 model 50 computer for analysis of calibration and X-ray spectra. In general, for a given element, energies for both pionic and muonic  $K_{\alpha}$  X-ray transitions were determined from the analysis of the pionic and muonic  $K_{\alpha}$  lines appearing in the "pion spectra." In addition, the muonic  $K_{\alpha}$  line appearing in the "muon spectra" taken for background subtraction purposes was also analyzed to give the muonic  $K_{\alpha}$  X-ray transition energy.

The muonic X-ray and calibration lines, corrected for background contamination, were fitted to a Gaussian function plus a linear background term. The pionic  $K_{\alpha}$  X-ray lines were naturally broadened due to fast nuclear capture of the pion so that these lines were a complex mixture of Gaussian and Lorentzian functions, the Lorentzian shape arising from the capture process and the Gaussian shape resulting from both the charge collection processes in the detector and the electronic noise distribution in the preamplifier-amplifier system. In order to determine the centers of the background-corrected pionic  $K_{\alpha}$  peaks, each pionic peak was fit separately to both a Gaussian function with a linear background term and also to a Lorentzian function plus linear background. In every case, the centers as predicted by the Gaussian and Lorentzian fits agreed within their statistical errors, and, as a final value, a simple average of the two was taken and the larger of the two errors assigned.

For each spectral line, the range of channels included in the fit was varied in order to determine the dependence of the peak center on the functional fit. The peak centers were observed to remain constant within the statistical error over all ranges examined except those which were so narrow that the background included was not definite enough to allow a reasonable fit to be assumed straight line. As a test of the data over these narrow ranges, the slope and intercept of straight line background were set at the values obtained from a fit over a wide channel range. With these parameters fixed, the centers obtained from fits over the narrow ranges were constant and equal to those obtained from wide-range fits. Generally,  $\chi^2$ 's obtained for the least squares fits were approximately equal to the number of data points included. For the worst cases,  $\chi^2$ 's were not more than twice the number of data points.

In order to simplify the description of the background-subtraction process, the following definitions are made:

1. The raw spectrum is that spectrum containing the contaminated peak from which the background is to be subtracted.
2. The background spectrum is that spectrum containing the background peaks (themselves uncontaminated) which are to be subtracted from the raw spectrum.
3. The spectrum of interest is that spectrum remaining after the background spectrum has been subtracted from the raw spectrum, and the peak of interest is the peak remaining after the background peaks have been subtracted from the contaminated peak.

4. The reference line, or peak, is a line generated by the source of background and appearing uncontaminated in both the raw and background spectra.

In all cases for which background subtraction was necessary, it was possible to obtain a background spectrum and a reference line. The centers, widths, and amplitudes of the background peaks and of the reference line, all appearing in the background spectrum, were determined using the least-squares fitting program. The energies of these lines were determined from associated calibration runs. The center and amplitude of the reference line appearing in the raw spectrum were also determined from the least squares fitting program, and the energy per channel was determined for the raw spectrum using associated calibration runs. With these parameters determined, the centers and amplitudes of the background peaks appearing in the raw spectrum were calculated as follows:

$$X_1 = X_0 - (E_0 - E_1)/m,$$

$$A_1 = a_1 N,$$

$$N = A_0/a_0,$$

where

$m$  = energy per channel in the raw spectrum,

$E_1$  = energy of the  $i^{\text{th}}$  background line,

$a_1$  = amplitude of the  $i^{\text{th}}$  background line appearing in the background spectrum,

$A_1$  = amplitude of the  $i^{\text{th}}$  background line appearing in the raw spectrum,

$X_1$  = center of the  $i^{\text{th}}$  background line appearing in the raw spectrum,

$E_0$  = energy of the reference line,

$X_0$  = center of the reference line appearing in the raw spectrum,

$A_0$  = amplitude of the reference line appearing in the raw spectrum, and

$a_0$  = amplitude of the reference line appearing in the background spectrum.

The widths of unbroadened spectral lines were well known and were accordingly assigned to the background peaks appearing in the raw spectrum.

With these centers, widths, and amplitudes, the background contamination appearing in the raw spectrum was generated and subtracted channel-by-channel from the raw spectrum, leaving only the peak of interest and a random background to be fit with an appropriate function. Since the background parameters were assumed to be known exactly in the subtraction process, the statistical error on the center of the peak of interest was unrealistic, and therefore an additional error introduced by the background subtraction process was computed. The worst case of background contamination, the  $C^{12}$  pionic  $K_\alpha$  line, was examined for this purpose.

The background parameters ( $X_1$ ,  $A_1$ , and widths) were varied within their errors, the background subtraction process repeated, and the background-corrected  $C^{12}$  pionic  $K_\alpha$  line refit to determine the dependence of its center on the values of the background parameters. The total excursion of the peak center due to variation in the background parameters was then added linearly to the statistical error on the center to take into account uncertainties in background subtraction. For this worst case, the total excursion of the peak center was never greater than the statistical error on the center. For all other cases in which background subtraction was necessary, the error incurred was estimated on a percentage basis using the background subtraction error computed for the  $C^{12}$  pionic

$K_{\alpha}$  line as a standard. Since the widths and centers of the background peaks were precisely known, most of the error arising from background subtraction was due to uncertainties in the amplitudes of the background peaks. Thus, for a given case, the ratio of the sum of the amplitudes of the background peaks occurring under the contaminated peak to the sum of the amplitudes of the background peaks occurring under the  $C^{12}$  pionic  $K_{\alpha}$  line was computed. The error incurred by the background subtraction process was then taken to be the product of this ratio and the error due to background subtraction computed for the  $C^{12}$  pionic  $K_{\alpha}$  line. These errors are included in the discussion of the analysis of the individual lines in part C of this section.

Isotopic contamination in the  $B^{11}$  target was taken into account in the background analysis. However, for targets in which the contamination was less than 8 percent ( $Li^6$ ,  $Li^7$ , and  $B^{10}$ ), no corrections were made. For these targets, the errors on the final values of the X-ray energies were enhanced by 10 eV. All calibration and X-ray peak centers were also corrected for system nonlinearities and the errors enhanced as required, as outlined in section III.

As previously mentioned in section III, analysis of the calibration runs, taken before and after each X-ray run, indicated that there were drifts in the calibration peak centers due to temperature variations in the laboratory. Fig. 21 shows these drifts for the calibration peak centers used in the  $Li^6$ ,  $Li^7$ , and  $Be^9$  X-ray analysis. The solid black triangles along the horizontal axis indicate X-ray runs. Time intervals between calibration runs which bracketed X-ray runs were about six hours. Figs. 22 and 23 show similar plots for calibration peak centers used for

the  $B^{10}$ ,  $B^{11}$ , and  $C^{12}$  X-ray analysis. Drifts during calibration runs were negligible, since the accumulation times were short. In order to correct for drifts occurring during the period of one X-ray run, an averaging process for obtaining peak centers was employed. Under the assumption that the drifts were slow and linear, the peak centers of corresponding lines occurring in the calibration spectra obtained before and after a given X-ray run were averaged. This provided one set of calibration peak centers for each X-ray run. Although computer fits gave centers to within approximately 0.07 channels, it was necessary to assign a larger error to the averaged centers in order to take the effects of drifts into account. For this purpose, the magnitude of the drift of each of the centers of lines accumulated in calibration runs bracketing a given X-ray run was computed. The magnitude of the drift was then compared to the statistical error on the center of the mesic X-ray lines recorded in the X-ray run bracketed by the calibration runs. The larger of these two quantities was then selected to be the error on the center of the averaged calibration peak. These calculations were done separately for each calibration line. The minimum errors thus calculated were typically 0.2 channels.

As mentioned in section III, there was a small systematic gain increase for calibration runs taken with the Ge(Li) spectrometer due to contamination of the 59.57 keV stabilization line. This contamination occurred during calibration runs but not during X-ray runs and was due to the 59.318 keV  $K_{\alpha 1}$  and 57.982 keV  $K_{\alpha 2}$  electronic X-rays of  $W^{182}$  formed by beta decay from the  $Ta^{182}$  calibration source. During calibration runs, these X-rays contributed about 16 percent of the total

integrated counts under the 59.57 keV stabilization peak and resulted in the formation of the low-energy tail on the stabilization peak shown in Fig. 11. In order to estimate the magnitude of the gain shift caused by this low-energy tail, laboratory tests were made on the Ge(Li) spectrometer with the same gain settings used during the run. With the 59.57 keV line again used for stabilization purposes, the  $\text{Co}^{57}$  122 keV line was accumulated with and without the  $\text{Ta}^{182}$  source present. Systematic shifts of  $+0.37 \pm 0.37$  channels were observed in the 122 keV line center when the  $\text{Ta}^{182}$  source was present. From the results of these tests, the calibration line centers were corrected for stabilization effects. These corrections are listed separately for each of the Ge(Li) spectrometer calibration lines in part B of this section. The calibration line centers were thus corrected for drifts, system nonlinearities, and for background and stabilization effects as required. The errors assigned to the calibration line centers included contributions from background subtraction and uncertainties in drift and stabilization effects.

With the calibration and X-ray line centers computed in the manner described, the individual X-ray centers and their corresponding averaged calibration runs were then analyzed separately for the energies of the pionic and muonic  $K_{\alpha}$  X-ray lines. The 26.36 and 59.57 keV calibration lines were used as calibration standards to compute the energies of the pionic and muonic X-ray lines observed for the  $\text{Li}^6$ ,  $\text{Li}^7$ , and  $\text{Be}^9$  targets. The 67.75 and 100.12 keV calibration lines were used to compute the  $\text{B}^{10}$ ,  $\text{B}^{11}$ , and  $\text{C}^{12}$  pionic and muonic X-ray energies. For each X-ray run, the energy per channel was determined from the corresponding averaged

calibration runs, and with the better known of the two averaged calibration lines used as an energy reference, the X-ray energy and its error were computed. The pionic and muonic  $K_{\alpha}$  X-ray energies obtained for each run for a given target element were then compounded in the usual manner<sup>61</sup> to give final values for the energies of the pionic and muonic  $K_{\alpha}$  X-rays in that element. Results of these analyses are given in Tables I - VI. The errors listed in these tables include contributions from the statistical error inherent in the least-squares analysis and uncertainties arising from background subtraction, drifts, and stabilization effects. The compounded errors listed in Tables I - VI do not include contributions arising from uncertainties in system linearity. In order to account for uncertainties in system linearity and other possible undetected systematic errors, the compounded errors for the  $B^{10}$ ,  $B^{11}$ , and  $C^{12}$  X-ray energies were further increased by 60 eV, while those for the  $Li^6$ ,  $Li^7$ , and  $Be^9$  X-ray energies were increased by 20 eV (corresponding to 0.3 channels in both cases). In addition, these compounded errors were increased for isotopic contamination effects as previously described. The pionic and muonic  $K_{\alpha}$  X-ray energies and the final errors thus computed are listed in Table VII under E (W&M).

The  $\gamma$ -ray spectrometers were tested for rate dependence using calibrated sources. Gamma-ray spectra were recorded for a wide range of accumulation rates, and line centers were obtained by least-squares analysis. These tests indicated that shifts in line centers due to rate-dependent effects were negligible for counting rates of less than 2000 counts/sec. As a further check on rate dependence, a  $Be^9$  X-ray run

taken simultaneously with accidentally-gated calibration lines was analyzed for the pionic and muonic  $K_{\alpha}$  X-ray energies. These energies agreed with the energies obtained for the same transitions using the  $\text{Be}^9$  runs bracketed by calibration runs, indicating that rate dependent effects were minimal and that the averaging process for calibration lines was valid. Also, agreement between the  $\text{C}^{12}$  pionic and muonic X-ray energies measured at CMU and those measured at SREL, where the pion stopping rate was a factor of six larger, indicated that rate-dependent effects were not significant.

#### B. Analysis of Calibration Lines

The 26.36 and 59.57 keV lines used to calibrate the Si(Li) spectrometer were both free from background contamination. For each of these lines, peak centers were determined by least-squares fits to a Gaussian plus a linear background term. A typical calibration spectrum is shown in Fig. 9.

Each of the two calibration lines used for the Ge(Li) spectrometer is described in turn:

1.  $\text{W}^{182}$  67.75 keV calibration line. The spectrum generated by the  $\text{Ta}^{182}$  source included  $\text{W}^{182}$  67.75 and 65.72 keV  $\gamma$ -rays whose centers were separated by approximately 8.5 channels. The observed ratio of their respective amplitudes was about 10/1. The 67.244 keV  $K_{\beta 1}$  and the 66.951 keV  $K_{\beta 2}$  electronic X-rays<sup>47</sup> of  $\text{W}^{182}$  also fell in this energy region. However, they were very weak and could be neglected in this analysis. In order to determine the center of the 67.75 keV peak for calibration purposes, the 67.75 and 65.72 keV

lines were fit to the sum of two Gaussians plus a linear background term. Only the 67.75 keV line was used for calibration purposes since the error on its center was smaller than that on the 65.72 keV line center. The center of the 67.75 keV line was corrected by -0.04 channels for stabilization effects and the error on the center was enhanced by 0.04 channels.

2. W<sup>182</sup> 100.12 keV calibration line. The W<sup>182</sup> 100.12 keV line was uncontaminated. Its center was determined by a least-squares fit to a Gaussian plus a linear background. The peak center was corrected by -0.24 channels for stabilization effects and the error enhanced by 0.24 channels.

### C. Analysis of X-ray Lines

The analysis of the pionic and muonic  $K_{\alpha}$  X-ray lines and the spectrum analysis needed for the computation of background parameters are discussed separately for each of the target elements.

1. Li<sup>6</sup>. A total of five separate pion runs and one muon run were taken for Li<sup>6</sup>. Typical spectra are shown in Fig. 15.

The pionic  $K_{\alpha}$  line in Li<sup>6</sup> was contaminated by the muonic  $K_{\beta}$  and  $K_{\gamma}$  lines in Li<sup>6</sup> and the pionic  $L_{\beta}$  line in C<sup>12</sup>, the last occurring from pion stops in the target wrappings and counter 3. Because the muonic  $K_{\alpha}$  line was contaminated by the C<sup>12</sup> pionic  $L_{\alpha}$  line, it was not used as a reference line. Instead, the muonic  $K_{\beta}$  line was used as a reference line to subtract the muonic  $K_{\gamma}$  peak, which itself was buried under the pionic  $K_{\alpha}$  peak. In order to determine the center and amplitude of the muonic  $K_{\beta}$  line in the

pionic spectrum, this line and the pionic  $K_{\alpha}$  line (not corrected for background) were fit to the sum of two Gaussians plus a linear background term. The muonic  $K_{\alpha}$ ,  $K_{\beta}$ , and  $K_{\gamma}$  lines in the muonic spectrum were analyzed, and, using the muonic  $K_{\beta}$  peak as a reference line, the muonic  $K_{\gamma}$  line was subtracted from the contaminated pionic  $K_{\alpha}$  line. In addition, the muonic  $K_{\beta}$  line itself, which partially contaminated the pionic  $K_{\alpha}$  line, was subtracted. This left only the  $C^{12}$  pionic  $L_{\beta}$  line to be removed from the  $Li^6$  pionic  $K_{\alpha}$  line. In order to predict the center, width, and amplitude of the  $C^{12}$  pionic  $L_{\beta}$  line, a  $C^{12}$  target was placed in the pion beam, and the  $C^{12}$  pionic  $L_{\alpha}$  and  $L_{\beta}$  lines were observed with the Si(Li) spectrometer. The centers, widths and amplitudes of both these lines were obtained by a least-squares analysis. The  $C^{12}$  pionic  $L_{\alpha}$  line was used as the reference peak, after the contaminating  $Li^6$  muonic  $K_{\alpha}$  line had been subtracted in the pion spectrum by using the  $Li^6$  muonic  $K_{\beta}$  line as a reference. With the  $C^{12}$  pionic  $L_{\alpha}$  line as a reference, the contaminating  $C^{12}$  pionic  $L_{\beta}$  line, appearing under the  $Li^6$  pionic  $K_{\alpha}$  line, was subtracted. Finally, the remaining contamination-free  $Li^6$  pionic  $K_{\alpha}$  line was analyzed with both Gaussian and Lorentzian fits as previously described. The statistical error on the center of this line was enhanced by 0.14 channels due to uncertainties in the parameters which entered in the background subtraction analysis.

As noted, the muonic  $K_{\alpha}$  line in the pion spectra was contaminated by the  $C^{12}$  pionic  $L_{\alpha}$  line. The  $C^{12}$  pionic  $L_{\alpha}$  line, whose center, width, and amplitude were determined for the background

analysis of the  $\text{Li}^6$  pionic  $K_\alpha$  line, was subtracted from the contaminated  $\text{Li}^6$  muonic  $K_\alpha$  line. The low energy tail on the  $\text{Li}^6$  muonic  $K_\alpha$  line was attributed to  $180^\circ$  Compton scattering in the target and was Gaussian in shape. This effect was enhanced for the muonic  $K_\alpha$  lines in the pionic spectra since there was also a contribution from backscattering of the  $\text{C}^{12}$  pionic  $L_\alpha$  X-rays at approximately the same energy. The backscatter peak and the  $\text{Li}^6$  muonic  $K_\alpha$  line were fit to the sum of two Gaussians plus a linear background term. The statistical errors on the centers of the muonic  $K_\alpha$  lines in the pionic spectra were enhanced by 0.82 channels because of uncertainties in the background parameters.

2. Li<sup>7</sup>. Typical  $\text{Li}^7$  pionic and muonic spectra are shown in Fig. 16. Four separate pion runs and one muon run were taken for  $\text{Li}^7$ . The analysis of the pionic and muonic  $K_\alpha$  lines was, in all aspects, the same as that for the corresponding peaks in the  $\text{Li}^6$  spectra.

3. Be<sup>9</sup>. Five separate pion runs and one muon run were taken for  $\text{Be}^9$ . Typical pionic and muonic spectra are shown in Fig. 17. The  $\text{Be}^9$  pionic  $K_\alpha$  line was contaminated by the  $\text{Be}^9$  muonic  $K_\beta$  and  $K_\gamma$  lines. The muonic  $K_\alpha$  line occurring in the pionic spectra of  $\text{Be}^9$  was uncontaminated, and this line was used as a reference to remove the muonic  $K_\beta$  and  $K_\gamma$  contamination from the pionic  $K_\alpha$  line. The pionic  $K_\alpha$  line was then fit separately to Lorentzian and Gaussian functions, and the statistical error on the center enhanced by 0.06 channels because of uncertainties in the background parameters.

4. B<sup>10</sup>. Typical B<sup>10</sup> pionic and muonic spectra are shown in Fig. 18. A total of five separate pion runs and one muon run were taken for B<sup>10</sup>. The B<sup>10</sup> muonic K<sub>β</sub> and K<sub>γ</sub> lines were removed from the pionic K<sub>α</sub> line in B<sup>10</sup> by using the muonic K<sub>α</sub> line as a reference line. The pionic K<sub>α</sub> line and the muonic K<sub>β</sub> line centers were separated by approximately twenty channels, whereas the muonic K<sub>γ</sub> line was totally obscured by the pionic K<sub>α</sub> peak. The muonic K<sub>δ</sub> line was very weak and was therefore neglected in the background analysis. After background subtraction, the contaminant-free pionic K<sub>α</sub> peak was analyzed as previously described. The statistical error on the pionic K<sub>α</sub> line center was enhanced by 0.03 channels due to uncertainties in the background-subtraction parameters.

5. B<sup>11</sup>. Three separate pion runs and one muon run were taken for B<sup>11</sup>. Typical spectra are shown in Fig. 19. The background analysis was similar to that for B<sup>10</sup>, except that for B<sup>11</sup> the 19.78 percent B<sup>10</sup> isotopic contamination was removed. A Gaussian function whose amplitude was 19.78 percent of the amplitude of the contaminated B<sup>11</sup> pionic K<sub>α</sub> line corrected for muonic background, and whose center and width were determined from the B<sup>10</sup> pionic K<sub>α</sub> line energy and width, was subtracted from this background-corrected B<sup>11</sup> pionic K<sub>α</sub> line. The remaining B<sup>11</sup> pionic K<sub>α</sub> line was then analyzed as previously described. The muonic K<sub>α</sub> line was similarly corrected for isotopic contamination. The statistical error on the center of the pionic K<sub>α</sub> line was enhanced by 0.13 channels, and the error on the muonic K<sub>α</sub> line center was increased by 0.07 channels due to background-subtraction uncertainties.

6. C<sup>12</sup>. Six separate pion runs and two muon runs were taken for C<sup>12</sup>. Fig. 20 shows typical pionic and muonic spectra. The C<sup>12</sup> pionic K<sub>α</sub> line was contaminated by the muonic K<sub>β</sub>, K<sub>γ</sub>, and K<sub>δ</sub> lines in the same element. The muonic K<sub>α</sub>, K<sub>β</sub>, K<sub>γ</sub>, and K<sub>δ</sub> lines appearing in the muonic spectra were each fit to a Gaussian plus linear background term, as was the uncontaminated muonic K<sub>α</sub> line appearing in the pionic spectra. The muonic K<sub>α</sub> line was used as a reference line, and the muonic K<sub>β</sub>, K<sub>γ</sub>, and K<sub>δ</sub> lines were subtracted from the contaminated pionic K<sub>α</sub> line. The statistical error on the center of the C<sup>12</sup> pionic K<sub>α</sub> line was increased by 0.17 channels because of background uncertainties.

## V. RESULTS AND THEORETICAL CONSIDERATIONS

The pionic and muonic  $K_{\alpha}$  X-ray energies determined in this work are listed in Table VII and compared to measurements made by groups at CERN<sup>8,9</sup> and Berkeley<sup>5</sup>. The energies determined in this work and those measured by the CERN group agree to within one standard deviation, except for the  $C^{12}$  pionic  $K_{\alpha}$  X-ray energies which are in agreement to within two standard deviations. In most cases, the X-ray energies measured by the Berkeley group are consistently lower than those obtained in this work and by the CERN group. The measurements reported here represent a substantial improvement in precision over these previous measurements.

The remainder of this section consists of a description of how the measured pionic and muonic  $K_{\alpha}$  X-ray energies are used to determine the experimental nuclear force shift for each of the target elements. These shifts are then compared to the shifts predicted from the theory of the Ericsons<sup>30,31</sup>. Energies for pionic and muonic  $K_{\alpha}$  transitions are computed using the Klein-Gordon and Dirac equations, respectively. Calculations of vacuum polarization effects for these transitions have been done according to the method of Mickelwait and Corben<sup>13</sup>. The Coulomb shifts for the pionic  $1s$  levels are computed according to Pustovalov<sup>12</sup> using nuclear radii determined from electron scattering. As a consistency check, these Coulomb shifts are also calculated with nuclear radii determined from the muonic X-ray data. The differences between the theoretically-predicted pionic  $K_{\alpha}$  transition energies corrected for both Coulomb and vacuum polarization effects and the experimentally

measured energies for the same transitions are attributed to the nuclear force shift.

#### A. Computation of Pionic and Muonic $K_{\alpha}$

##### Transition Energies

The pionic  $K_{\alpha}$  transition energies were computed for each target element using the energy levels as given by the Klein-Gordon equation:

$$E_{n,l} = -\frac{\mu c^2}{2n^2}(Z\alpha)^2 \left[ 1 + \left(\frac{Z\alpha}{n}\right)^2 \left( \frac{n}{l + \frac{1}{2}} - \frac{3}{4} \right) \right],$$

to terms of order  $\alpha^4$ . The results of these calculations are listed in the column  $E_{KG}$  of Table VIII.

The muonic  $K_{\alpha}$  X-ray transition energies were similarly computed using energy levels determined from the Dirac equation:

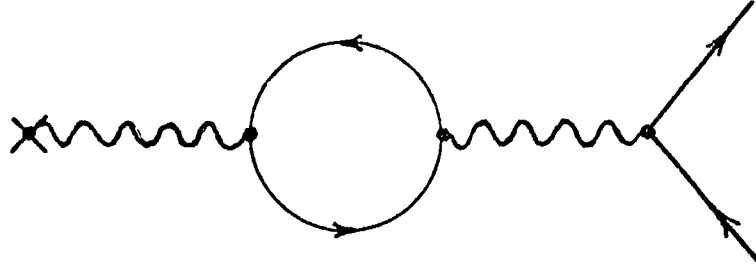
$$E_{n,j} = -\frac{\mu c^2}{2n^2}(Z\alpha)^2 \left[ 1 + \left(\frac{Z\alpha}{n}\right)^2 \left( \frac{n}{j + \frac{1}{2}} - \frac{3}{4} \right) \right],$$

also to terms of order  $\alpha^4$ . Fine structure splitting (about 10 eV for the 2p level of  $C^{12}$ ) was neglected in the analysis. The results of these calculations are listed in Table IX(a) under  $E_D$ .

#### B. Vacuum Polarization Corrections

Vacuum polarization corrections were computed according to the method of Mickelwait and Corben<sup>13,14</sup>. Corrections to the 1s and 2p levels were calculated for each target element. The effect of the finite size of the nucleus on the vacuum polarization calculations for the 1s level was included in the perturbing potential, and unperturbed hydrogenic wave functions were used in the analysis. The calculations were made using

the second order term in the S matrix expansion for the interaction of a charged particle with an external electromagnetic field, corresponding to the diagram:



The induced vacuum current was extracted, its zeroth component being the induced charge,  $\delta\rho$ . The electrostatic potential,  $\delta\phi$ , associated with the induced charge was determined from

$$-\nabla^2(\delta\phi) = \delta\rho.$$

This potential was determined for both a point charge approximation,  $\delta\phi_{pt}$ , and a finite uniform spherical charge distribution,  $\delta\phi_f$ . Outside the nucleus, the finite nuclear size has little effect on the potential; hence  $\delta\phi_f \simeq \delta\phi_{pt}$  for  $r > R$ . Therefore the only correction made for finite nuclear size was in the region  $r < R$ . The energy correction  $W$  for  $1s$  levels, corrected for finite nuclear size, is given by:

$$W = -e \int_0^\infty \psi^\dagger \delta\phi_f \psi \, d\tau,$$

or

$$\begin{aligned} W &\simeq -e \left[ \int_0^R \psi^\dagger \delta\phi_f \psi \, d\tau + \int_R^\infty \psi^\dagger \delta\phi_{pt} \psi \, d\tau \right] \\ &= -e \left[ \int_0^R \psi^\dagger \delta\phi_f \psi \, d\tau + \int_0^\infty \psi^\dagger \delta\phi_{pt} \psi \, d\tau - \int_0^R \psi^\dagger \delta\phi_{pt} \psi \, d\tau \right] \end{aligned}$$

But

$$-e \int_0^{\infty} \psi^\dagger \delta\phi_{pt} \psi d\tau = W_{pt}$$

so

$$W \simeq W_{pt} + \left[ \left( -e \int_0^R \psi^\dagger \delta\phi_f \psi d\tau \right) - \left( -e \int_0^R \psi^\dagger \delta\phi_{pt} \psi d\tau \right) \right]$$

or

$$W = W_{pt} + \text{correction terms.}$$

The correction terms and  $W_{pt}$  were evaluated using the appropriate forms of  $\delta\phi_f$  and  $\delta\phi_{pt}$  given by Mickelwait and Corben. The vacuum polarization corrections for the 2p levels were evaluated using  $\delta\phi_{pt}$ , and no attempt was made to correct for finite nuclear size. These calculations were made for the 1s and 2p levels of all the target elements, and the resulting corrections to the theoretical  $K_\alpha$  pionic and muonic transition energies are listed in Tables VIII and IX(a) under  $E_{vp}$ .

### C. Coulomb Corrections

Coulomb corrections to the theoretical pionic  $K_\alpha$  transition energies were calculated according to the method of Pustovalov<sup>12</sup> in the nonrelativistic approximation. The nucleus is assumed to be a uniform spherical charge distribution of radius  $R$ , such that

$$\rho(r) = \frac{3eZ}{4\pi R^3} \quad \text{for} \quad 0 \leq r \leq R,$$

and

$$\rho(r) = 0 \quad \text{for} \quad R < r \leq \infty.$$

This choice of charge distribution leads to the following potentials inside and outside of the nuclear volume:

$$\phi(r)_{\text{int}} = \frac{eZ}{R} \left[ \frac{3}{2} - \frac{1}{2} \left( \frac{r}{R} \right)^2 \right] \quad \text{for} \quad 0 \leq r \leq R,$$

and

$$\phi(r)_{\text{ext}} = \frac{eZ}{r} \quad \text{for} \quad R \leq r \leq \infty.$$

The Schrodinger equation, including  $\phi(r)$ , was solved numerically by Pustovalov in the regions inside and outside of the nuclear volume. The energy eigenvalues were then found by requiring continuity of the logarithmic derivatives of the interior and exterior solutions at the edge of the nucleus. This was done for a number of values of  $R$ ,  $Z$ , and  $\mu$ , defined in terms of the parameter  $t$ :

$$t = \frac{RZ}{a},$$

with

$$a = \frac{\hbar^2}{\mu e^2}.$$

Values of  $t$  in the range 0 to 2.75 served to define the dependence of the Coulomb shift on  $\mu$ ,  $R$ , and  $Z$  for pionic and muonic atoms for  $Z \lesssim 70$ . The results of these calculations were used to develop an interpolation formula giving the Coulomb correction as a function of  $t$ :

$$\Delta n = \sum_{i=0}^5 A_i t^i + (C_0 + C_2 t^2) \exp\left(-\sum_{k=1}^4 B_k t^k\right).$$

where the A's, B's, and C's are constants calculated by Pustovalov for the 1s, 2s, 3s, 2p, and 3p levels and  $\Delta n$  is defined by

$$E_C = E_0 \left[ 1 - \frac{1}{(n + \Delta n)^2} \right],$$

where  $E_0$  is the Bohr mesic 1s level energy,  $n$  the principal quantum number, and  $E_C$  is the Coulomb correction. The Coulomb corrections for

the pionic 1s levels were calculated with nuclear radii (equivalent uniform charge distribution) determined from electron scattering experiments and with the appropriate values of  $\mu$  and  $Z$ . The Coulomb shifts for the 2p levels were negligible, and the total Coulomb corrections to the theoretical pionic  $K_{\alpha}$  X-ray energies were attributed to shifts in only the 1s levels. Relativistic corrections to the Coulomb shifts were also computed according to Pustovalov; however, they were negligible for the elements considered here. In each case, the error on the Coulomb shift was determined by allowing the nuclear radius to vary within its error so as to find extremum values of the shift. The Coulomb corrections and associated errors computed in this manner, as well as the radii used in the computations are listed in Table VIII under  $E_C$  and  $R_E$ , respectively. Where several references are listed for a given radius, a simple average value was used and the error increased so that the average radius and those listed in the references were in agreement within the error.

The Coulomb shift for the 1s levels of muonic atoms formed in the target elements was taken to be the difference between the theoretically predicted muonic  $K_{\alpha}$  energies corrected for vacuum polarization, and the experimental energies measured for the same transitions. The muonic Coulomb shifts thus measured are listed in Table IX(a) under  $E_C$ . With Coulomb shifts of the 2p levels assumed negligible, and with these values of  $E_C$ , the interpolation formula of Pustovalov was solved, using a computer search technique, for the nuclear radii for all of the target elements. These radii are listed under  $R_{\mu}$  in Table IX(a) and are compared to radii determined from electron scattering data in Table X.

Errors on the values of  $R_\mu$  were determined by allowing the measured muonic Coulomb shifts to vary within their errors. The agreement between the radii determined from muonic X-ray data and those determined from electron scattering experiments is satisfactory within the errors quoted.

As a consistency check on the pionic 1s Coulomb shifts calculated using electron scattering radii, the values of  $R_\mu$  were also used with the interpolation formula to compute the pionic 1s Coulomb shifts. These shifts are listed under  $E_C'$  in Table IX(b). The errors quoted were calculated by allowing the  $R_\mu$  to vary within their errors. Agreement between the pionic 1s Coulomb shifts calculated by both methods is good; however, the shifts calculated with the radii from electron scattering data are more precise because of the smaller errors on these radii.

#### D. Nuclear Force Shift

The experimental nuclear force shifts for the 1s levels of pionic atoms formed in each of the target elements are listed under  $E_{\text{nuc}}$  (measured) in Table VIII.  $E_{\text{tot}}$  is equal to  $E_{\text{KG}}$  (the pionic  $K_\alpha$  X-ray energy computed from the Klein-Gordon equation) corrected for both vacuum polarization,  $E_{\text{VP}}$ , and the Coulomb effect,  $E_C$ :

$$E_{\text{tot}} = E_{\text{KG}} + E_{\text{VP}} - E_C.$$

$E_{\text{nuc}}$  (measured) is then the difference between  $E_{\text{tot}}$  and  $E_{\text{exp}}$  and is assumed to be due entirely to shifts in the pionic 1s levels.  $E_{\text{nuc}}$  (measured) constitutes a shift upward in the 1s levels, implying less binding, and hence corresponds to a repulsive potential. As a final consistency check, the nuclear force shift determined using the pionic Coulomb shift,  $E_C'$ ,

calculated with radii  $R_\mu$  computed from the muonic X-ray data is listed under  $E'_{\text{nuc}}$  (measured) in Table IX(b). The large errors on  $E'_{\text{nuc}}$  (measured) arise from the poorer precision on the  $R_\mu$ . There is good agreement, within the quoted errors, between  $E'_{\text{nuc}}$  (measured) and  $E_{\text{nuc}}$  (measured); however, only the more precise  $E_{\text{nuc}}$  (measured) will be compared to the results of the theoretical calculations. Theoretical values for the pionic 1s nuclear force shift have been calculated according to the method of M. Ericson<sup>31</sup>. The pion-nucleus interaction potential,

$$V(R) = - \frac{4\pi\hbar^2}{2m_\pi} \left( 1 + \frac{m_\pi}{M} \right) \left[ b_0 \text{ eff} + b_1 \text{ eff} \left( \frac{N - Z}{A} \right) \right] \rho(R)$$

discussed in section II, was used in these calculations. The nuclear density was taken to be

$$\rho(R) = \frac{3A}{4\pi R^3},$$

where the values of  $R$  used are listed in Table VIII under  $R_e$ . The effective values of the scattering lengths used in the calculations were<sup>30</sup>

$$b_0 \text{ eff} = -0.028 \pm 0.006$$

and

$$b_1 \text{ eff} = -0.10 \pm 0.01.$$

M. Ericson solves the Schrodinger equation including the nuclear potential  $V(r)$  and the uniform spherical charge distribution potential,  $\phi(r)_{\text{int}}$ , for the region within the nuclear volume. For the region outside of the nuclear volume, the Schrodinger equation for the Coulomb potential  $\phi(r)_{\text{ext}}$  is solved. An expression for the energy eigenvalues is obtained by requiring continuity of the logarithmic derivatives of

the interior and exterior solutions at the nuclear surface. The expression for the energy is complicated and is given as a first-order expansion in the level correction,  $\Delta E$ . For the 1s state, this expression is:

$$\Delta E = \frac{E_0 (2k_0 R_e)^2 \left[ -\frac{2m_\pi V R_e}{3k_0 \hbar^2} - \frac{3}{15} \right]}{1 + 2k_0 R_e + \frac{2m_\pi V R_e^2}{3\hbar^2}}$$

where

$$E_0 = -\frac{1}{2} m_\pi (Z\alpha c)^2,$$

and

$$k_0 = \left[ \frac{2m_\pi}{\hbar^2} (-E_0) \right]^{\frac{1}{2}}.$$

The level correction,  $\Delta E$ , includes contributions from both the Coulomb and the nuclear force shifts. In order to determine only the nuclear force shift,  $V$  in the expansion for  $\Delta E$  was equated to zero, and the resulting expression solved for only the Coulomb shift. The Coulomb shift was then subtracted from the total shift  $\Delta E$ , leaving only the nuclear force shift. These theoretically-calculated values of the nuclear force shift are listed under  $E_{\text{nuc}}$  (theoretical) in Table VIII and are in fair agreement with the experimentally-determined values of the shifts reported here. Additional calculations for the 1s level shift in atoms with  $A \leq 27$  are listed and compared with the latest experimental values in Table XII. The errors quoted for the theoretical values result from uncertainties in the nuclear radii and in the effective values of the scattering lengths used in the calculations. There

is an additional 10 percent error due to the terms not included in the expansion itself. Several important factors enter in this calculation:

1. Although the calculation is termed theoretical,  $b_0$  and  $b_1$  are indirectly determined from experimental pion-nucleon scattering data. In spite of the small errors quoted on  $b_0$  and  $b_1$ , there seem to be large variations in these parameters as illustrated by the earlier values<sup>48</sup> (1963) of:

$$b_0 = -0.002 \pm 0.003$$

$$b_1 = -0.086 \pm 0.002$$

compared to the values<sup>34</sup> (1965) of

$$b_0 = -0.012 \pm 0.004$$

$$b_1 = -0.097 \pm 0.007$$

used in these calculations. The parameter  $b_{0\text{eff}}$  is the dominant term in the interaction potential, and the calculated shifts are quite sensitive to variations in its value.

2. The corrections to  $b_0$  due to nuclear effects are large. These corrections are (see section II):

Fermi motion: +0.004,

finite range correlation: -0.014,

real part of the absorption amplitude:  $-0.006 \pm 30$  percent,

giving a total correction of -0.016 which is larger than  $b_0$  itself. Thus, these corrections are essential to the theory and the results are strongly dependent on their magnitudes. Calculations using  $b_0$  and  $b_1$  un-corrected for nuclear effects give shifts that are about 50 percent smaller than corresponding experimental shifts. It

should be noted that the correction due to the real part of the absorption amplitude, which is 21 percent of  $b_0 \text{ eff}$ , is not well-known and constitutes a large source of uncertainty.

3. The shift calculations are not as dependent on the nuclear radii as the width calculations,<sup>24</sup> in which the radius enters through  $\rho^2(r)$ . A 10 percent decrease in the  $\text{Be}^9$  radius leads to only a 0.5 percent decrease in the value of the computed nuclear force shift.

Although the theoretical and experimental values of the nuclear force shift for  $A \leq 12$  agree within their errors, the theoretical values are consistently larger. This trend may be due to an overestimate of the correction to  $b_0$  from the real part of the absorption amplitude. If this correction is taken to be one-half<sup>25</sup> of that estimated by the Ericsons, the theoretically-calculated shifts become smaller and agreement between theory and experiment is improved. Results of such calculations, with  $b_0 \text{ eff} = -0.025$  are listed in Table XI under  $E_{\text{nuc}}(4)$ .

An additional calculation of the nuclear force shift using first-order perturbation theory is listed in Table XI under  $E_{\text{nuc}}(3)$ . This calculation was done with hydrogenic wave functions, the strong interaction potential,  $V(r)$ , given by the Ericsons, and a constant nuclear density  $A / (4/3\pi R_e^3)$ :

$$E_{\text{nuc}} = \int_{\text{nuc vol}} \psi^\dagger V \psi \, d\tau.$$

The pionic  $K_\alpha$  transition energies listed in Table VIII show a definite isotope shift of  $0.12 \pm 0.08$  keV for lithium and  $0.79 \pm 0.16$  keV

for boron. However, within the experimental errors, the muonic  $K_{\alpha}$  transition energies for the same elements exhibit no such shift. This effect, then, is attributed to the strong pion-nucleus interaction. The experimental nuclear force shift ( $E_{\text{nuc}}$  (W&M), Table XI) exhibits deviations due to isotope effects, which for lithium are about 60 percent and for boron about 30 percent of the respective  $\text{Li}^6$  and  $\text{B}^{10}$  nuclear force shifts. With the isotopic-spin dependent term included in  $V(r)$ , calculations according to the method of M. Ericson ( $E_{\text{nuc}}$  (1), Table XI) accurately predict the percentage shifts due to isotope effects. However, when the isotopic-spin dependent term is not included in  $V(r)$ , the isotope shifts predicted for lithium and boron are only 17 percent and 9 percent of the respective  $\text{Li}^6$  and  $\text{B}^{10}$  nuclear force shifts. Results of these calculations are listed under  $E_{\text{nuc}}$  (2) in Table XI.

On the basis of the above calculations and the experimental measurements reported in this paper, the following conclusions are made:

1. The theory of the Ericsons gives results that are in fair agreement with the experimental nuclear force shift for light pionic atoms. Agreement between theory and experiment is enhanced if the contribution to  $b_{0\text{eff}}$  from the real part of the absorption amplitude is taken to be about half that suggested by the Ericsons. For atoms with  $Z \gtrsim 7$  the theoretical shift becomes larger than the measured shift and agreement is poorer. This disagreement may be due either to the failure of the additivity hypothesis inherent in the Ericsons potential that the  $\pi$ -nucleus scattering lengths are the coherent sum of the  $\pi$ -nucleon scattering lengths, or to an overestimate in nuclear corrections to  $b_0$  for  $Z \gtrsim 7$ . Since the measured

widths seem to be smaller than those predicted by the Ericsons' theory<sup>24</sup> (Table XIII) for  $Z \geq 7$ , the correction to  $b_0$  from the real part of the absorption amplitude may be very small for these elements. Such an effect would tend to improve agreement between the theoretical and measured shifts.

2. Contrary to the results of Seki and Cromer<sup>49</sup>, first order perturbation theory calculations give results that are in rough agreement with the experimental nuclear force shifts reported here. Seki and Cromer, and others<sup>50</sup>, have done a calculation for the nuclear force shift similar to that of M. Ericson but with new approximation techniques for the wave function outside the region of strong interaction. Their conclusions were based on a calculation in which earlier measured pionic  $K_\alpha$  transition energies<sup>5</sup> were used to predict the properties of the wave functions and the strong interaction potential.

3. The isotopic-spin dependent term in the strong interaction potential developed by the Ericsons is necessary in order to provide agreement between calculated and experimentally measured percentage isotope shifts. Seki and Cromer observe no isotopic dependence in the strong interaction potential.

4. The additivity hypothesis for the  $\pi$ -nucleon scattering lengths can neither be confirmed nor disproved here, since the present value of the correction to  $b_0$  from the real part of the absorption amplitude is not well known.

## VI. TABLES

### TABLE

- I. Pionic and muonic  $K_{\alpha}$  X-ray energies for  $\text{Li}^6$ .
- II. Pionic and muonic  $K_{\alpha}$  X-ray energies for  $\text{Li}^7$ .
- III. Pionic and muonic  $K_{\alpha}$  X-ray energies for  $\text{Be}^9$ .
- IV. Pionic and muonic  $K_{\alpha}$  X-ray energies for  $\text{B}^{10}$ .
- V. Pionic and muonic  $K_{\alpha}$  X-ray energies for  $\text{B}^{11}$ .
- VI. Pionic and muonic  $K_{\alpha}$  X-ray energies for  $\text{C}^{12}$ .
- VII. Summary of recent pionic and muonic  $K_{\alpha}$  X-ray energy measurements for elements in the range  $Z = 3$  to  $Z = 6$ .
- VIII. Measured and calculated pionic  $K_{\alpha}$  X-ray energies and level shifts.
- IX. (a) Measured and calculated muonic  $K_{\alpha}$  X-ray energies, level shifts, and nuclear radii.  
(b) Pionic  $1s$  level nuclear force shift determined with radii computed from muonic X-ray data.
- X. Comparison of nuclear radii determined from muonic X-ray data and those determined from electron scattering.
- XI. Comparison of several theoretical calculations of the pionic  $1s$  nuclear force shift.
- XII. Comparison of theoretical pionic  $1s$  nuclear force shift and recent experimental shifts.
- XIII. Comparison of theoretical pionic  $K_{\alpha}$  line width calculations and recent experimental width measurements.

Table I - Pionic and muonic  $K_{\alpha}$  X-ray energies for  $\text{Li}^6$ .

See Table VII for final errors on weighted averages.

| RUN       | X-RAY ENERGY, keV |                  |
|-----------|-------------------|------------------|
|           | $\pi K_{\alpha}$  | $\mu K_{\alpha}$ |
| A18       | $24.13 \pm 0.11$  | $18.63 \pm 0.13$ |
| A25       | $24.19 \pm 0.04$  | $18.66 \pm 0.11$ |
| A28       | $24.18 \pm 0.04$  | $18.62 \pm 0.11$ |
| A30       | $24.20 \pm 0.04$  | $18.66 \pm 0.11$ |
| A35       | $24.16 \pm 0.04$  | $18.68 \pm 0.12$ |
| A38       | -----             | $18.67 \pm 0.04$ |
| WTD. AVG. | $24.18 \pm 0.03$  | $18.66 \pm 0.04$ |

Table II - Pionic and muonic  $K_{\alpha}$  X-ray energies for  $\text{Li}^7$ .

See Table VII for final errors on weighted averages.

| RUN       | X-RAY ENERGY, keV |                  |
|-----------|-------------------|------------------|
|           | $\pi K_{\alpha}$  | $\mu K_{\alpha}$ |
| A17       | $24.05 \pm 0.04$  | $18.71 \pm 0.10$ |
| A23       | $24.04 \pm 0.05$  | -----            |
| A27       | $24.11 \pm 0.05$  | $18.77 \pm 0.10$ |
| A29       | $24.05 \pm 0.04$  | $18.64 \pm 0.10$ |
| A37       | -----             | $18.72 \pm 0.04$ |
| WTD. AVG. | $24.06 \pm 0.03$  | $18.71 \pm 0.03$ |

Table III - Pionic and muonic  $K_{\alpha}$  X-ray energies for  $\text{Be}^9$ .

See Table VII for final errors on weighted averages.

| RUN       | X-RAY ENERGY, keV |                  |
|-----------|-------------------|------------------|
|           | $\pi K_{\alpha}$  | $\mu K_{\alpha}$ |
| A20       | $42.32 \pm 0.04$  | $33.39 \pm 0.03$ |
| A21       | $42.31 \pm 0.05$  | $33.39 \pm 0.04$ |
| A22       | $42.33 \pm 0.07$  | $33.40 \pm 0.05$ |
| A26       | $42.32 \pm 0.05$  | $33.39 \pm 0.04$ |
| A31       | $42.30 \pm 0.04$  | $33.39 \pm 0.02$ |
| A36       | -----             | $33.40 \pm 0.03$ |
| WTD. AVG. | $42.32 \pm 0.02$  | $33.39 \pm 0.01$ |

Table IV - Pionic and muonic  $K_{\alpha}$  X-ray energies for  $\text{B}^{10}$ .

See Table VII for final errors on weighted averages.

| RUN       | X-RAY ENERGY, keV |                  |
|-----------|-------------------|------------------|
|           | $\pi K_{\alpha}$  | $\mu K_{\alpha}$ |
| G5        | $65.77 \pm 0.09$  | $52.19 \pm 0.09$ |
| G12       | $65.80 \pm 0.07$  | $52.17 \pm 0.06$ |
| G13       | $65.77 \pm 0.07$  | $52.12 \pm 0.08$ |
| G20       | -----             | $52.21 \pm 0.06$ |
| G22       | $65.74 \pm 0.07$  | $52.18 \pm 0.06$ |
| G23       | $65.87 \pm 0.09$  | $52.24 \pm 0.09$ |
| WTD. AVG. | $65.79 \pm 0.04$  | $52.18 \pm 0.03$ |

Table V - Pionic and muonic  $K_{\alpha}$  X-ray energies for  $B^{11}$ .

See Table VII for final errors on weighted averages.

| RUN       | X-RAY ENERGY, keV |                  |
|-----------|-------------------|------------------|
|           | $\pi K_{\alpha}$  | $\mu K_{\alpha}$ |
| G4        | 65.03 $\pm$ 0.10  | 52.28 $\pm$ 0.08 |
| G11       | 64.99 $\pm$ 0.08  | 52.23 $\pm$ 0.06 |
| G14       | 64.97 $\pm$ 0.09  | 52.18 $\pm$ 0.06 |
| G21       | -----             | 52.25 $\pm$ 0.06 |
| WTD. AVG. | 65.00 $\pm$ 0.05  | 52.23 $\pm$ 0.03 |

Table VI - Pionic and muonic  $K_{\alpha}$  X-ray energies for  $C^{12}$ .

See Table VII for final errors on weighted averages.

| RUN       | X-RAY ENERGY, keV |                  |
|-----------|-------------------|------------------|
|           | $\pi K_{\alpha}$  | $\mu K_{\alpha}$ |
| G3        | 93.23 $\pm$ 0.19  | 75.22 $\pm$ 0.04 |
| G10       | 93.11 $\pm$ 0.16  | 75.21 $\pm$ 0.03 |
| G19       | -----             | 75.22 $\pm$ 0.03 |
| K6        | 93.07 $\pm$ 0.15  | 75.17 $\pm$ 0.03 |
| K7        | 93.28 $\pm$ 0.17  | 75.27 $\pm$ 0.05 |
| K8        | 93.25 $\pm$ 0.15  | 75.27 $\pm$ 0.03 |
| K9        | -----             | 75.23 $\pm$ 0.03 |
| K10       | 93.21 $\pm$ 0.16  | 75.27 $\pm$ 0.04 |
| WTD. AVG. | 93.19 $\pm$ 0.06  | 75.23 $\pm$ 0.02 |

Table VII - Summary of recent pionic  $K_{\alpha}$  X-ray energy measurements.

| ELEMENT                                 | E (W&M)      | E (CERN)     | E (BERK)   |
|---|--------------|--------------|------------|
| PIONIC $K_{\alpha}$ X-RAY ENERGIES, keV |              |              |            |
| Li <sup>6</sup>                         | 24.18 ± 0.06 | -----        | 23.9 ± 0.2 |
| Li <sup>7</sup>                         | 24.06 ± 0.06 | -----        | 23.8 ± 0.2 |
| Be <sup>9</sup>                         | 42.32 ± 0.05 | 42.38 ± 0.20 | 42.1 ± 0.2 |
| B <sup>10</sup>                         | 65.79 ± 0.11 | 65.94 ± 0.18 | 64.9 ± 0.2 |
| B <sup>11</sup>                         | 65.00 ± 0.11 | 64.98 ± 0.18 | 64.5 ± 0.2 |
| C <sup>12</sup>                         | 93.19 ± 0.12 | 92.94 ± 0.15 | 93.3 ± 0.5 |
| MUONIC $K_{\alpha}$ X-RAY ENERGIES, keV |              |              |            |
| Li <sup>6</sup>                         | 18.66 ± 0.07 | -----        | 18.1 ± 0.4 |
| Li <sup>7</sup>                         | 18.71 ± 0.06 | -----        | 18.1 ± 0.4 |
| Be <sup>9</sup>                         | 33.39 ± 0.05 | -----        | 33.0 ± 0.2 |
| B <sup>10</sup>                         | 52.18 ± 0.10 | 52.23 ± 0.15 | 51.6 ± 0.3 |
| B <sup>11</sup>                         | 52.23 ± 0.09 | 52.31 ± 0.15 | 51.6 ± 0.3 |
| C <sup>12</sup>                         | 75.23 ± 0.08 | 75.25 ± 0.15 | 75.8 ± 0.5 |

Table VIII - Measured and calculated pionic  $K_{\alpha}$  X-ray energies and level shifts.

(All energies in keV)

| ELEMENT         | $E_{exp}$    | $E_{KG}$ | $E_{VP}$ | $R_e$ , fm               | $E_C$       | $E_{tot}$    | $E_{nuc}$<br>(measured) | $E_{nuc}$<br>(theoretical) |
|-----------------|--------------|----------|----------|--------------------------|-------------|--------------|-------------------------|----------------------------|
| Li <sup>6</sup> | 24.13 ± 0.06 | 24.49    | 0.10     | 3.20 ± 0.06 <sup>a</sup> | 0.06        | 24.53        | 0.35 ± 0.06             | 0.47 ± 0.09                |
| Li <sup>7</sup> | 24.06 ± 0.06 | 24.58    | 0.10     | 3.09 ± 0.04 <sup>a</sup> | 0.05        | 24.63        | 0.57 ± 0.06             | 0.79 ± 0.10                |
| Be <sup>9</sup> | 42.32 ± 0.05 | 43.93    | 0.21     | 3.25 ± 0.50 <sup>b</sup> | 0.19 ± 0.06 | 43.95 ± 0.06 | 1.63 ± 0.08             | 2.12 ± 0.29                |
| B <sup>10</sup> | 65.79 ± 0.11 | 68.80    | 0.37     | 3.16 ± 0.15 <sup>c</sup> | 0.42 ± 0.04 | 68.75 ± 0.04 | 2.96 ± 0.12             | 3.29 ± 0.63                |
| B <sup>11</sup> | 65.00 ± 0.11 | 68.89    | 0.37     | 3.12 ± 0.15 <sup>c</sup> | 0.41 ± 0.04 | 68.85 ± 0.04 | 3.85 ± 0.12             | 4.56 ± 0.63                |
| C <sup>12</sup> | 93.19 ± 0.12 | 99.41    | 0.58     | 3.11 ± 0.05 <sup>d</sup> | 0.84 ± 0.03 | 99.15 ± 0.03 | 5.96 ± 0.12             | 6.50 ± 1.22                |

<sup>a</sup>See reference 51.<sup>b</sup>See references 52, 53, and 54.<sup>c</sup>See reference 55.<sup>d</sup>See references 56 and 57.

Table IX(a) - Measured and calculated muonic  $K_{\alpha}$  X-ray  
energies, shifts, and radii.

(Energy in keV)

| ELEMENT         | $E_{\text{exp}}$ | $E_{\text{D}}$ | $E_{\text{VP}}$ | $E_{\text{tot}}$ | $E_{\text{C}}$ | $R_{\mu}$ , fm |
|-----------------|------------------|----------------|-----------------|------------------|----------------|----------------|
| Li <sup>6</sup> | 18.66 ± 0.07     | 18.64          | 0.06            | 18.70            | 0.04 ± 0.07    | 4.0 ± 6.0      |
| Li <sup>7</sup> | 18.71 ± 0.06     | 18.69          | 0.06            | 18.75            | 0.04 ± 0.06    | 4.0 ± 5.0      |
| Be <sup>9</sup> | 33.39 ± 0.05     | 33.35          | 0.13            | 33.48            | 0.09 ± 0.05    | 3.38 ± 1.16    |
| B <sup>10</sup> | 52.18 ± 0.10     | 52.18          | 0.24            | 52.42            | 0.24 ± 0.10    | 3.56 ± 0.88    |
| B <sup>11</sup> | 52.23 ± 0.09     | 52.23          | 0.24            | 52.47            | 0.24 ± 0.09    | 3.56 ± 0.78    |
| C <sup>12</sup> | 75.23 ± 0.08     | 75.29          | 0.38            | 75.67            | 0.44 ± 0.08    | 3.36 ± 0.35    |

Table IX(b) - Pionic 1s nuclear force shift (keV)

determined with  $R_{\mu}$  from muon data.

| ELEMENT         | $E_{\text{C}}^{\prime}$ | $E_{\text{nuc}}^{\prime}$<br>(measured) |
|-----------------|-------------------------|---|
| Li <sup>6</sup> | 0.09 ± 0.11             | 0.32 ± 0.11                             |
| Li <sup>7</sup> | 0.09 ± 0.13             | 0.53 ± 0.13                             |
| Be <sup>9</sup> | 0.20 ± 0.11             | 1.62 ± 0.12                             |
| B <sup>10</sup> | 0.53 ± 0.22             | 2.85 ± 0.25                             |
| B <sup>11</sup> | 0.53 ± 0.20             | 3.73 ± 0.23                             |
| C <sup>12</sup> | 0.97 ± 0.17             | 5.83 ± 0.21                             |

Table X - Comparison of nuclear radii (equivalent uniform charge distribution) determined from muonic X-ray data and those determined from electron scattering.

| ELEMENT         | RADIUS, fm  |                     |
|-----------------|-------------|---------------------|
|                 | THIS WORK   | ELECTRON SCATTERING |
| Li <sup>6</sup> | 4.0 ± 6.0   | 3.28 ± 0.06         |
| Li <sup>7</sup> | 4.0 ± 5.0   | 3.09 ± 0.04         |
| Be <sup>9</sup> | 3.38 ± 1.16 | 3.25 ± 0.50         |
| B <sup>10</sup> | 3.56 ± 0.88 | 3.16 ± 0.15         |
| B <sup>11</sup> | 3.56 ± 0.78 | 3.12 ± 0.15         |
| C <sup>12</sup> | 3.36 ± 0.34 | 3.11 ± 0.05         |

Table XI - Comparison of theoretical calculations of the  
1s level nuclear force shift (keV).

| ELEMENT         | $E_{\text{nuc}}$ (W&M) | $E_{\text{nuc}}$ (1) | $E_{\text{nuc}}$ (2) | $E_{\text{nuc}}$ (3) | $E_{\text{nuc}}$ (4) |
|-----------------|------------------------|----------------------|----------------------|----------------------|----------------------|
| Li <sup>6</sup> | 0.35 ± 0.06            | 0.47                 | 0.47                 | 0.51                 | 0.42                 |
| Li <sup>7</sup> | 0.57 ± 0.06            | 0.79                 | 0.55                 | 0.90                 | 0.74                 |
| Be <sup>9</sup> | 1.63 ± 0.08            | 2.21                 | 1.58                 | 2.47                 | 1.97                 |
| B <sup>10</sup> | 2.96 ± 0.12            | 3.29                 | 3.29                 | 3.75                 | 2.95                 |
| B <sup>11</sup> | 3.85 ± 0.12            | 4.56                 | 3.58                 | 5.47                 | 4.23                 |
| C <sup>12</sup> | 5.96 ± 0.12            | 6.50                 | 6.50                 | 7.61                 | 5.84                 |

$E_{\text{nuc}}$  (W&M): Experimental nuclear force shift.

$E_{\text{nuc}}$  (1) : Theoretical nuclear force shift after M. Ericson.

$$b_{0\text{eff}} = -0.028 \pm 0.006$$

$$b_{1\text{eff}} = -0.10 \pm 0.01.$$

$E_{\text{nuc}}$  (2) : Same as  $E_{\text{nuc}}$  (1), but no isotopic spin dependence in  $V(r)$ .

$E_{\text{nuc}}$  (3) : Theoretical nuclear force shift from perturbation theory.

$$b_{0\text{eff}} \text{ and } b_{1\text{eff}} \text{ same as in } E_{\text{nuc}} (1).$$

$E_{\text{nuc}}$  (4) : Same as  $E_{\text{nuc}}$  (1), but

$$b_{0\text{eff}} = -0.025 \pm 0.006$$

$$b_{1\text{eff}} = -0.10 \pm 0.01.$$

Table XII - Comparison of theoretical nuclear force shift and recent experimental shift measurements.

(Energy in keV)

| ELEMENT          | RADIUS   | $E_{\text{nuc}}$ (W&M)      | $E_{\text{nuc}}$ (CERN) | $E_{\text{nuc}}$ (BERK) | $E_{\text{nuc}}$ (THEORET) |
|------------------|----------|-----------------------------|-------------------------|-------------------------|----------------------------|
| He <sup>4</sup>  | 2.07(60) | 0.07 ± 0.06 <sup>(58)</sup> | -----                   | -----                   | 0.10                       |
| Li <sup>6</sup>  | 3.28     | 0.35 ± 0.06                 | -----                   | 0.6 ± 0.2               | 0.47 ± 0.09                |
| Li <sup>7</sup>  | 3.09     | 0.57 ± 0.06                 | -----                   | 0.8 ± 0.2               | 0.79 ± 0.10                |
| Be <sup>9</sup>  | 3.25     | 1.63 ± 0.08                 | 1.57 ± 0.20             | 1.75 ± 0.2              | 2.12 ± 0.29                |
| B <sup>10</sup>  | 3.16     | 2.96 ± 0.12                 | 2.79 ± 0.19             | 2.6 ± 0.6               | 3.29 ± 0.63                |
| B <sup>11</sup>  | 3.12     | 3.85 ± 0.12                 | 3.80 ± 0.19             | 2.9 ± 0.7               | 4.56 ± 0.63                |
| C <sup>12</sup>  | 3.11     | 5.96 ± 0.12                 | 6.12 ± 0.15             | 5.8 ± 0.5               | 6.50 ± 1.22                |
| N <sup>14</sup>  | 3.16(54) | -----                       | 10.10 ± 0.16            | 9.8 ± 1.1               | 11.49 ± 2.12               |
| O <sup>16</sup>  | 3.42(56) | -----                       | 15.73 ± 0.26            | 14.2 ± 1.2              | 18.68 ± 3.44               |
| O <sup>18</sup>  | 3.58(59) | -----                       | 20.59 ± 0.26            | -----                   | 27.17 ± 3.41               |
| F <sup>19</sup>  | 3.68(8)  | -----                       | 25.6 ± 0.6              | 25.8 ± 1.1              | 34.50 ± 5.18               |
| Na <sup>23</sup> | 3.79(8)  | -----                       | 52.4 ± 1.0              | 49.8 ± 1.4              | 68.36 ± 10.42              |
| Mg <sup>24</sup> | 3.88(8)  | -----                       | -----                   | 57.3 ± 1.4              | 79.32 ± 14.32              |
| Al <sup>27</sup> | 3.91(8)  | -----                       | -----                   | -----                   | 120.20 ± 18.53             |

Table XII - Comparison of theoretical nuclear force shift and recent experimental shift measurements.

(Energy in keV)

| ELEMENT          | RADIUS   | $E_{\text{nuc}}$ (W&M) | $E_{\text{nuc}}$ (CERN) | $E_{\text{nuc}}$ (BERK) | $E_{\text{nuc}}$ (THEORET) |
|------------------|----------|------------------------|-------------------------|-------------------------|----------------------------|
| He <sup>4</sup>  | 2.07(60) | $0.07 \pm 0.06$ (58)   | -----                   | -----                   | 0.10                       |
| Li <sup>6</sup>  | 3.28     | $0.35 \pm 0.06$        | -----                   | $0.6 \pm 0.2$           | $0.47 \pm 0.09$            |
| Li <sup>7</sup>  | 3.09     | $0.57 \pm 0.06$        | -----                   | $0.8 \pm 0.2$           | $0.79 \pm 0.10$            |
| Be <sup>9</sup>  | 3.25     | $1.63 \pm 0.08$        | $1.57 \pm 0.20$         | $1.75 \pm 0.2$          | $2.12 \pm 0.29$            |
| B <sup>10</sup>  | 3.16     | $2.96 \pm 0.12$        | $2.79 \pm 0.19$         | $2.6 \pm 0.6$           | $3.29 \pm 0.63$            |
| B <sup>11</sup>  | 3.12     | $3.85 \pm 0.12$        | $3.80 \pm 0.19$         | $2.9 \pm 0.7$           | $4.56 \pm 0.63$            |
| C <sup>12</sup>  | 3.11     | $5.96 \pm 0.12$        | $6.12 \pm 0.15$         | $5.8 \pm 0.5$           | $6.50 \pm 1.22$            |
| N <sup>14</sup>  | 3.16(54) | -----                  | $10.10 \pm 0.16$        | $9.8 \pm 1.1$           | $11.49 \pm 2.12$           |
| O <sup>16</sup>  | 3.42(56) | -----                  | $15.73 \pm 0.26$        | $14.2 \pm 1.2$          | $18.68 \pm 3.44$           |
| O <sup>18</sup>  | 3.58(59) | -----                  | $20.59 \pm 0.26$        | -----                   | $27.17 \pm 3.41$           |
| F <sup>19</sup>  | 3.68(8)  | -----                  | $25.6 \pm 0.6$          | $25.8 \pm 1.1$          | $34.50 \pm 5.18$           |
| Na <sup>23</sup> | 3.79(8)  | -----                  | $52.4 \pm 1.0$          | $49.8 \pm 1.4$          | $68.36 \pm 10.42$          |
| Mg <sup>24</sup> | 3.88(8)  | -----                  | -----                   | $57.3 \pm 1.4$          | $79.32 \pm 14.32$          |
| Al <sup>27</sup> | 3.91(8)  | -----                  | -----                   | -----                   | $120.20 \pm 18.53$         |

Table XIII - Comparison of theoretical width calculations  
and recent experimental width measurements.

Radii used in the calculations are listed in Table XII.

(Widths in keV)

| ELEMENT          | $\Gamma$ (W&M)      | $\Gamma$ (BERK) | $\Gamma$ (CERN) | $\Gamma$ (THEORET) |
|------------------|---------------------|-----------------|-----------------|--------------------|
| He <sup>4</sup>  | 0.00 $\pm$ 0.09(58) | -----           | -----           | 0.06               |
| Li <sup>6</sup>  | 0.15 $\pm$ 0.05     | 0.39 $\pm$ 0.36 | -----           | 0.11               |
| Li <sup>7</sup>  | 0.19 $\pm$ 0.05     | 0.57 $\pm$ 0.30 | -----           | 0.18               |
| Be <sup>9</sup>  | 0.58 $\pm$ 0.05     | 0.85 $\pm$ 0.28 | 1.07 $\pm$ 0.30 | 0.56               |
| B <sup>10</sup>  | 1.68 $\pm$ 0.12     | 1.4 $\pm$ 0.5   | 1.27 $\pm$ 0.25 | 1.48               |
| B <sup>11</sup>  | 1.72 $\pm$ 0.15     | 2.3 $\pm$ 0.5   | 1.87 $\pm$ 0.25 | 1.75               |
| C <sup>12</sup>  | 3.25 $\pm$ 0.15     | 2.6 $\pm$ 0.5   | 2.96 $\pm$ 0.25 | 3.41               |
| N <sup>14</sup>  | -----               | 4.1 $\pm$ 0.4   | 4.48 $\pm$ 0.30 | 6.72               |
| O <sup>16</sup>  | -----               | 9.0 $\pm$ 2.0   | 7.56 $\pm$ 0.50 | 9.69               |
| O <sup>18</sup>  | -----               | -----           | 8.67 $\pm$ 0.70 | 10.57              |
| F <sup>19</sup>  | -----               | 4.6 $\pm$ 2.0   | 9.40 $\pm$ 1.5  | 14.76              |
| Na <sup>23</sup> | -----               | 4.6 $\pm$ 3.0   | 10.3 $\pm$ 4.0  | 33.57              |
| Mg <sup>24</sup> | -----               | -----           | -----           | 41.80              |
| Al <sup>27</sup> | -----               | -----           | -----           | 63.73              |

## VII. ACKNOWLEDGMENTS

The author wishes to express his appreciation to the following persons:

Dr. Morton Eckhause, his advisor, for his continued guidance and encouragement during the course of the experiment and in the preparation of the manuscript.

Mr Robert J. Harris, Jr., with whom the author worked in preparation for the experiment and in the taking of the experimental data.

Drs. Robert E. Welsh and Robert T. Siegel for their assistance and advice and careful reading of the manuscript.

Drs. Rolf G. Winter and David A. Jenkins for helpful discussions and reading the manuscript.

Dr. Raymond W. Southworth for reading the manuscript and, as director of the William and Mary computer center, for his support and that of his staff rendered during computer analysis of the data.

Mr. William H. Hunt for calculations of the level corrections due to vacuum polarization effects.

Dr. John Biggerstaff for loan of the precision pulser used in the linearity tests.

Dr. David K. Anderson for helpful discussions concerning the theoretical aspects of this investigation.

Mr. George H. Miller for his help in recording and analyzing the data, Mr. W. Wade Sapp for his aid in taking the data, and Mr. Darrell G. Eisenhut for his help with the figures.

Mr. Stanley Hummel and the William and Mary machine shop staff for construction of the scintillation counters and much of the cryogenic equipment.

Dr. Roger B. Sutton and the Carnegie-Mellon Nuclear Research Center for their hospitality.

His wife Jeanne for her encouragement and for her help in the punching of the data, computer programming, and the typing of the initial drafts of the manuscript.

This work was supported in part by the National Aeronautics and Space Administration.

## VIII. LIST OF REFERENCES

1. M. Conversi, E. Pancini, and O. Piccioni, Phys. Rev. 71, 209 (1947).
2. M. Camac, A. D. McGuire, J. B. Platt, and H. J. Schulte, Phys. Rev. 88, 134 (1952).
3. D. West, Repts. Prog. Phys. 21, 271 (1958).
4. D. A. Jenkins and K. M. Crowe, Phys. Rev. Letters 16, 637 (1966).
5. D. A. Jenkins, R. Kunselman, M. K. Simmons, and T. Yamazaki, Phys. Rev. Letters 17, 1 (1966).
6. D. A. Jenkins and R. Kunselman, Phys. Rev. Letters 17, 1148 (1966).
7. G. Backenstoss, S. Charalambus, H. Daniel, G. Poolz, and H. Schmitt, International Conference on Nuclear Physics, Gatlinburg, Tennessee, September 12-17, 1966.
8. G. Backenstoss, S. Charalambus, H. Daniel, H. Koch, G. Poelz, H. Schmitt, and L. Tauscher, Phys. Letters 25B, 547 (1967).
9. G. Backenstoss, S. Charalambus, H. Daniel, H. Koch, G. Poelz, H. Schmitt, and L. Tauscher, Phys. Letters 25B, 365 (1967).
10. N. L. Cooper and E. M. Henley, Phys. Rev. 92, 801 (1953).
11. Flügge, Lectures on field theory and applications to meson problems, at Carnegie-Mellon Institute (1953, unpublished).
12. E. Pustovalov, Soviet Physics JETP 36, 1288 (1959).
13. A. B. Mickelwait and H. C. Corben, Phys. Rev. 96, 1145 (1954).
14. A. B. Mickelwait, thesis, Carnegie-Mellon Institute, (1954, unpublished).
15. M. Stearns and M. B. Sterns, Phys. Rev. 103, 1534 (1956).

16. J. D. Bjorken and S. D. Drell, Relativistic Quantum Mechanics, McGraw-Hill, N.Y. (1964).
17. B. A. Jacobsohn, Phys. Rev. 96, 1637 (1954).
18. E. Amaldi and G. Fidecaro, Phys. Rev. 81, 339 (1951).
19. J. M. Kennedy, Phys. Rev. 87, 935 (1952).
20. D. L. Hill and K. W. Ford, Phys. Rev. 94, 1617 (1954).
21. H. Primakoff, Rev. Mod. Phys. 31, 802 (1959).
22. K. A. Brueckner, Phys. Rev. 98, 769 (1955).
23. A. M. L. Messiah and R. E. Marshak, Phys. Rev. 88, 678 (1952).
24. R. J. Harris, Jr., thesis, College of William and Mary (1968).
25. D. Anderson, private communication.
26. S. Deser, M. L. Goldberger, K. Baumann, and W. Thirring, Phys. Rev. 96, 774 (1954).
27. K. A. Brueckner, R. Serber, and K. M. Watson, Phys. Rev. 84, 258 (1951).
28. R. Karplus and F. Halpern, Bull. Amer. Phys. Soc. 2, 5 (1957).
29. L. Wolfenstein, Bull. Amer. Phys. Soc. 2, 39 (1957).
30. M. Ericson and T. E. O. Ericson, Ann. Phys. 36, 323 (1966).
31. M. Ericson, Compt. rend. 257, 3831 (1963).
32. M. Ericson, Compt. rend. 258, 1471 (1964).
33. S. G. Eckstein, Phys. Rev. 129, 413 (1963)
34. V. K. Samaranyake and W. S. Woolcock, Phys. Rev. Letters 15, 936 (1965).
35. M. H. Foss, Conference on High Energy Cyclotron Improvement at the College of William and Mary, p. 85 (1964).

36. M. H. Foss, R. W. Findly, and A. Suzuki, Conference on High Energy Cyclotron Improvement at the College of William and Mary, p. 75 (1964)
37. C. H. Nowlin and J. L. Blankenship, Rev. Sci. Inst. 36, 1830 (1965).
38. M. G. Strauss, R. N. Larsen and L. L. Sifter, Nucl. Instr. and Meth. 46, 45 (1967).
39. EG&G Inc., Nanotes 1, No. 2 (Jan. 1967).
40. R. J. Harris, Jr., and W. B. Shuler, Nucl. Instr. and Meth. 51, 341 (1967).
41. R. J. Harris, Jr., William and Mary Report WM 8 (1967).
42. P. P. Day, Phys. Rev. 97, 689 (1955).
43. E. J. Seppi, H. Henrikson, F. Boehm, and J. W. M. DuMond, Nucl. Instr. and Meth. 16, 17 (1962).
44. R. L. Heath, W. W. Black, and J. E. Cline, Nucleonics 24, No. 5 (1966)
45. W. W. Black and R. L. Heath, Nucl. Phys. A90, 650 (1967).
46. W. W. Black, U. S. AEC report No. IDO-17140 (1965).
47. J. A. Bearden, Rev. Mod. Phys. 39, 78 (1967).
48. J. Hamilton and W. S. Woolcock, Rev. Mod. Phys. 35, 737 (1963).
49. R. Seki and A. H. Cromer, Phys. Rev. 156, 93 (1967).
50. L. P. Fulcher, J. M. Eisenberg, and J. Le Tourneux, Can. J. Phys. 45, 3313 (1967).
51. L. R. Suelze, M. R. Yearian, and Hall Crannell, Phys. Rev. 162, 992 (1967).
52. R. Hofstadter, Rev. Mod. Phys. 28, 214 (1956). (Private communication from J. F. Streib.)

53. R. Hofstadter, *Ann. Rev. Nucl. Sci.* 7, 231 (1957).
54. U. Meyer-Berkhout, K. W. Ford, and A. E. S. Green, *Ann. Phys.* 8, 119 (1959).
55. T. Stovall, J. Goldemberg, and D. B. Isabelle, *Nucl. Phys.* 86, 225 (1966).
56. H. Crannell, *Phys. Rev.* 148, 1107 (1966).
57. R. Engfer and D. Turck, *Z. Physik* 205, 60 (1967).
58. R. J. Wetmore, D. C. Buckle, J. R. Kane, and R. T. Siegel, *Phys. Rev. Letters* 19, 1003 (1967).
59. G. R. Bishop, *Nucl. Phys.* 41, 118 (1963).
60. L. R. B. Elton, Nuclear Sizes, Oxford University Press, London (1961).
61. J. Mandel, The Statistical Analysis of Experimental Data, Interscience (1964).

## IX. FIGURES

### FIGURE

- 1 . CMU differential range curve for pions stopping in  $2.9 \text{ gm/cm}^2 \text{ C}^{12}$ .
- 2 . SREL differential range curve for pions stopping in  $5.7 \text{ gm/cm}^2 \text{ C}^{12}$ .
- 3 . Counter geometry.
- 4 . Logic circuitry.
- 5 . Timing spectrum.
- 6 . Time to amplitude converter calibration.
- 7a. Silicon spectrometer preamplifier first stage.
- 7b. Germanium spectrometer preamplifier first stage.
- 8 .  $\text{Am}^{241}$  spectrum showing Si(Li) spectrometer resolution.
- 9 . Si(Li) spectrometer calibration spectrum.
- 10 .  $\text{Co}^{57}$  spectrum showing Ge(Li) spectrometer resolution.
- 11 . Ge(Li) spectrometer calibration spectrum.
- 12 . Exaggerated nonlinear system response.
- 13 . Si(Li) spectrometer system linearity.
- 14 . Ge(Li) spectrometer system linearity.
- 15 . Raw  $\pi$  and  $\mu$  spectra in  $\text{Li}^6$ .
- 16 . Raw  $\pi$  and  $\mu$  spectra in  $\text{Li}^7$ .
- 17 . Raw  $\pi$  and  $\mu$  spectra in  $\text{Be}^9$ .
- 18 . Raw  $\pi$  and  $\mu$  spectra in  $\text{B}^{10}$ .
- 19 . Raw  $\pi$  and  $\mu$  spectra in  $\text{B}^{11}$ .
- 20 . Raw  $\pi$  and  $\mu$  spectra in  $\text{C}^{12}$ .
- 21 . Calibration line center drift for Si(Li) spectrometer (CMU run).
- 22 . Calibration line center drift for Ge(Li) spectrometer (CMU run).
- 23 . Calibration line center drift for Ge(Li) spectrometer (SREL run).

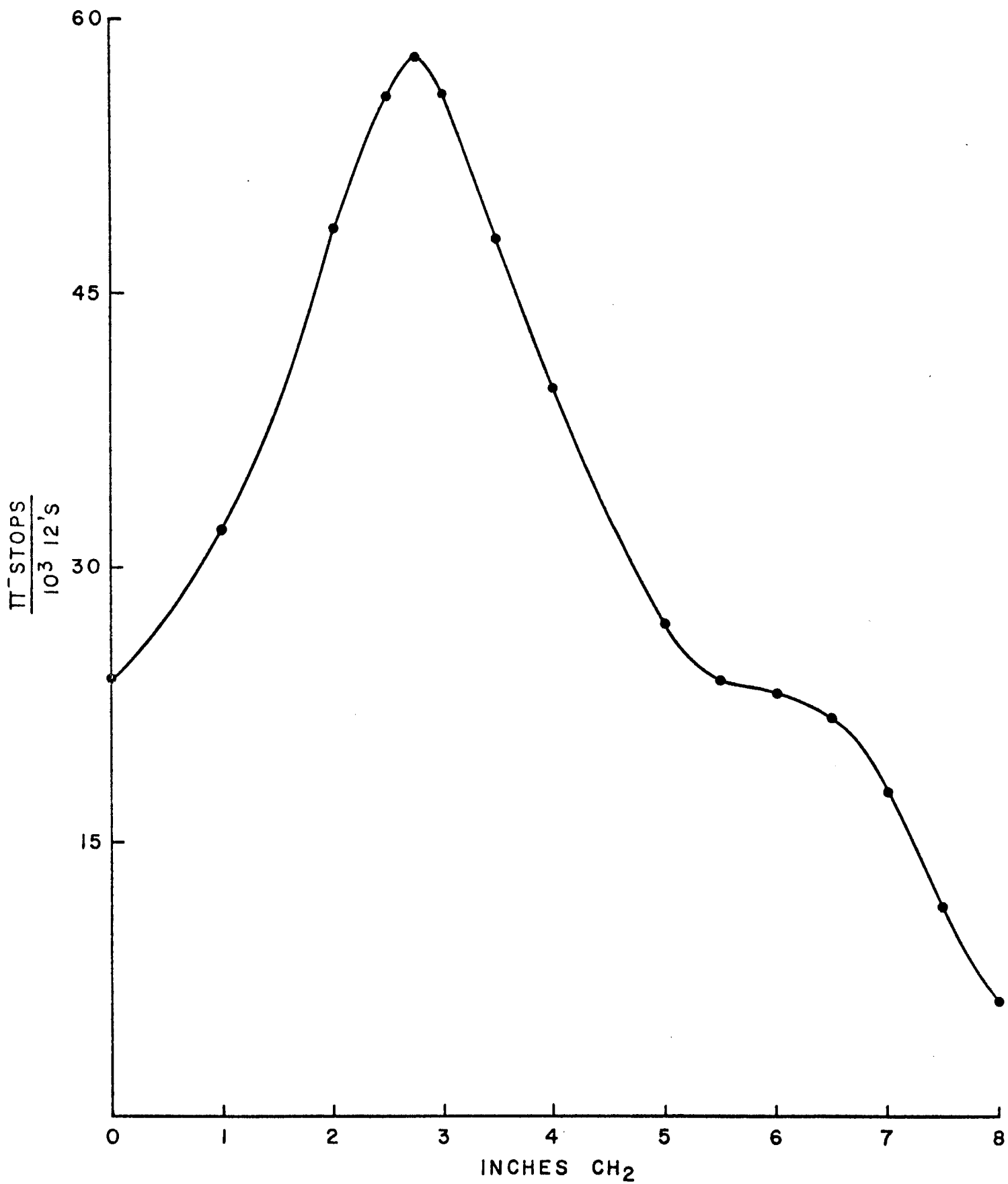


FIG. 1

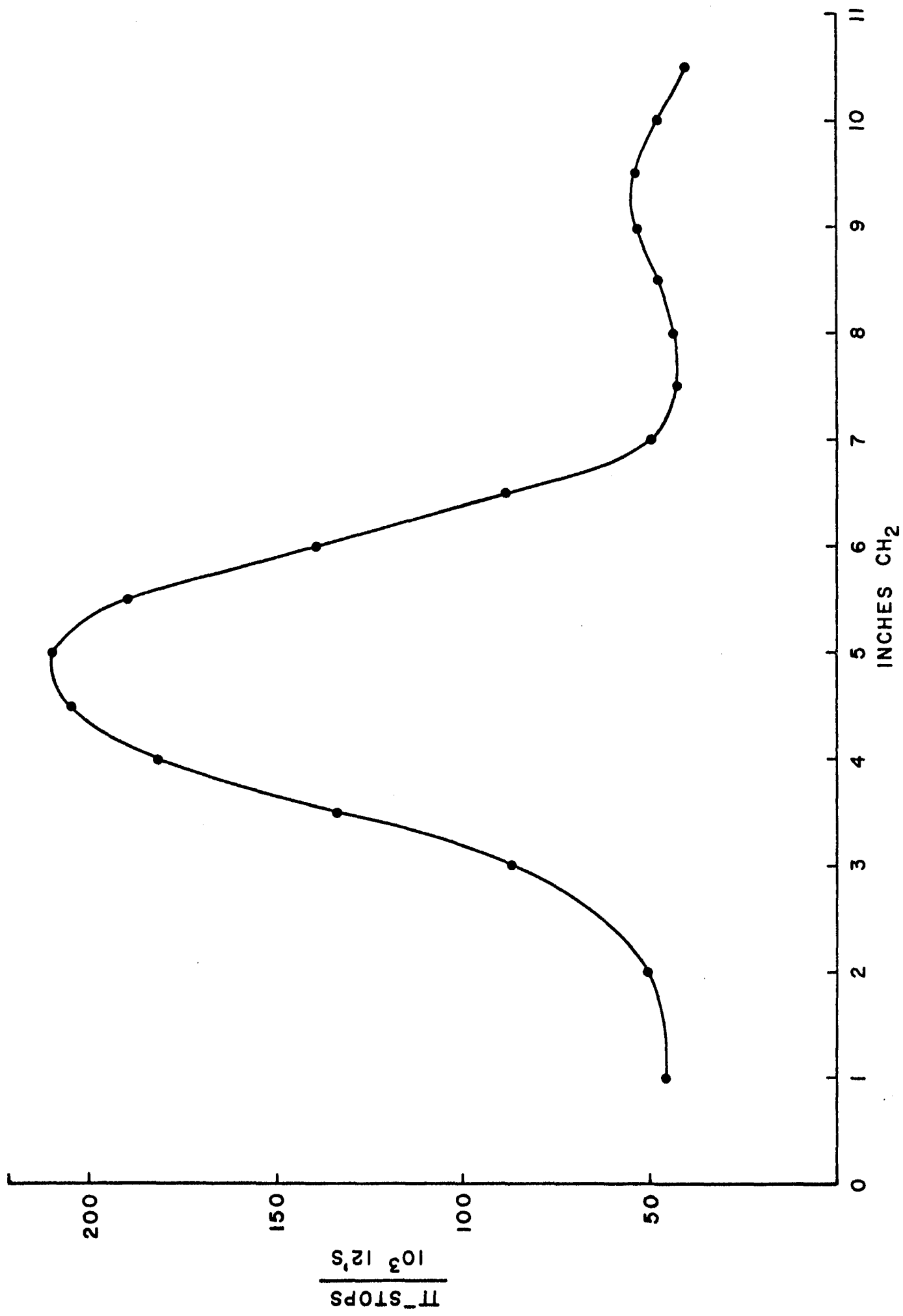


FIG. 2

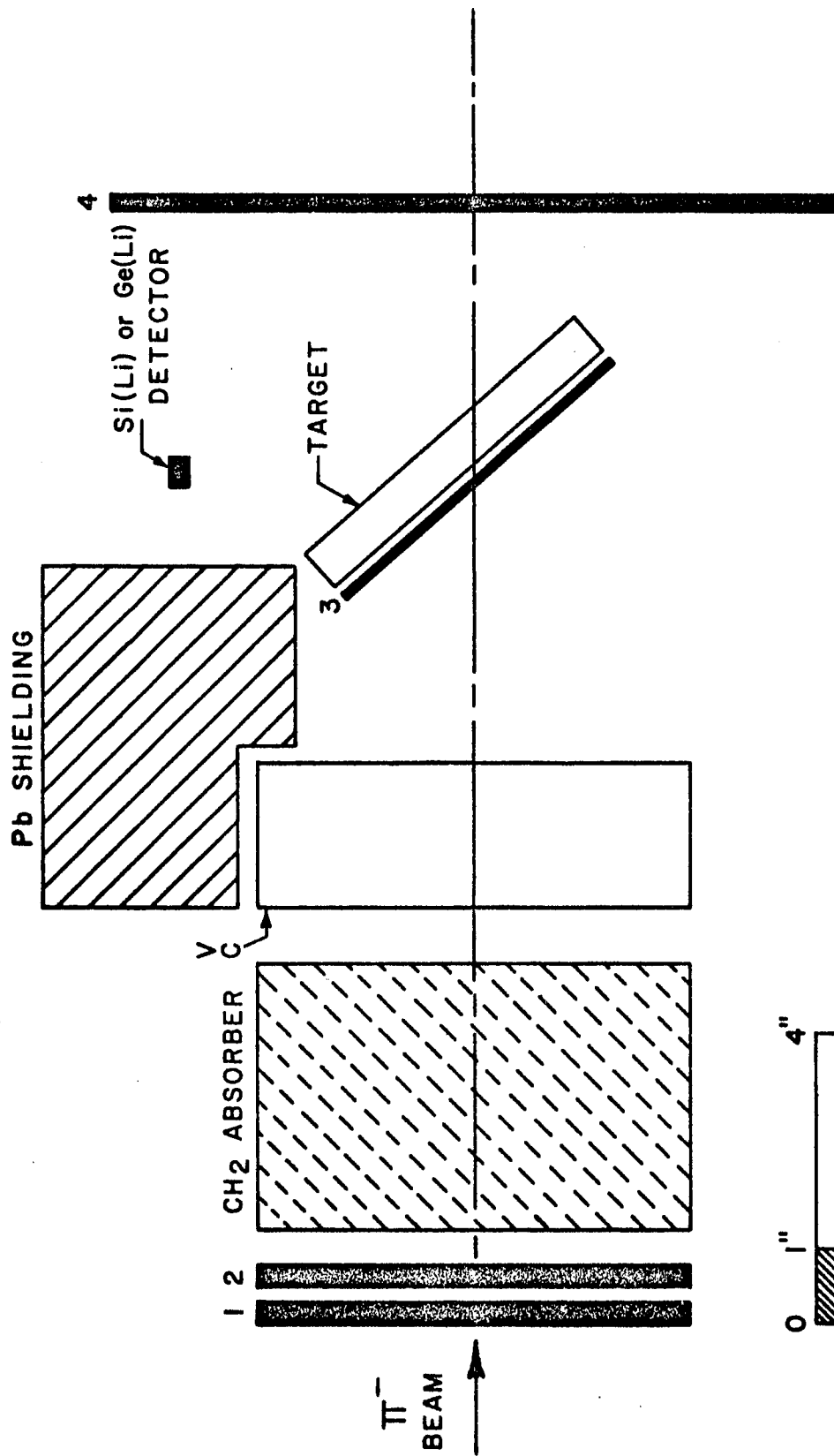


FIG. 3



# TIMING SPECTRUM

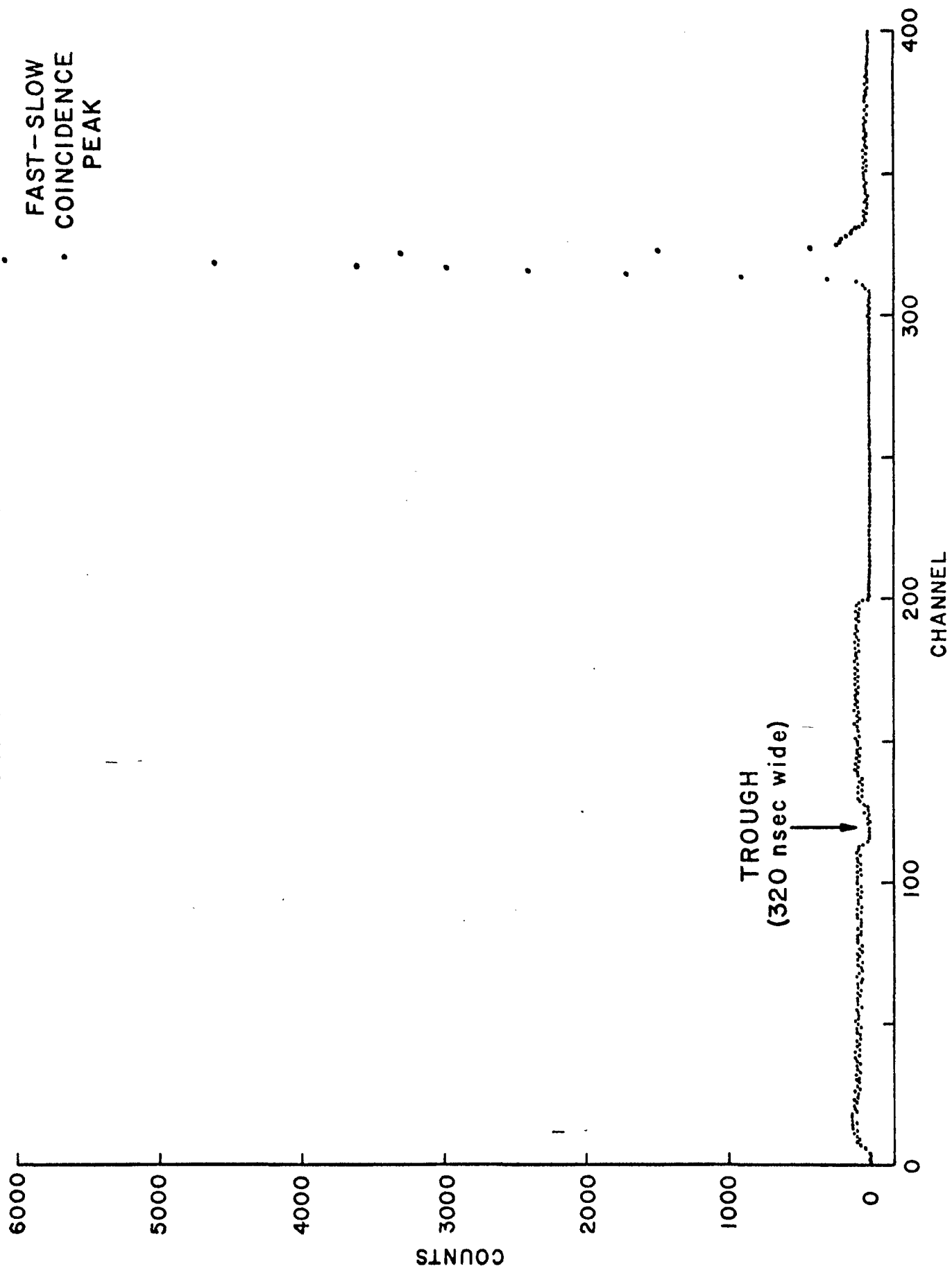


FIG. 5

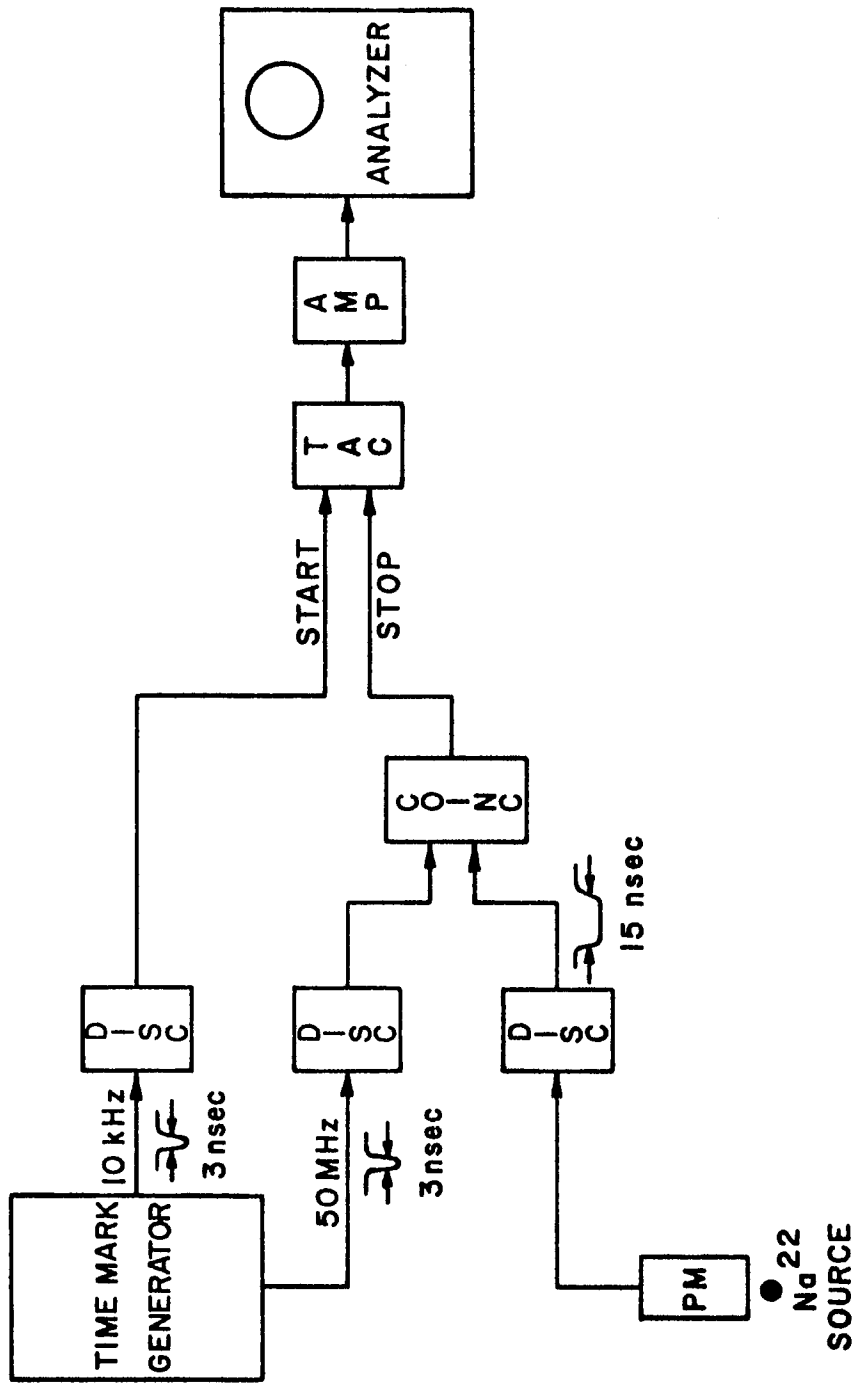
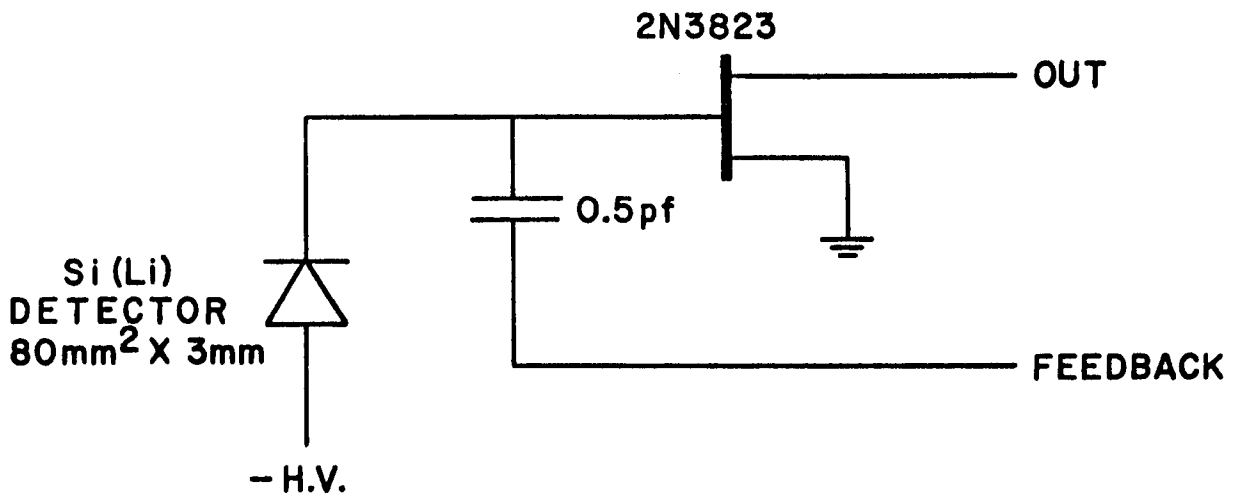
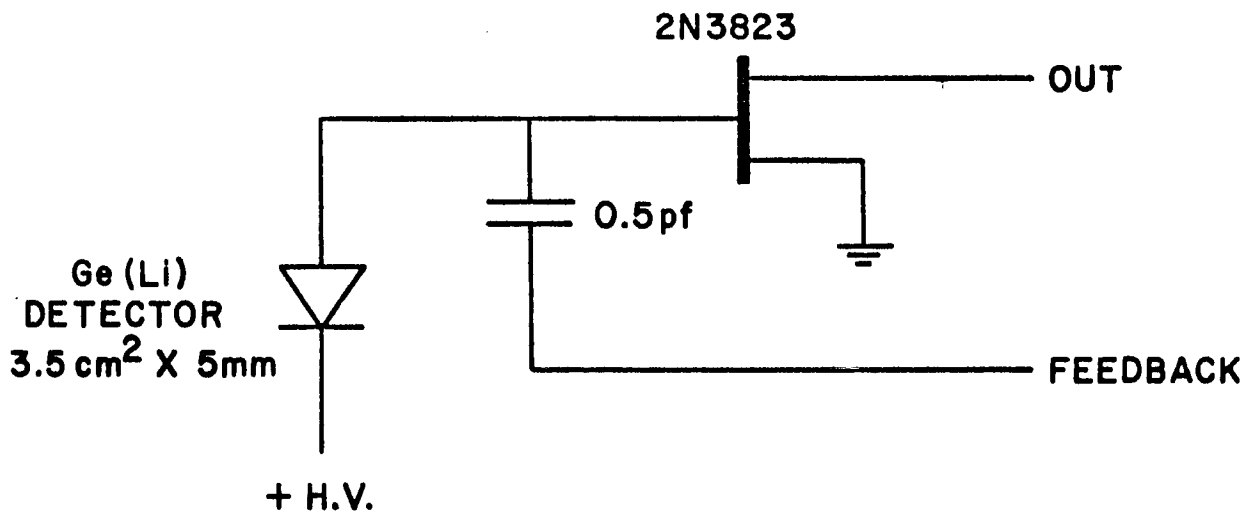


FIG. 6



SILICON SPECTROMETER — PREAMPLIFIER FIRST STAGE

FIG. 7(a)



GERMANIUM SPECTROMETER — PREAMPLIFIER FIRST STAGE

FIG. 7(b)

# Am<sup>241</sup> SPECTRUM (SILICON DETECTOR)

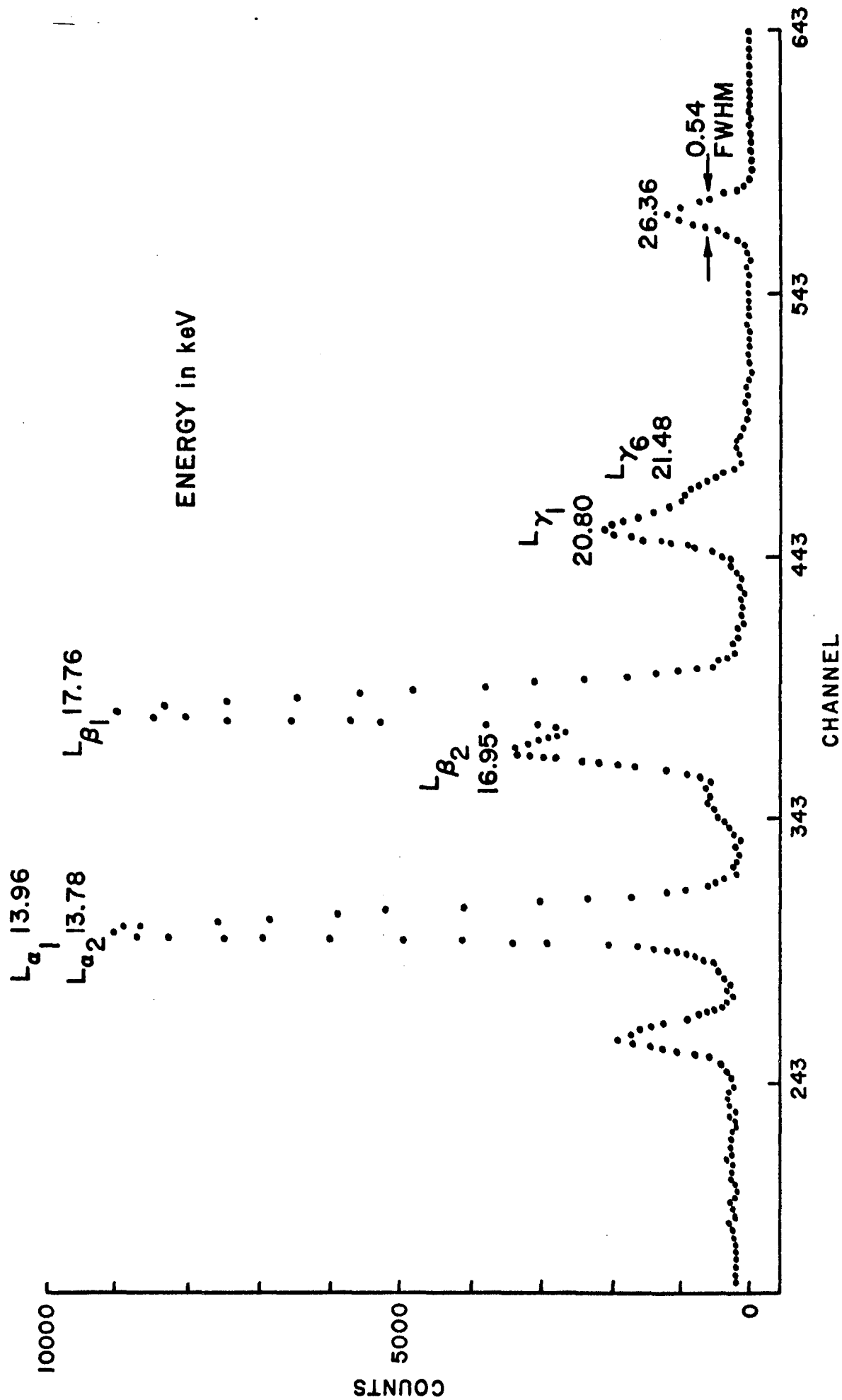


FIG. 8

# Am<sup>241</sup> CALIBRATION SPECTRUM



Energy in keV

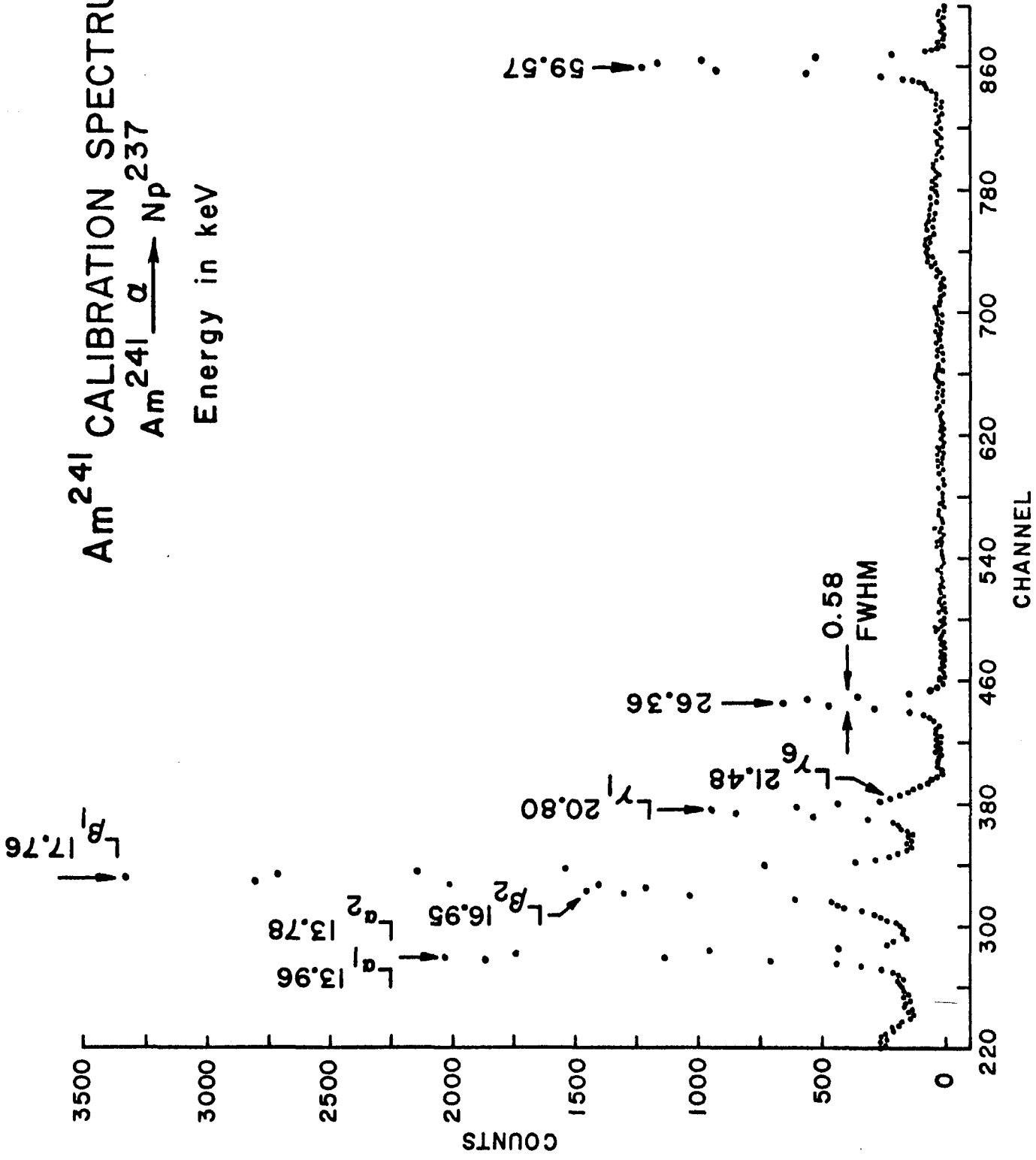


FIG. 9

# Co<sup>57</sup> SPECTRUM (GERMANIUM DETECTOR)

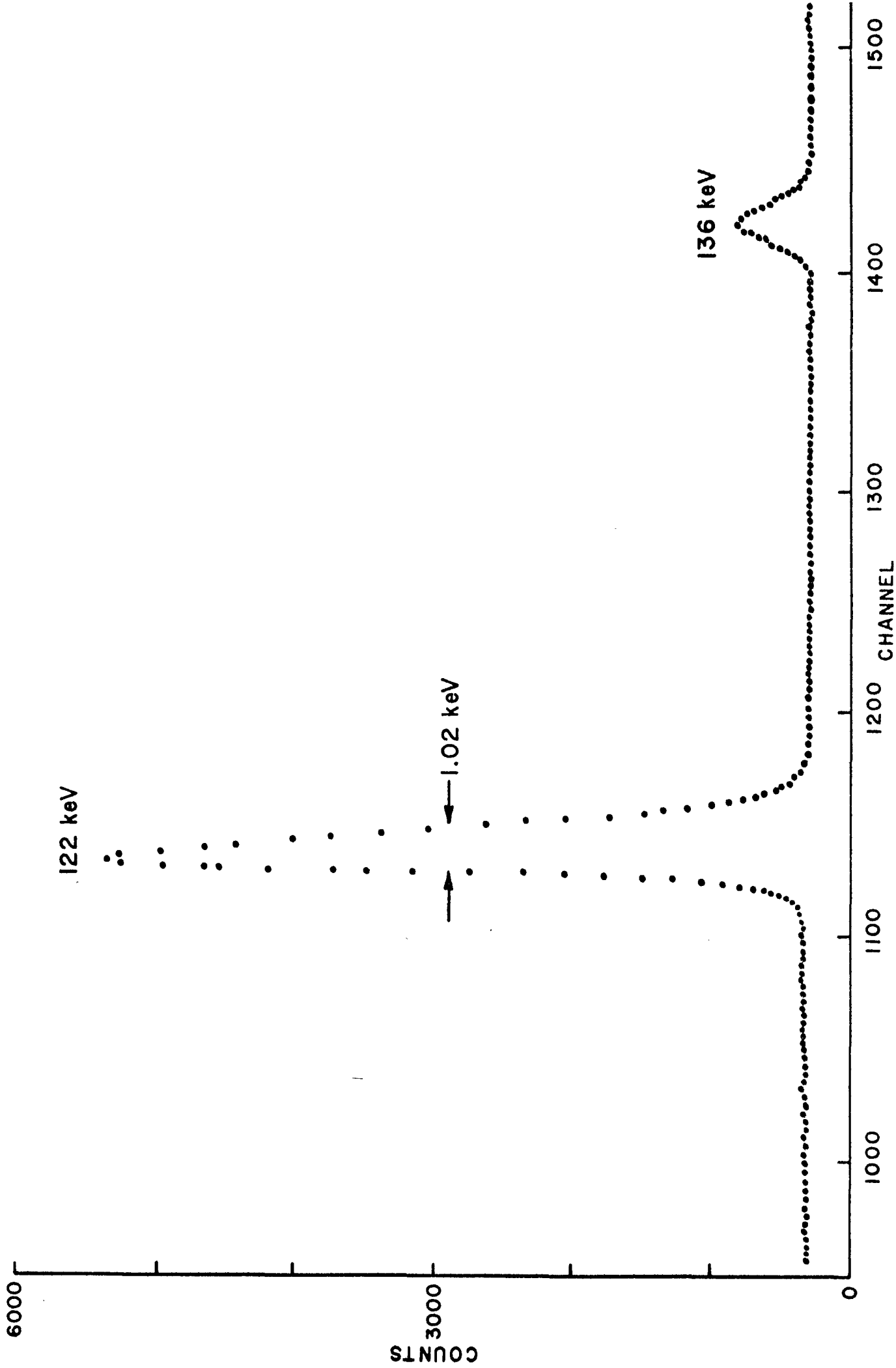


FIG. 10

# Ta<sup>182</sup>, Am<sup>241</sup> and Hg<sup>203</sup> CALIBRATION SPECTRA

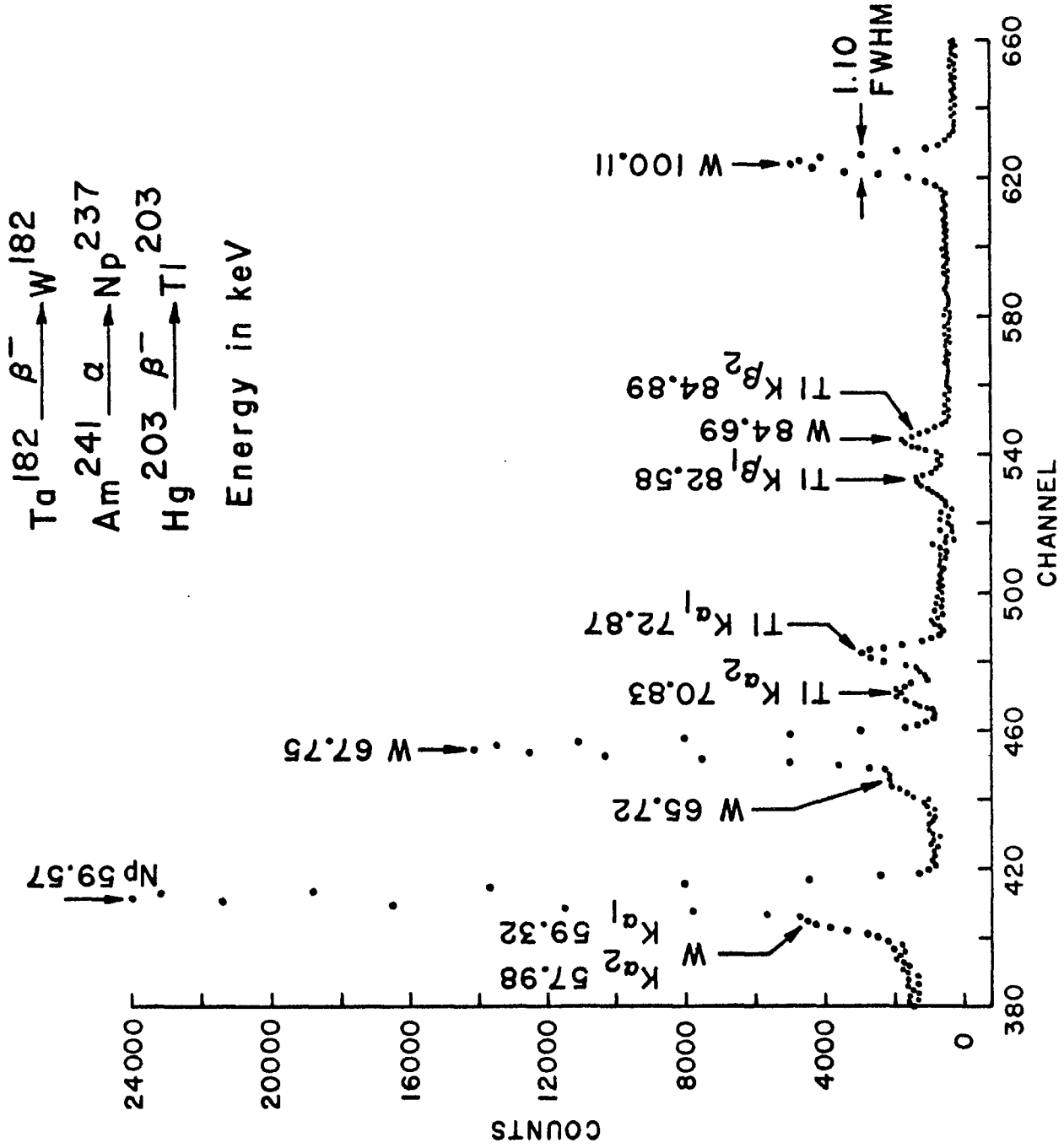


FIG. 11

ILLUSTRATION OF EXAGGERATED  
NONLINEAR SYSTEM RESPONSE

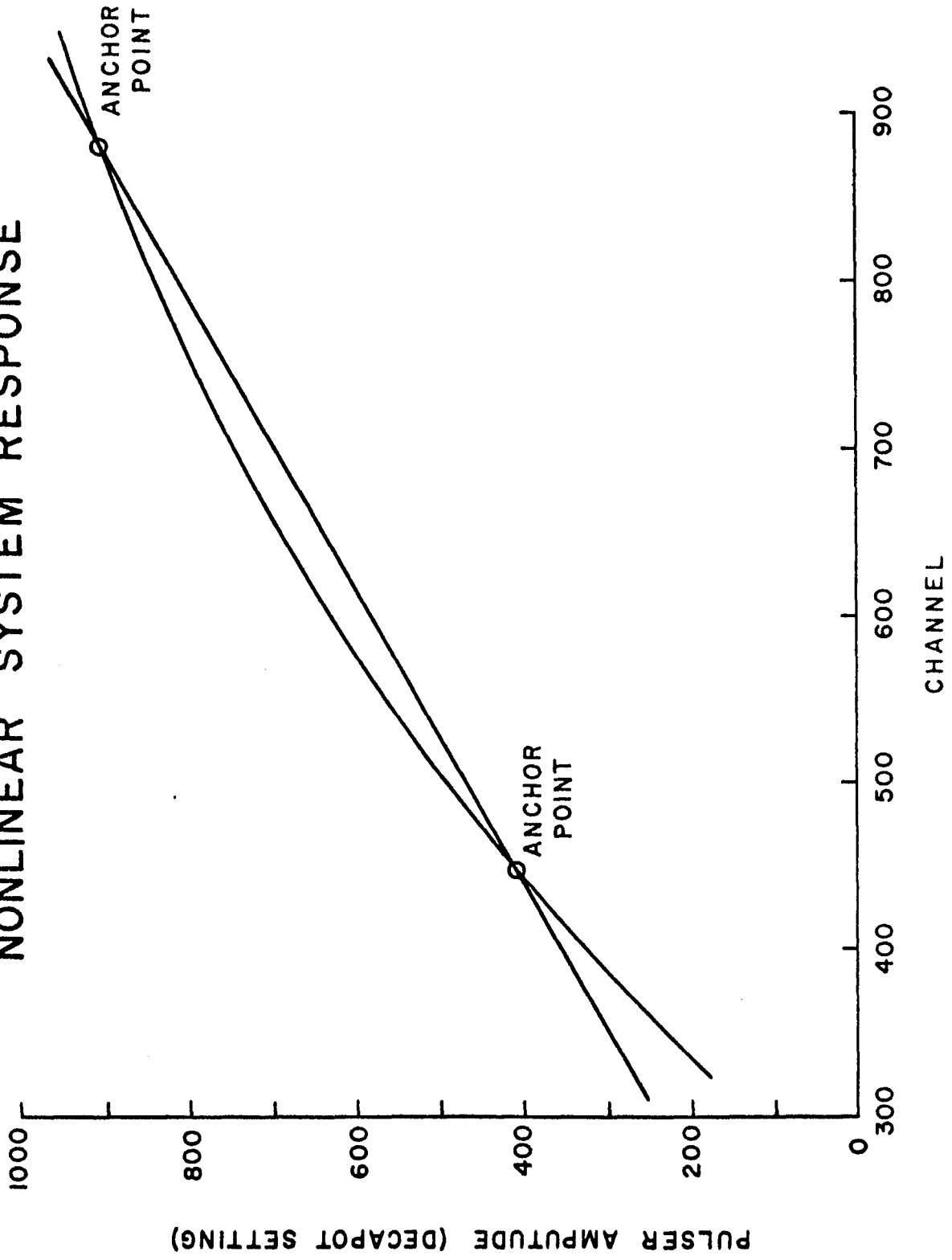


FIG. 12

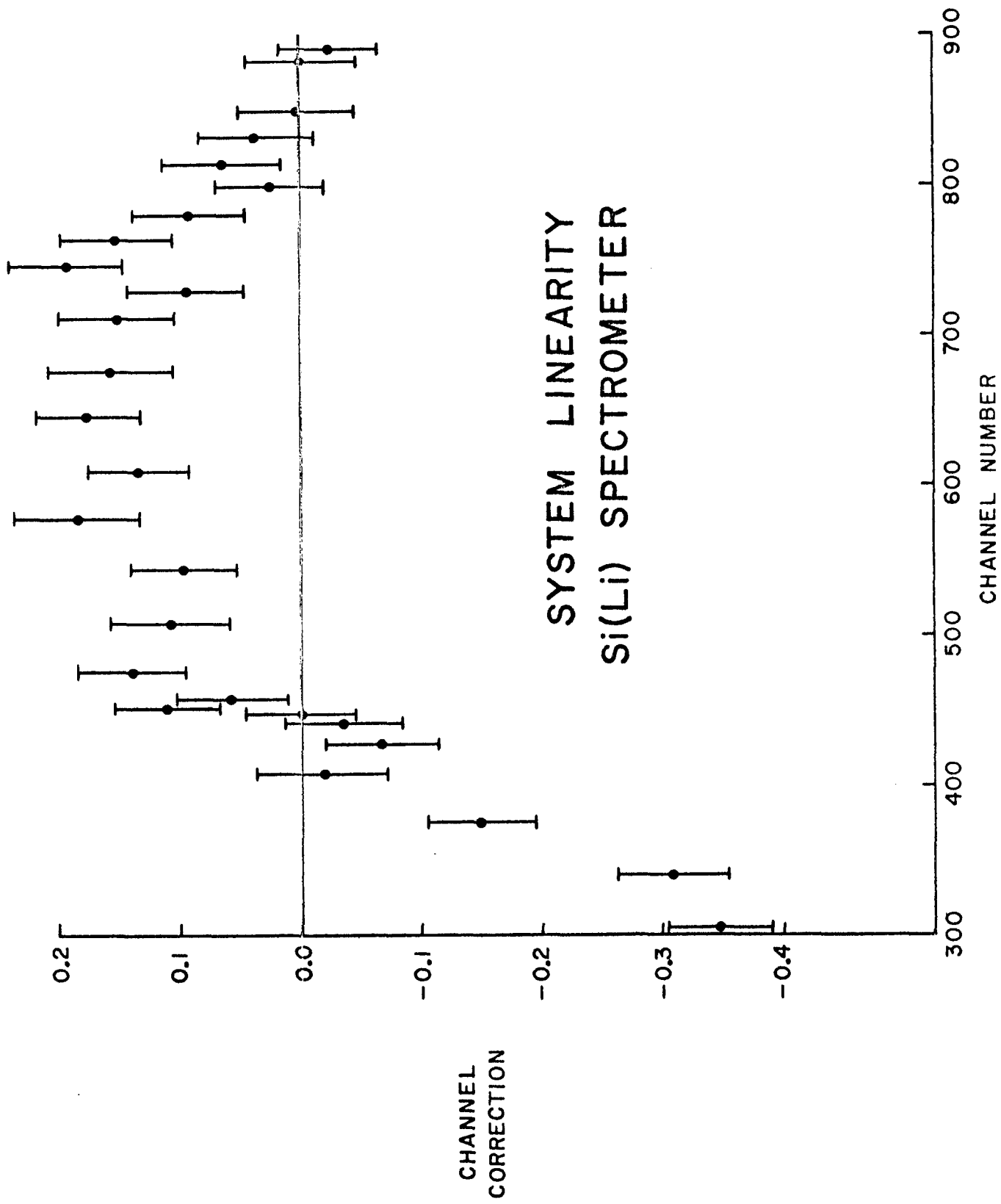


FIG. 13

SYSTEM LINEARITY  
Ge(Li) SPECTROMETER

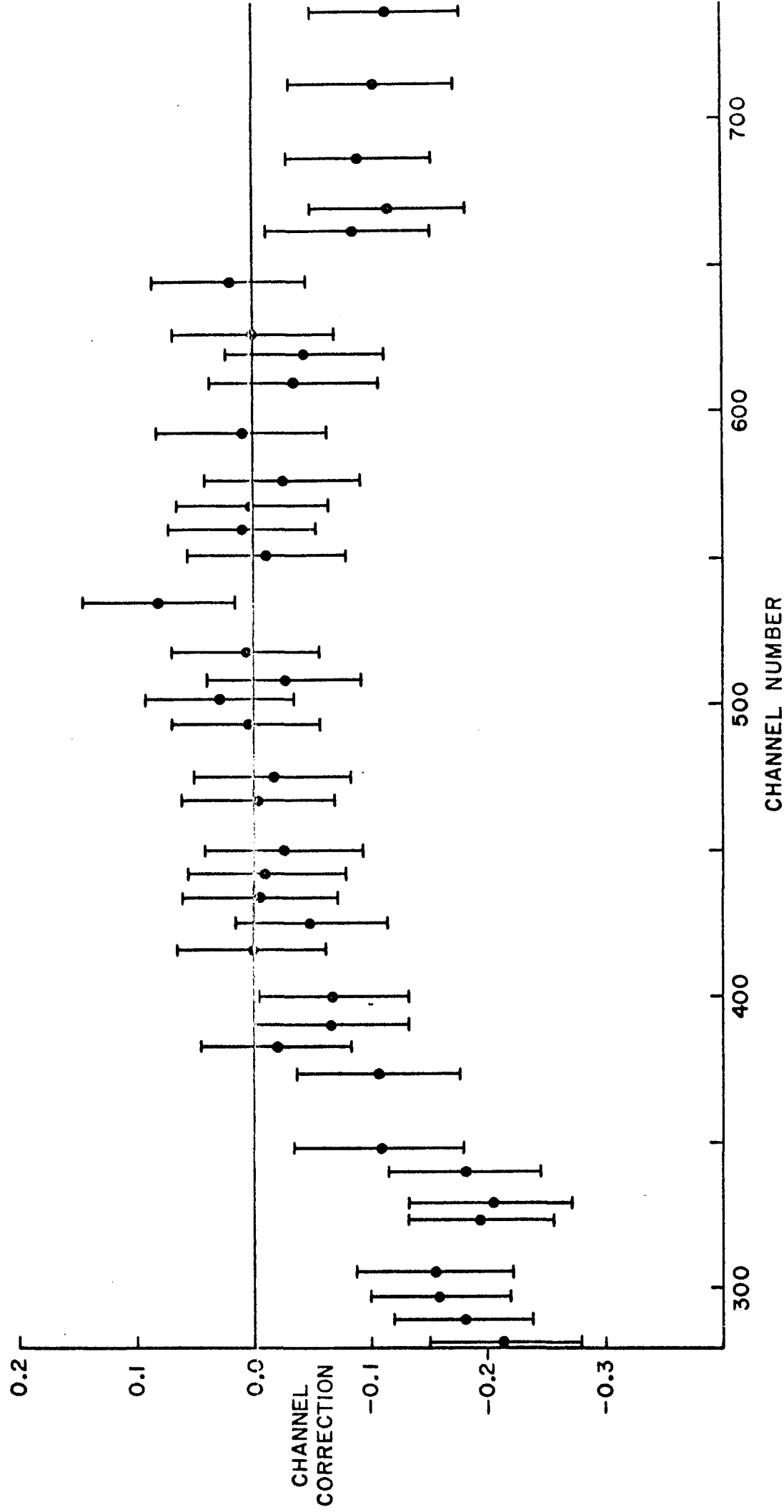


FIG. 14

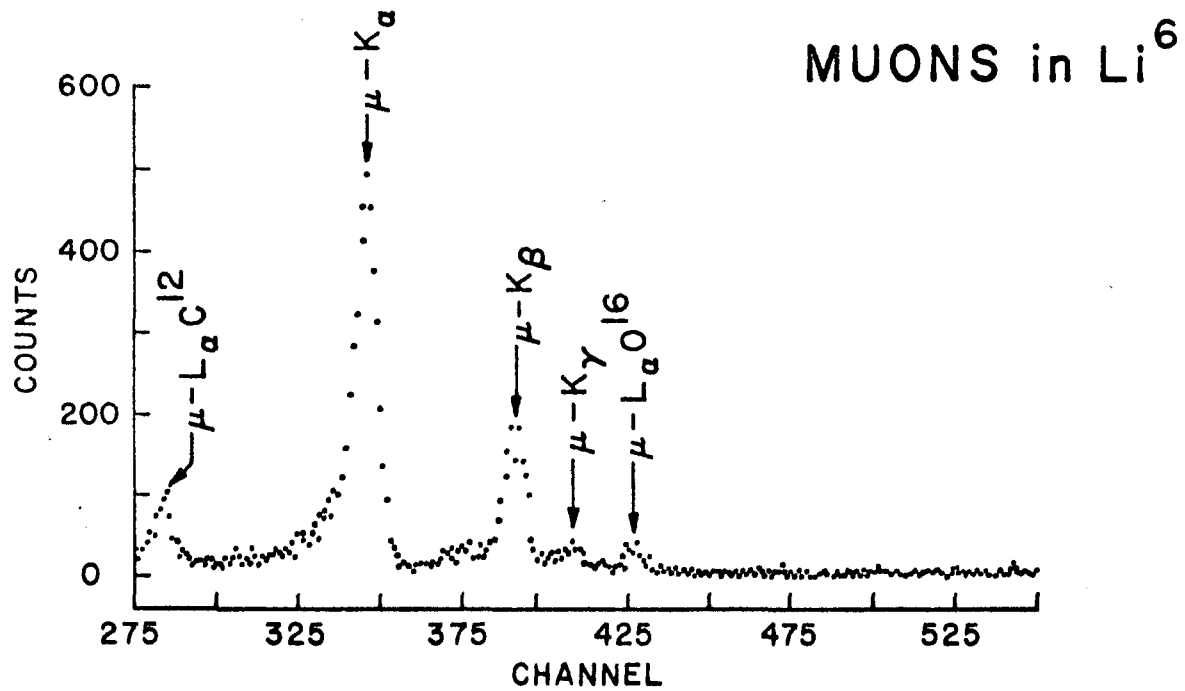
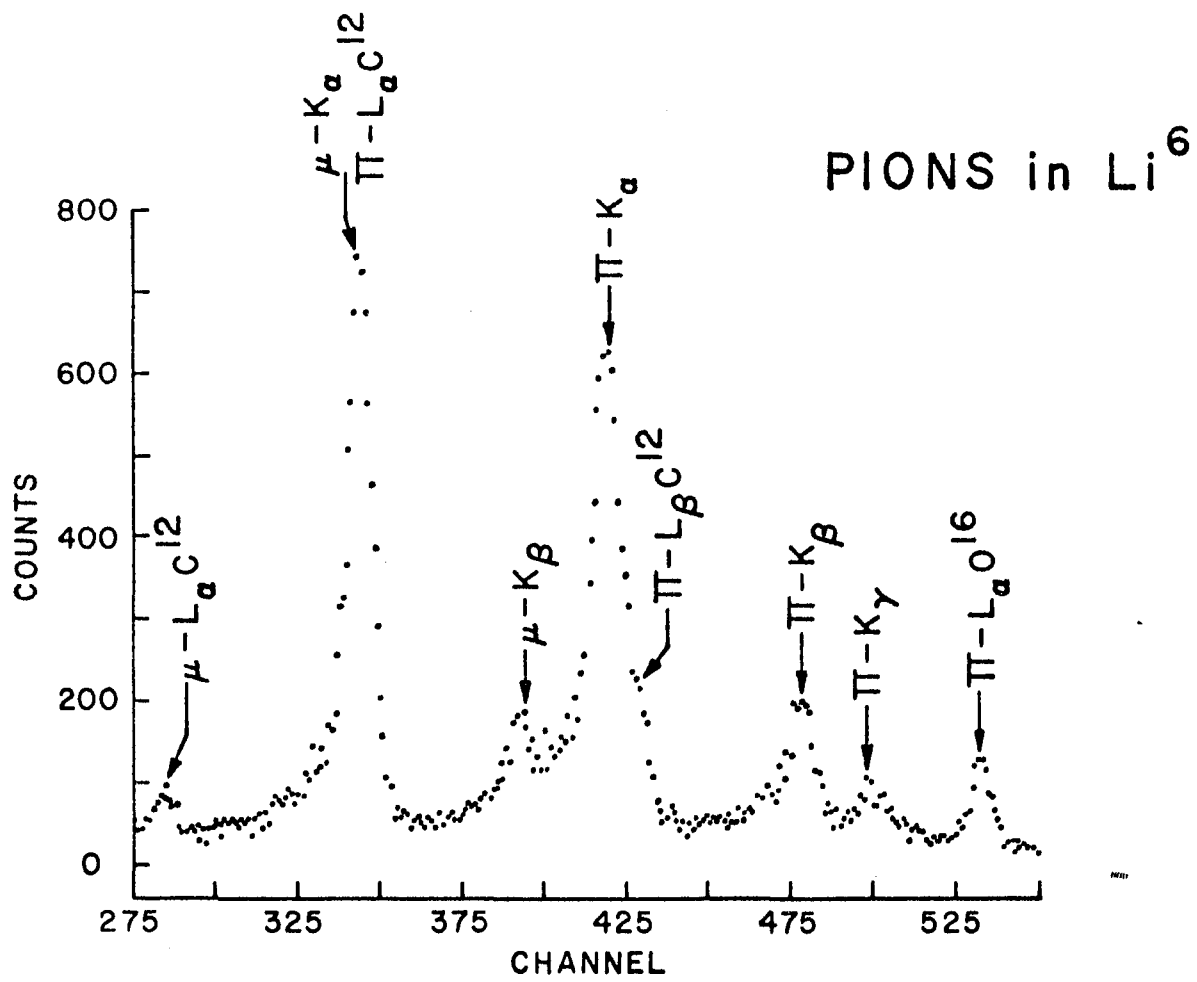


FIG. 15

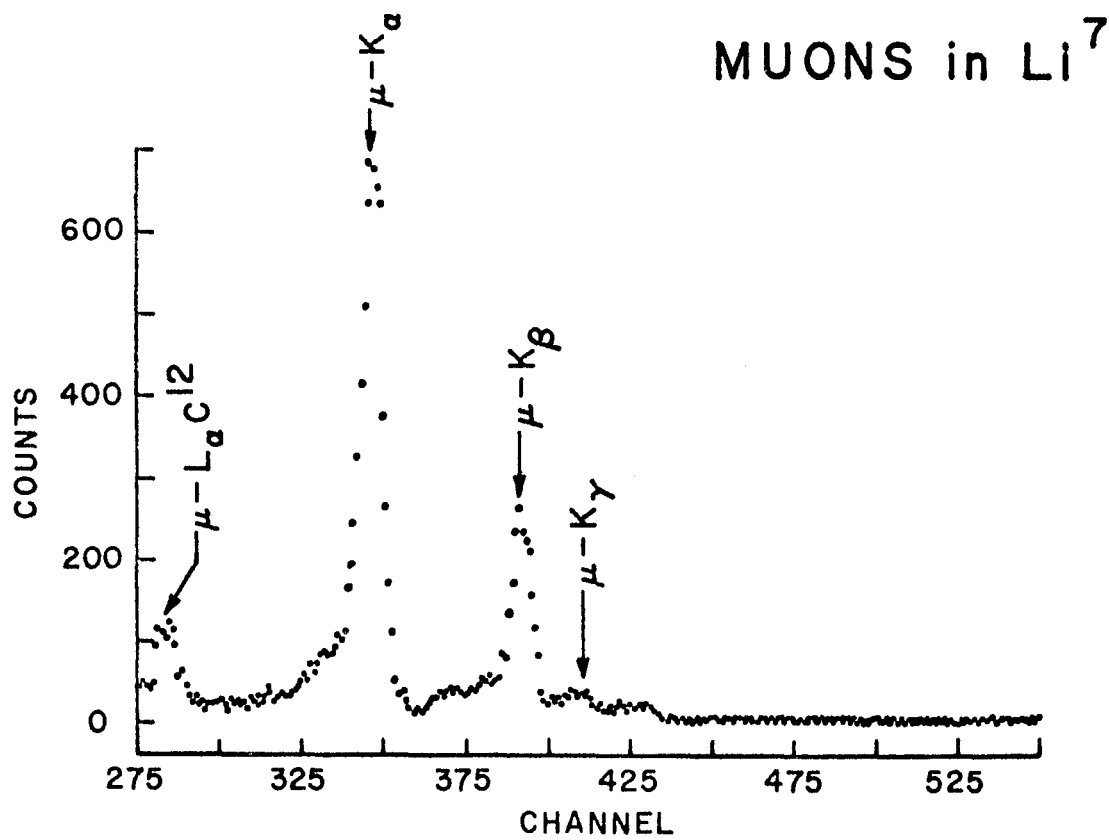
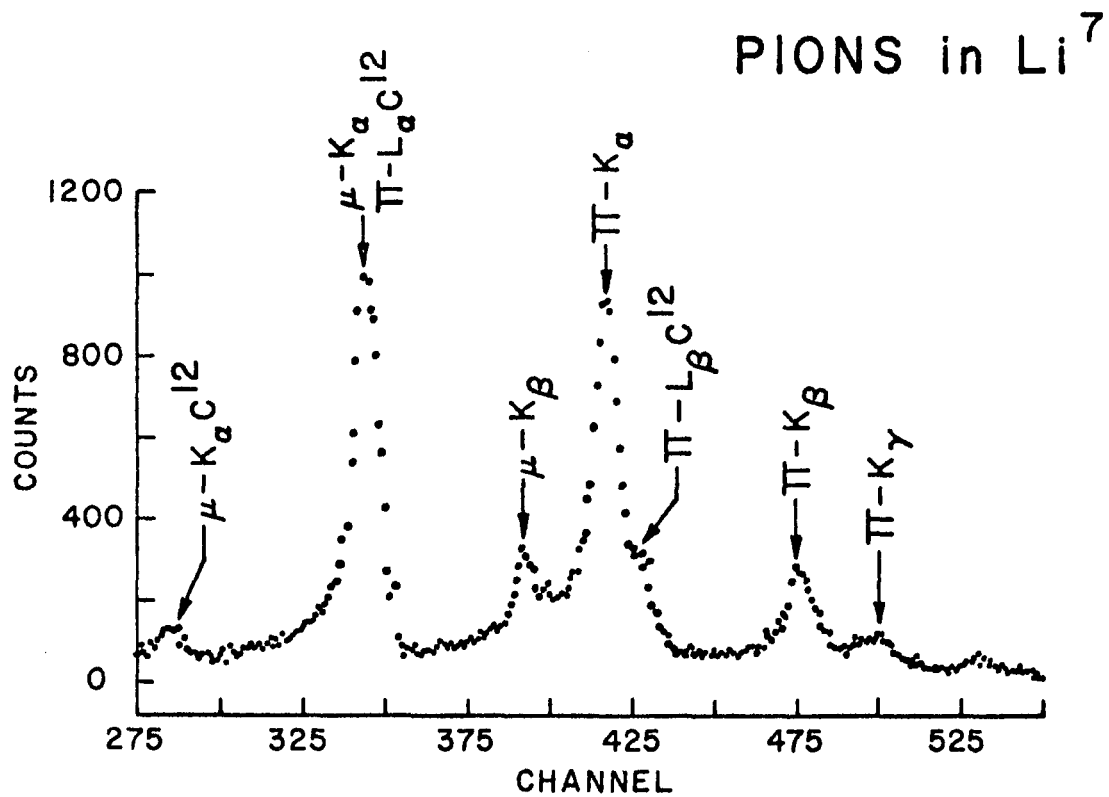


FIG. 16

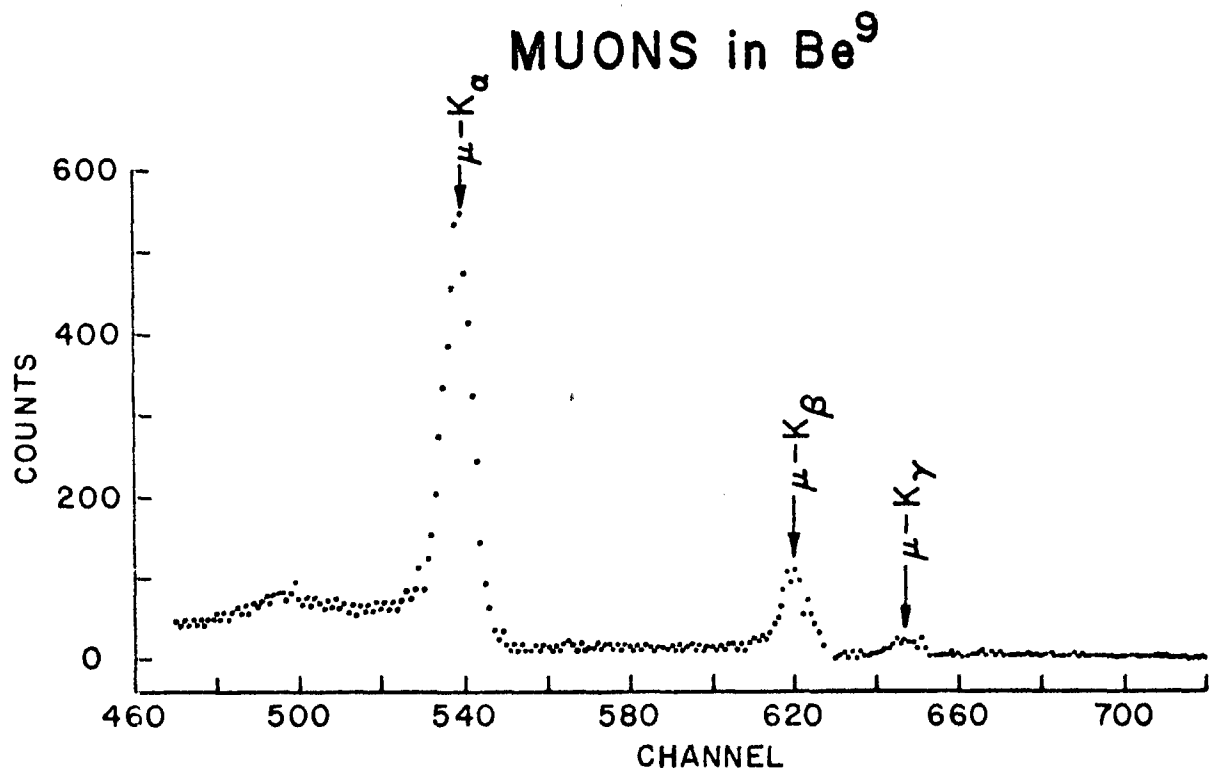
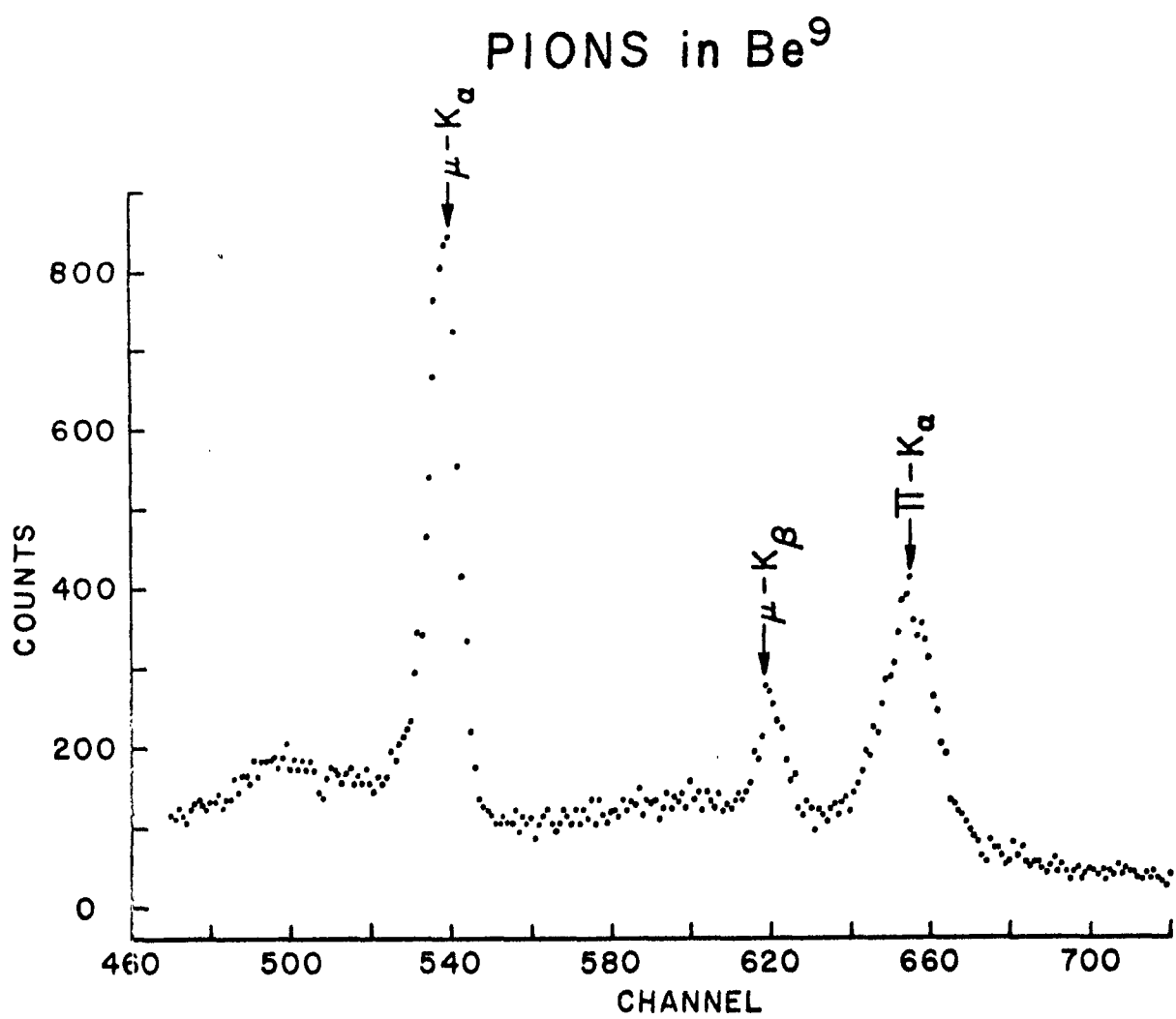


FIG. 17

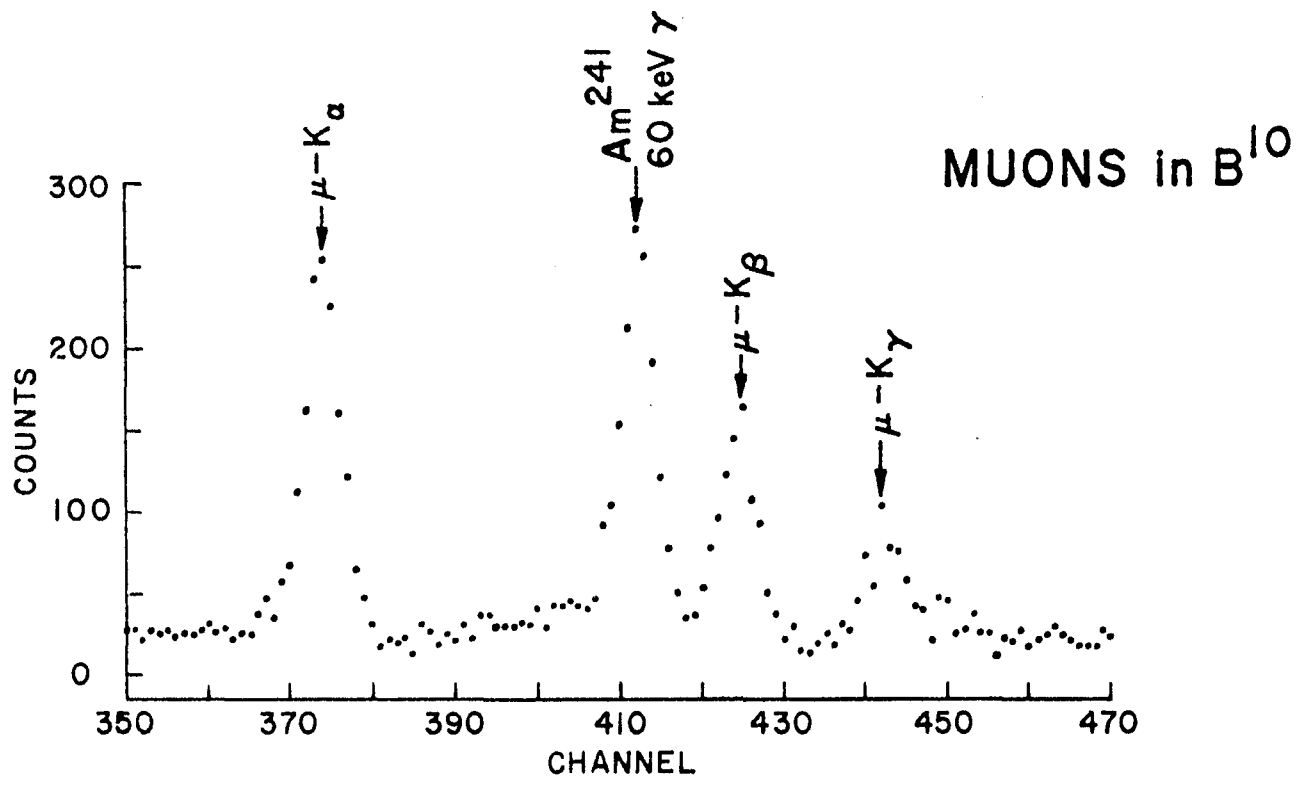
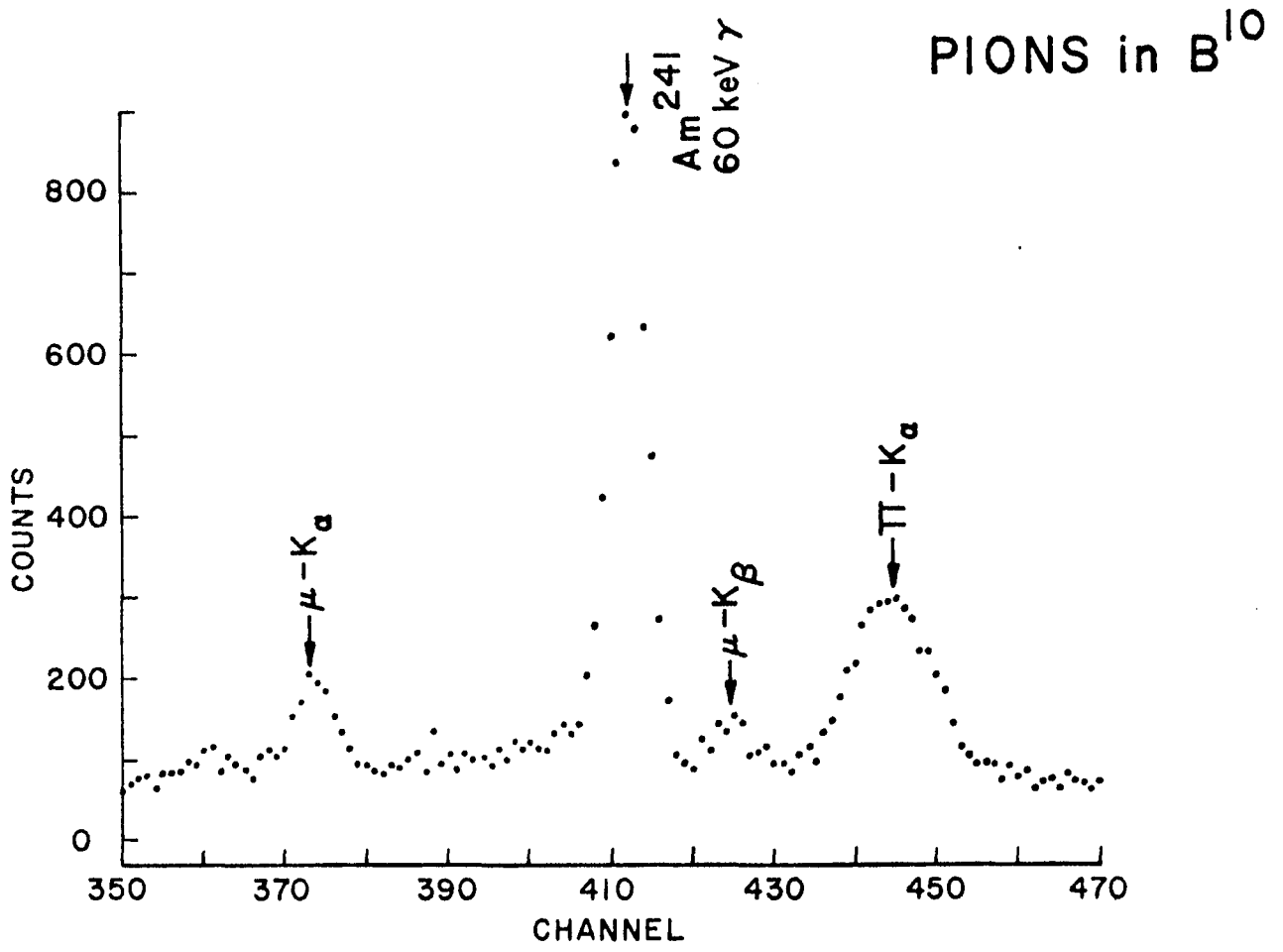


FIG. 18

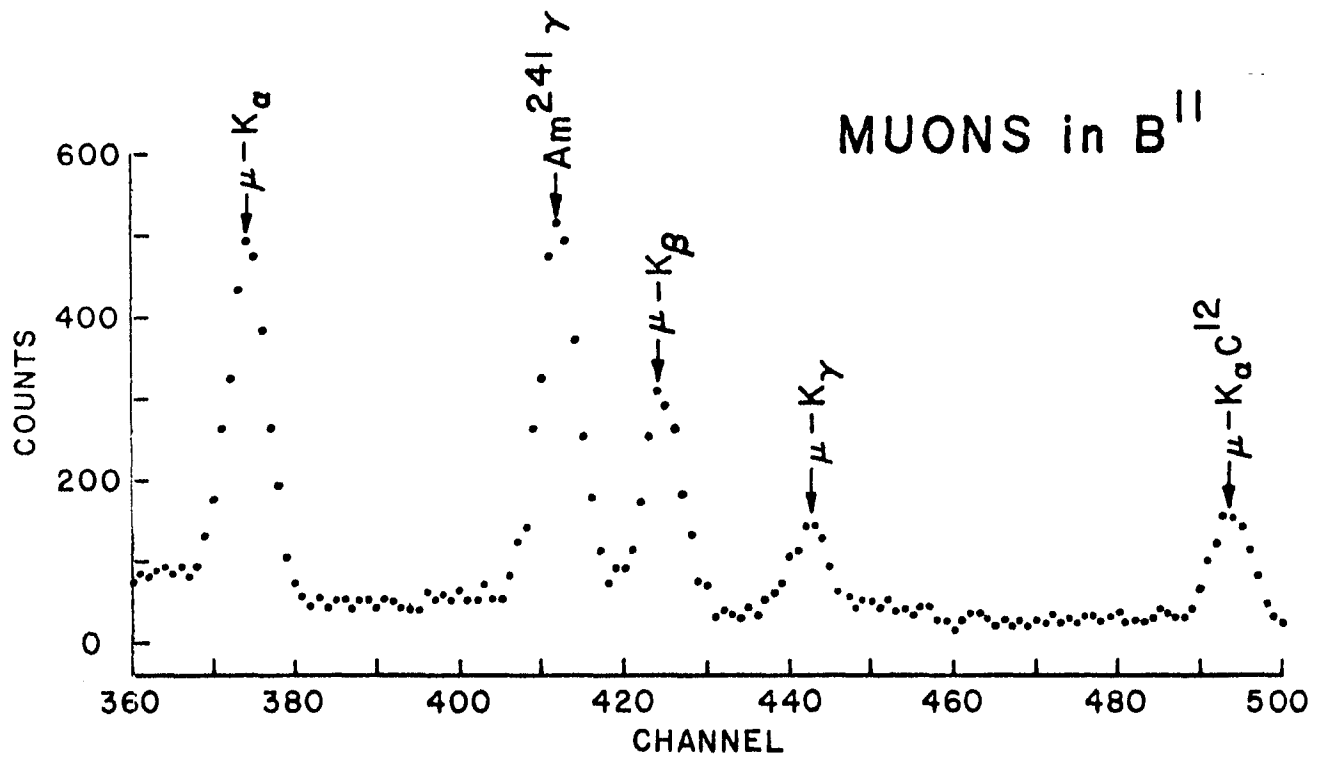
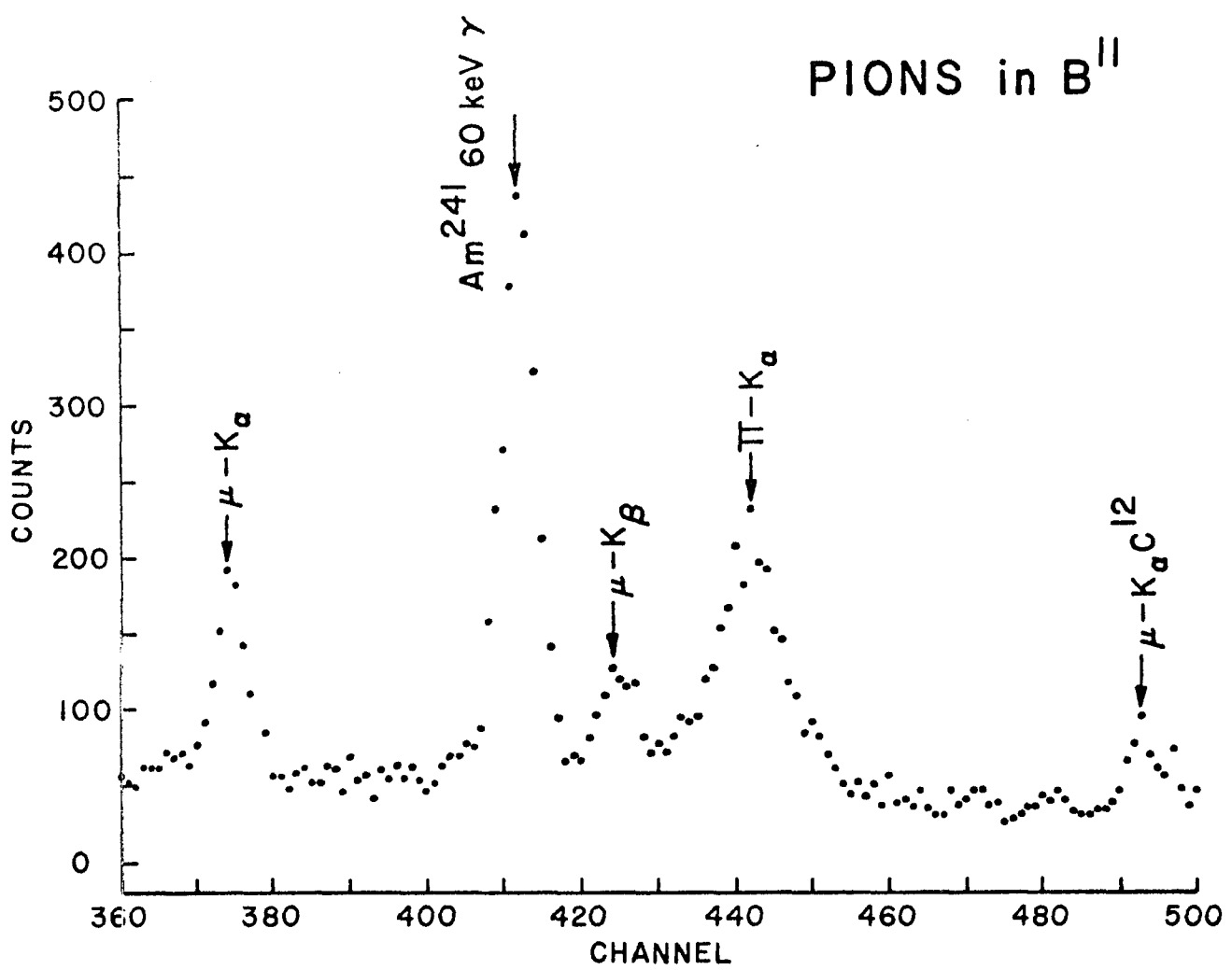


FIG. 19

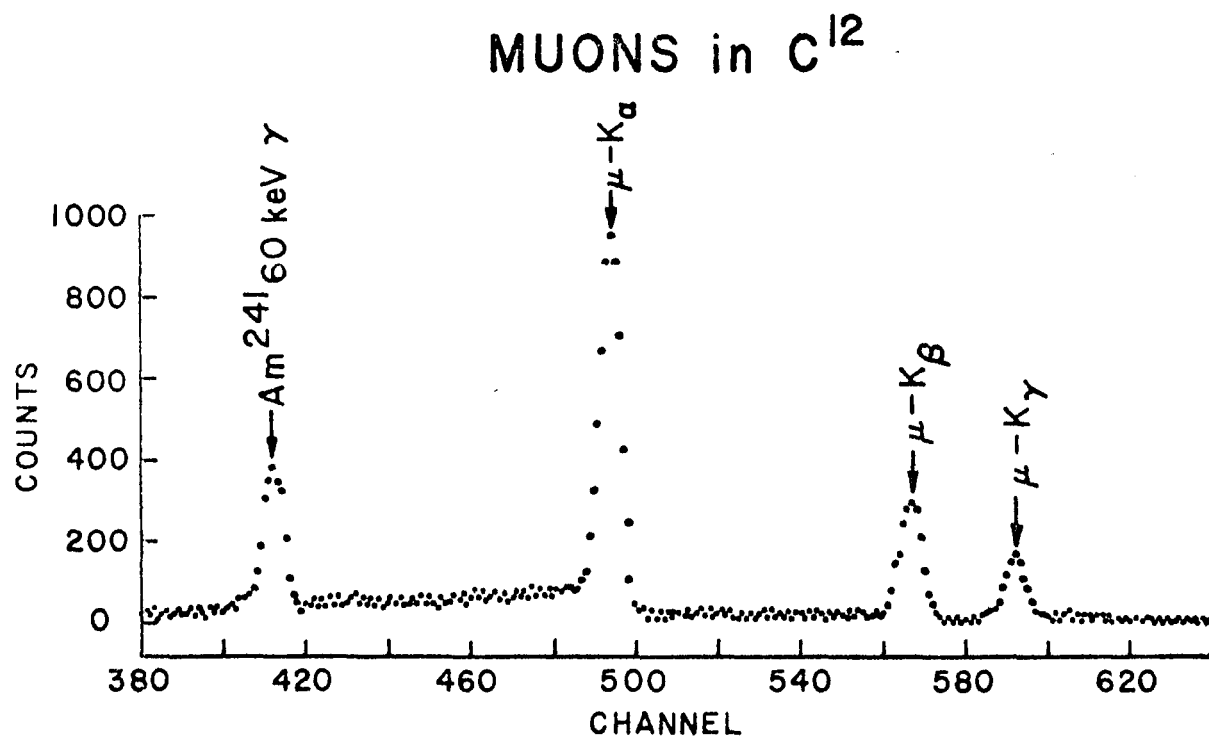
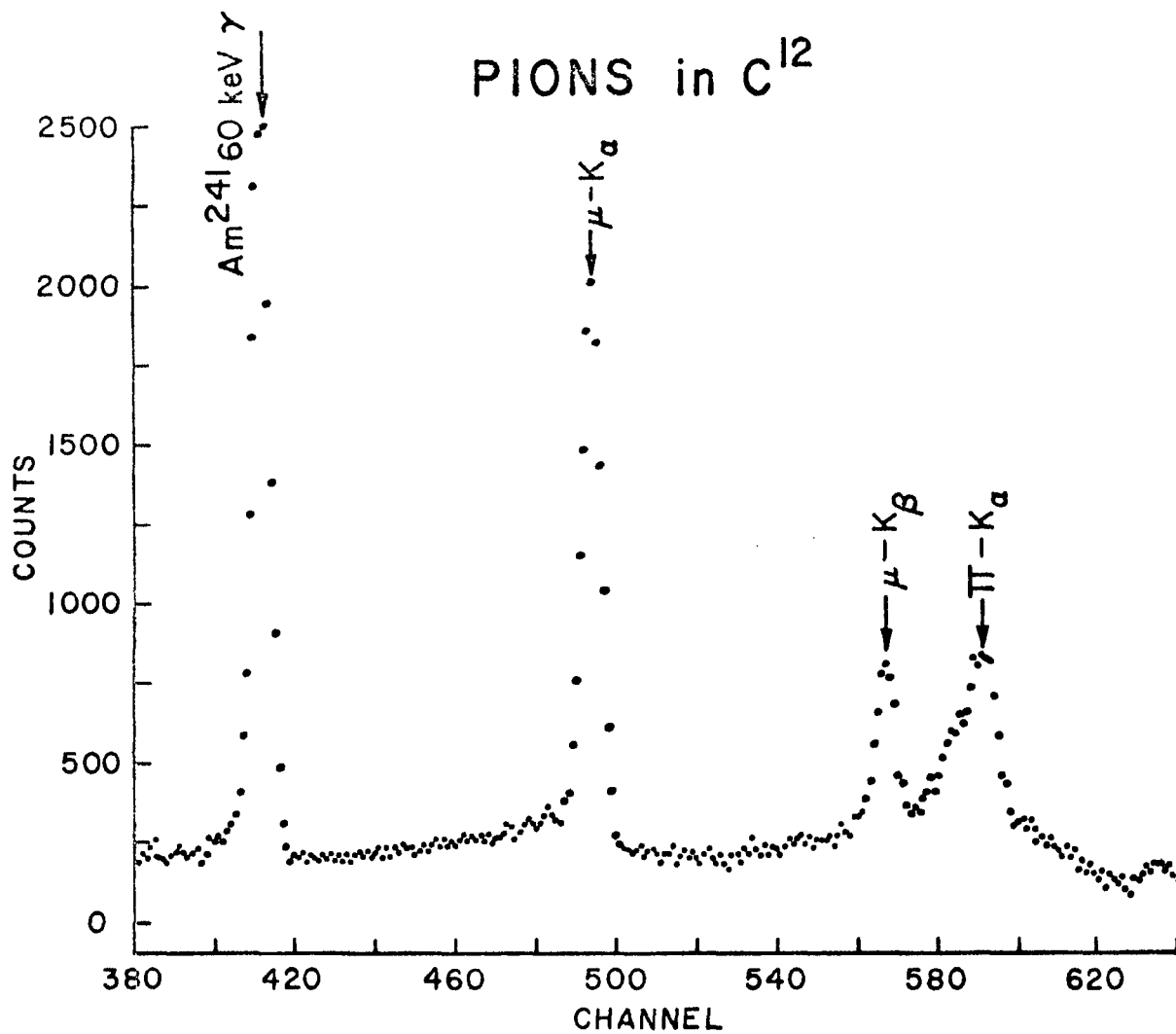


FIG. 20

CENTER CHANNEL DRIFT  
CALIBRATION PEAKS FOR  $\text{Li}^6$ ,  $\text{Li}^7$  &  $\text{Be}^9$  (CMU RUN)

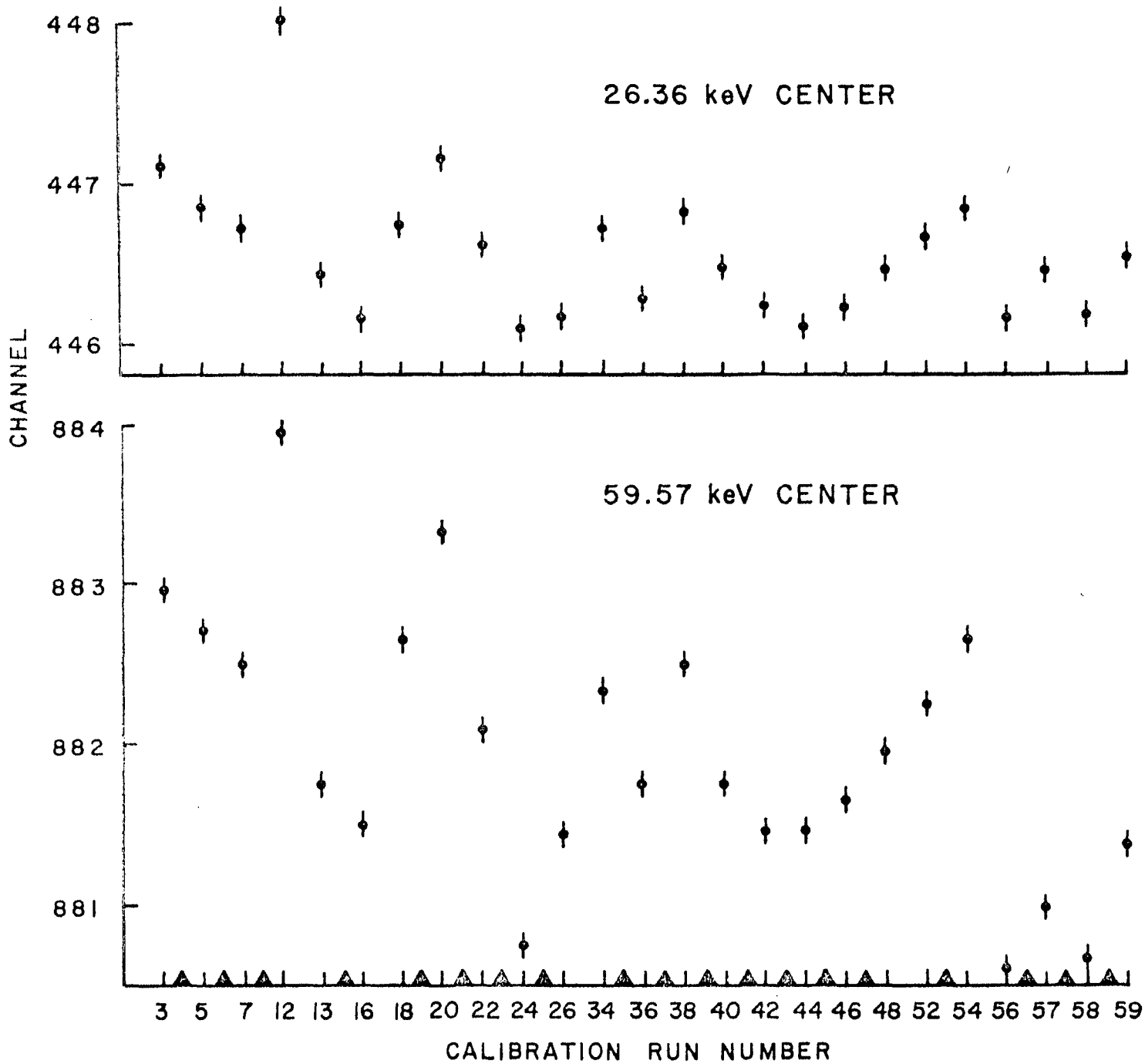
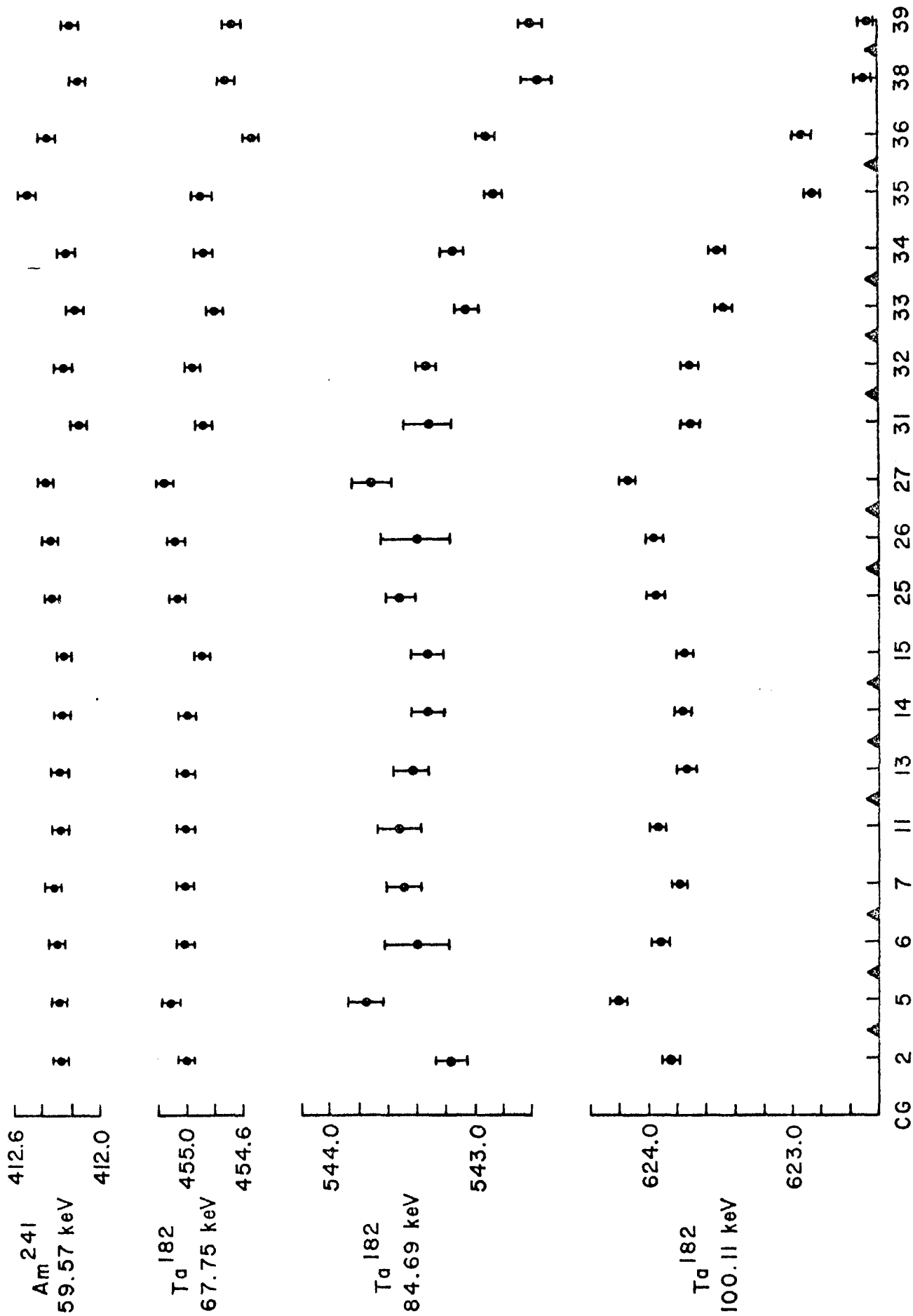


FIG. 21

# CENTER CHANNEL DRIFT

## CALIBRATION PEAKS FOR B<sup>10</sup>, B<sup>11</sup> & C<sup>12</sup> (CMU RUN)



CALIBRATION RUN NUMBER

FIG. 22

# CENTER CHANNEL DRIFT

## CALIBRATION PEAKS FOR $C^{12}$ (SREL RUN)

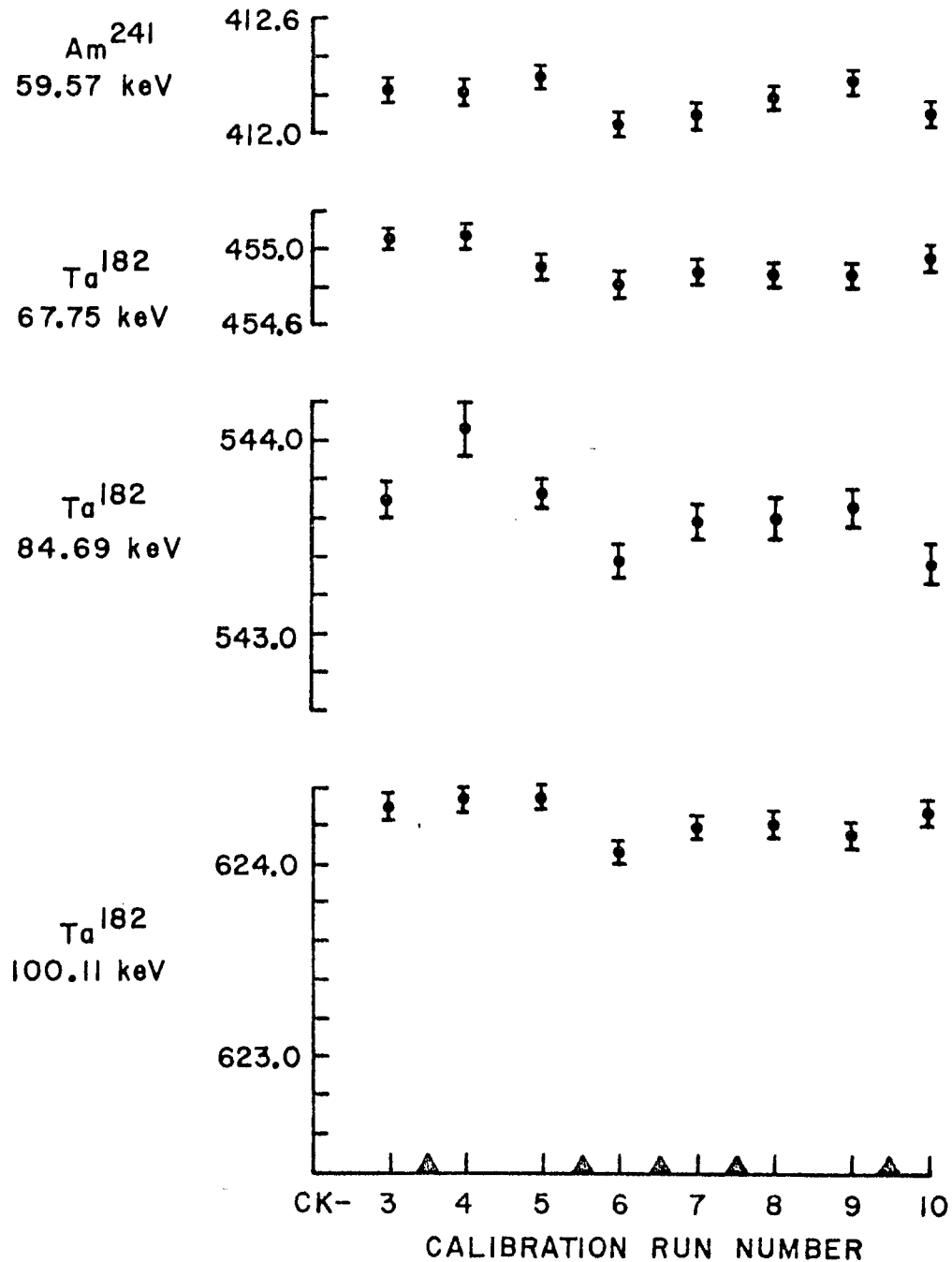


FIG. 23